NASA/CP–2000-209614

# Third Workshop on Photometry

*William J. Borucki*
*Ames Research Center*
*Moffett Field, California 94035*

*Lawrence E. Lasher*
*Ames Research Center*
*Moffett Field, California 94035*

**December 2000**

# Acknowledgments

Proceedings of a workshop held at the SETI Institute in Palo Alto, California
September 24 - 25, 1998

# Introduction

The papers contained herein were presented at the workshop held at the SETI Institute in Palo Alto, California, on September 24 and 25, 1998.

The discoveries of extrasolar planets by Wolszczan (1994), Mayor and Queloz (1995), Butler et al. (1997), and others have stimulated a widespread effort to obtain a body of data sufficient to understand their occurrence and characteristics. Doppler velocity techniques have found dozens of extrasolar planets with masses similar to that of Jupiter. Approximately ten percent of the stars that show planets with orbital periods of a few days to a week are expected to show transits. With the mass obtained from Doppler velocity measurements and the size from transit photometry, the densities of the planets can be determined. Theoretical models of the structure of "hot Jupiters" (i.e., those planets within a tenth of an astronomical unit (AU) of the parent star) indicate that these planets should be substantially larger in size and lower in density than Jupiter. Thus the combination of transit and Doppler velocity measurements provide a critical test of the theories of planetary structure. Furthermore, because photometry can be done with small-aperture telescopes rather than requiring the use of much larger telescopes, transit photometry should also reduce the cost of discovering extrasolar planets.

To successfully discover extrasolar planets by the transit method, investigators must monitor several thousand stars, make observations with an hour-to-hour precision of two to three parts per thousand, and observe the stars nearly continuously for several weeks. The required level of precision is difficult to attain on a routine basis, and the need to observe many thousands of stars suggests the use of small telescopes with large fields of view (FOVs). Hence the workshop emphasized equipment and software capable of routinely obtaining high precision when monitoring thousands of stars. The papers by Dunham, Borucki, Brown, Everett et al., and Henry discuss the instrumentation and software currently in use. Tests to identify the causes of photometric errors are described by Deeg and Doyle, Howell & Everett, Koch et al., Lockwood, and Mena-Werth.

Both photometers based on charged coupled devices (CCDs) and photomultiplier tube detectors (PMTs) are being used. The PMT detectors have been in use for many years; they show excellent relative precision when measuring night-to-night and year-to-year precision. However, even when skilled observers (Lockwood) or robotic systems (Henry) are employed, PMT systems can monitor less than 100 stars each night because of the need to move from star to star. Hence these systems are most advantageously employed to examine stars that have already been identified by the Doppler velocity technique as having planets. CCD detectors and wide FOV lenses allow many thousands of targets to be monitored simultaneously, but are just beginning to provide the precision obtained by the well-established systems based on PMTs. Wide FOV systems are best suited to searching a large area of the sky to discover planets.

## References

Butler, R. P.; Marcy, G. W.; Williams, E.; Hauser, H. and Shirts. P.: Astrophys. J. vol. 474, 1997, p. L115.
Mayor, M. and Queloz. D.: *Nature,* vol. 378, 1995, p. 355.
Wolszczan, A.: *Science* vol. 264, 1994, p. 538.

iv

# Table of Contents

# Ultra-High Precision CCD Photometry

Steve B. Howell and Mark E. Everett
*Department of Physics and Astronomy*
*University of Wyoming*
*Laramie, Wyoming 82071*

## Abstract

Many applications in modern observational astrophysics require ultra-high-precision charged coupled device (CCD) photometry. Photometry at these levels of precision (<1%) enters into a new regime of usage for CCD detectors and, as such, has numerous associated error sources previously unconsidered. In this paper, we discuss some of these error sources that have been previously ignored or were unknown until CCD photometric precisions entered into the range of 0.1% or better. We consider how the signal-to-noise ratio (S/N) of a CCD measurement may be improved and look at the problems associated with undersampling of point spread functions, nonlinearities in the CCD response, flat-field issues, intra-pixel quantum efficiency variations, and finally de-focused images. All of these effects are likely to be error sources at ultra-high-precision levels, yet few of them have had quantitative studies performed at the detailed levels required.

## Introduction

Applications of CCD imagers to observational projects requiring ultra-high-precision photometry are ever increasing. Research areas in which such high levels of precision photometry (better than 1%) are desired include searching for transits of extra-solar planets, asteroseismology, and variability of faint galactic and extra-galactic objects over large fields of view. The first and last of these applications require an additional constraint of wide-field imaging in order to be productive, while all three require photometric results of the highest precision possible.

We examine herein numerous issues that are generally of little import in typical CCD photometry, but remain as sources of error when ultra-high precisions are desired. Photometric precisions of better than 1% (i.e., precisions of better than 0.01 magnitudes) are easily attainable in theory but difficult in practice. Many limiting factors come into play, some of which are subtle and others are as yet undetermined. We concentrate in this paper on photometric errors due to the CCD detector itself and spend little time discussing additional problems, which may occur because of the telescope, the software, or misconceptions in data reduction techniques. This paper assumes that the reader is familiar with the terminology and use of a CCD detector. Further details of the properties of CCDs can be found in Howell (1999).

In ultra-high-precision CCD photometry, one should be able to routinely achieve precisions of 0.001 magnitudes (0.1%) or better. To date, however, the best consistent precisions obtained with CCD imagers are near 0.003–0.006 magnitudes for single observations of a few minutes duration and a modest-sized telescope. These precisions are obtained through the use of differential photometric techniques (Howell et al., 1988; Honeycutt 1992; Gilliland et al., 1993). Current CCD error values are still a factor of 3–6 above single photomultiplier tube detector (PMT) measurements (of very bright stars) and a factor of ~10 or more above the theoretical limit of a CCD. One of the challenges facing observers wishing to meet or exceed present-day values is to understand the factors that limit the precision and to determine methods by which these can be eliminated or further reduced. We consider below a set of likely or

known culprits that limit the precision of CCD measurements along with some possible solutions for each.

**Signal-to-Noise Ratio**

First we make a few comments about the S/N of a CCD measurement and what the limiting factors are. The standard equation for the S/N of an observation follows:

$$\frac{S}{N} = \frac{N_*}{\sqrt{N_* + n_{pix}(1 + \frac{n_{pix}}{n_B})(N_S + N_D + N_R^2 + G^2\sigma_f^2)}}$$

The "signal" term in the above equation, $N_*$, is the total number of photoelectrons (signal) collected from the object of interest. $N_*$ may be from one pixel (if determining the S/N of a single pixel as is sometimes done for a background measurement) or $N_*$ may be from several pixels, such as all those contained within a stellar profile. The noise terms in the above equation are the square roots of $N_*$, plus $n_{pix}$ (the number of pixels under consideration for the S/N calculation) times the contributions from $N_S$ (the total number of photoelectrons per pixel from the background or sky), $N_D$ (the total number of dark current electrons per pixel), and $N_R^2$ (the total number of electrons per pixel due to the read noise).

The term $(1 + \frac{n_{pix}}{n_B})$ provides a measure of the noise incurred due to any error introduced in the estimation of the background level on the CCD image, and $n_B$ is the total number of background pixels used in the S/N calculation to estimate the background (sky) level. One can see that the small values of $n_B$ will introduce the largest error, because they will provide a poor estimate of the mean level of the background distribution. Thus, very large values of $n_B$ are to be preferred, but clearly some trade-off must be made between providing a good estimate of the mean background level and using background pixels from areas on the CCD image that are far from the source of interest and possibly of a different character. In the term $G^2\sigma_f^2$, G is the gain of the CCD (in electrons/Analog to Digital Unit (ADU)) and $\sigma_f^2$ is an estimate of the 1-sigma error introduced within the analog-to-digital (A/D) converter and has a value of approximately 0.289.

Those interested in a deeper understanding of the terms in and the derivation thereof should refer to the discussion in Merline and Howell (1995).

We see from the above equation that if the total noise for a given measurement is dominated by the first noise term, $N_*$, (i.e., the noise contribution from the source itself), then the CCD equation reduces to

$$S/N = \frac{N_*}{\sqrt{N_*}} = \sqrt{N_*}$$

2

yielding the expected result for a measurement of a single Poisson behaved value. Turning the S/N of a measurement into a standard error for the measurement in magnitudes yields

$$\sigma\, magnitudes = \frac{1.0857\sqrt{N_* + p}}{N_*}$$

In this expression, $p$ is equal to $n_{pix}(1 + \frac{n_{pix}}{n_B})(N_S + N_D + N_R^2 + G^2\sigma^2_f)$ and the value of 1.0857 is needed as the correction term between an error in flux (electrons) and the error in magnitude (see Howell et al., 1988). We again see that if the Poisson error of $N_*$ dominates, the term $p$ can be ignored and this equation reduces to that expected for a 1$\sigma$ error estimate in the limiting case of a bright object.

This last expression can be used to determine the highest possible precision obtainable with a given CCD. Clearly this is best accomplished for the brightest possible source, that is, one that has its error completely dominated by the photon statistics of the source itself. If the *only* noise source is the star itself, and one can spread the light of the stellar profile across, say, 10 pixels, then for a CCD with a pixel full well capacity of, say, 350,000 electrons, the maximum signal that could be collected is 3,500,000 electrons. This would result in a maximum photometric precision of 0.06% or 5.8 X 10$^{-4}$ magnitudes. Reality does indeed cause limits to this number, but the reader can see that current-day best precisions still have a way to go to approach this number. In our own work using a testbed CCD with a meager well depth of near 85,000 electrons (Howell et al., 1998, Everett et al., 1998), we routinely achieve precisions of 0.004–0.006 magnitudes, not far from the theoretical limit for our system of 0.0037.

## Stellar Point-Spread Functions And Partial Pixel Sampling

Adaptations of older wide-field telescopes, such as Schmidt telescopes, to use with CCD imagers is occurring today. The major advantage is the existence of the telescope and its associated general disuse by the former owner. However, the use of such a system has associated problems when the goal of ultra-high-precision photometry is desired. The two-dimensional (2-D) shape of a star image, the point-spread function, or PSF, can be a strong function of location of the PSF at the focal plane and its color. For example, many Schmidt telescopes were built specifically to take photographs of large sky regions; thus their optics were often configured to provide best focus and PSF shapes at or near the field center and at one specific wavelength.

Physical conditions that cause additional PSF variations include telescope focus (often a strong function of temperature), telescope tracking and guiding, and other items such as wind shake and differential refraction. A perfect PSF for a star will contain ~100% of the light within an inscribed circle of 3.0 times the full width at half maximum (FWHM) of the PSF. However, as the PSF intensity drops near the edge of the profile, i.e., in stellar wings, the light collected per pixel from the source becomes less dominated by the star and increasingly dominated by the sky background. Thus, extraction of the source counts from a 2-D CCD image yields the best S/N, or the highest photometric precision, when an extraction radius of less than 3.0*FWHM is used (Howell 1989).

Shapes of stellar PSFs are quite complex and can extend for many tens of arc minutes, although their wings at these distances are 20 or more magnitudes fainter then their cores (King 1971). Mathematical functions such as Gaussians or Lorentzians are commonly used to approximate PSF shapes (Diego 1985), but in the case of wide-field imaging, the actual shape of a PSF is difficult to determine because of how it is sampled on the finite-sized grid of pixels of the CCD detector. Examples of such sampling are provided in Howell et al., (1996) and Merline & Howell (1995).

Pixel sampling can be quantified as follows. We defined a sampling parameter, r, such that an application of Nyquists theorem for critical sampling can be applied to a PSF imaged on a CCD. The value of r is calculated as

$$r = \frac{FWHM}{P}$$

where FWHM is the full width at half maximum values for the stellar PSF and P is the pixel size, both given in the same units (usually arc seconds). For r values of less than or equal to 1.5, the data are considered to be under or poorly sampled, while r > 1.5 is considered well-sampled data. For r values at or below 1.5, PSFs take on sampled shapes that are far from those of simple mathematical functions, and one should expect increasing errors to occur in photometric and astrometric measurements with decreasing r (Howell et al., 1996, King 1983).

For undersampled measurements, the stellar PSF is imaged by only one or a few CCD pixels and is thus sampled by these pixels in a manner that can cause it to appear brighter (pixel centered) or fainter (pixel corner), simply as a consequence of its centering. Small changes in telescope pointing or PSF modulation can cause apparent stellar variation in a random or possibly periodic manner. Photometric measurements using such undersampled data can contain large errors, depending on how the software used handles the estimation of the source flux falls on partial pixels. Partial pixels occur at the PSF edge, as it has a circular footprint that is imaged onto a rectangular grid. Partial pixels are particularly important in undersampled data because they can contain large fractions of the source flux, yet only small fractions of the total PSF.

There are three methods of dealing with partial pixels: 1) Keep all pixels in the summation of the stellar flux in which the PSF is even partially in; 2) throw out all pixels for which the pixel area is not 100% covered by the PSF; and 3) define some method within the analysis of the photometry that deals with these partially covered pixels. The latter method is the best to use, but the most difficult to implement in practice. Often schemes such as using the mean partial pixel value times the percentage of the pixel contained in the inscribed circle defining the PSF footprint are tried. The worse the under-sampling, the poorer the results one can expect from such simple schemes. The best solution to this problem appears to be that of not being undersampled in the first place.

**CCD Linearity**

One of the greatest advantages of a CCD is the fact that is has a linear response to detected light over a large dynamic range. Most of us are aware of possible nonlinearities that may occur at very low or very high signal levels. However, when playing the ultra-high-precision photometry game, we must also be aware of some other issues related to nonlinearity and to gain changes that may occur.

The maximum usable count level within a CCD pixel is determined by one of three different ways. Saturation can occur in a CCD if the pixel full capacity is exceeded or if the A/D converter bit limit is too low to represent the total amount of charge collected. Additionally, the CCD may become nonlinear in its response to input flux at a level below either of the two forms of saturation just mentioned. These three effects are well known and usually calibrated and listed for a particular CCD.

However, detailed study of CCD linearity curves usually reveals small deviations from a straight line due to nonlinearities occurring at modest charge levels. Gain changes during readout related to the x,y location of the pixel within the CCD or with temporal variations such as on-chip amplifier temperature cycling can also occur. These effects are quite small, less than 1%, but again of importance for ultra-high-precision photometry. Individual CCDs must have their linearity checked and understood

at very precise levels, and any spatial or temporal variations must be accounted for or avoided in order to achieve the best possible photometry. Well-run laboratory tests, careful to avoid false alarms due to small variations of the illumination device or CCD temperature changes, can determine with good accuracy the effects of CCD nonlinearities.

Another way in which nonlinearity can appear is within the cores of bright stars. If the pixels at the centers of star images have count levels near the onset of nonlinearity within a particular CCD, it may be that slight atmospheric, seeing, focus, or pixel grid placement changes can cause the tops of the PSFs to push into the nonlinear regime. This type of variation would be very difficult to quantify and would likely occur randomly throughout a time-series data set, leaving the reduced data containing unknown and intermittent errors. One sure way to avoid such a problem is to keep integration times short enough that the brightest stars of interest contain no pixels with count levels near the end of the range of linearity.

## Flat Fielding

Numerous papers and presentations have been written on the marvels of flat fielding a CCD. Many have similar approaches to the problem, and none seems yet to be the ultimate solution. Here, we simply offer some additional advice. CCD pixels respond differently to light of different wavelength. In order to properly flat field a blue star, one must have a correct assessment of the CCD response to blue light; for a red star, one must know the red response. This is simple in principle but extremely difficult to accomplish perfectly in practice. Stars and other astronomical objects come in all colors, and flat fields do as well. Twilight flats and most dome flats are reddish, while night-sky flat fields are bluish but of low S/N. Wide-field CCD images also are plagued by varying differential refraction across their field of view, causing color terms to be increasingly important.

The best solution seems to be to make your flat fields as spectrally and spatially flat as possible. Uniform illumination with light of all colors, possibly filtered to reduce the red while allowing increased blue flux, seems to be one of the best choices. In some instances, the use of a flat-field image as part of the data reduction can make the final precision worse than when no flat is used at all. Keeping PSFs on identical pixels and using differential techniques could be an ideal solution to the problem, alleviating the need for flat fields at all. However, in practice this is rarely possible, although space-based telescopes offer the best hope. Experimentation with your CDD, flat-field images, and data-reduction procedures is well advised.

## Intra-Pixel Effects

In a study of the quantum efficiency of a CCD on the intra-pixel level, Jorden et al., (1994) discovered that the overlying gate structures of a pixel cause very large color-dependent response variations to occur, depending on the location within the pixel of the incoming photons. In general, front-side illuminated CCDs have three gates overlying each active pixel, and the quantum efficiency within these three intra-pixel regions can vary by up to 15–20% from one location within a pixel to another. This is the major reason that undersampled PSFs are essentially impossible to use to obtain ultra-high-precision photometric information. Even Nyquist-sampled PSFs, while strictly meeting sampling theory requirements of 2 pixels per FWHM, do not allow for precise results because of internal pixel structures. PSFs with an asymmetric shape or high-frequency components are particularly troublesome. Adding to the intra-pixel sampling variations are image motion, PSF variations, and seeing changes, all of which make the problem worse. Back-side illuminated CCDs provide a better—but not perfect—solution to this problem. Again, well-sampled PSFs provide the best solution.

Quantitative studies of undersampled photometric observations have been performed for the wide field planetary camera (WFPC) aboard the Hubble Space Telescope (HST) and stellar observations made

with the CCD imager on the Galileo spacecraft, but neither of these studies were aimed at ultra-high-precision observations of time-series data.

## De-focused Images

A few observational projects seeking high-precision photometric results have been performed with stellar images that have been purposely de-focused. The French COROT mission search for extra-solar planets and their asteroseismology program are planning to collect CCD images that are de-focused slightly. This idea has also been proposed for the Kepler extra-solar planet space mission.

Advantages of using de-focused PSFs imaged on a CCD are likely to be: 1) better pixel sampling will reduce photometric deviations due to PSF changes and intra-pixel effects; 2) PSF centering becomes less of an issue; 3) dealing with partial pixels within the PSF is less of an issue; 4) saturation due to A/D limits or pixel full wells is greatly reduced; 5) the number of photons from the source of interest can be greatly increased because the light can be collected over many pixels; and 6) the overall dynamic range obtainable on a given CCD image can be large. Disadvantages seem to be limited to loss of the faintest stars for precision photometry and higher risk of overlapping PSFs due to field crowding.

Although the benefits of de-focusing probably outweigh the problems associated with it, there has yet to be a detailed study of this methodology. For example, effects of seeing, telescope tracking, and color terms all need to be explored in order to verify this technique and to provide guidance of the proper de-focus values to use. Optical systems that are designed to focus images on the detector may not provide a good—or even useful—PSF by simply de-focusing the image. We predict that the best out-of-focus CCD image, one that will provide the highest possible photometric precision, is one produced by an optical system specifically designed to make "perfect" de-focused images. The paper by Dunham in this volume has explored this idea; it includes a section on an optical design that produces an optimally blurred image. A quantitative study of de-focused images and their effect on ultra-high photometric results for time-series data sets is far overdue.

## Conclusion

The discussion presented here summarizes the many unknown or unstudied issues that may affect photometric data. For the common CCD user, these effects are not important for observations that are absolute or desired at only 1% or larger error levels. However, for photometric precisions of the highest quality, at the theoretical limits of CCDs, the above issues are of intimate concern. No doubt numerous similar results await discovery.

6

# References

Diego, F.: Publ. Astron. Soc. Pacific, vol. 97, 1988, p. 1209.

Everett, M.; Howell, S. B.; and Ousley, D.: In "Third Workshop on Improvements to Photometry," W. Borucki, ed., NASA Conference Publication, 1998.

Gilliland, R. L., et al.: Astrophys. J., vol. 106, 1993, p. 2441.

Honeycutt, R. K.: Publ. Astron. Soc. Pacific, vol. 104, 1992, p. 435.

Howell, S. B.; Mitchell, K.J.; and Warnock, A., III: Astrophys. J., vol. 95, 1988, p. 247.

Howell, S. B.: Publ. Astron. Soc. Pacific, vol. 101, 1989, p. 616.

Howell, S.B.: In "Astronomical CCD Observing and Reduction Techniques," ASP Conference Series, vol. 23, S. Howell, ed., 1992, p 105.

Howell, S.B.; Koehn, B.; Bowell, E. L. G.; and Hoffman, M.: Astrophys. J., vol. 112, 1996, p. 1302.

Howell, S.B.: "Handbook of CCD Astronomy," Cambridge University Press, 1999.

Jorden, P. R.; Deltorn, J.-M.; and Oates, A. P.: In "Instrumentation for Astronomy VIII," SPIE Proc., vol. 2198, 1994, p 57.

King, I: Publ. Astron. Soc. Pacific, vol. 83, 1971, p. 199.

King, I:, Publ. Astron. Soc. Pacific, vol. 95, 1983, p. 163.

Merline, W.; and Howell, S. B.: Exp. Ast., vol. 6, 1995, p. 163.

# A Case Study Illustrating the Practical Limitations of Precision Photoelectric Photometry

*G. W. Lockwood*
*Lowell Observatory*
*1400 Mars Hill Road*
*Flagstaff, AZ 86001*

## Abstract

We examine a long series of Strömgren *b, y* differential measurements of sunlike stars to see which observational and instrumental factors are most important in attaining high photometric precision. Often, an intrinsic variation of comparison stars dominates the error budget, with instrumental and observational errors playing a relatively minor role.

## Introduction

We have used the Lowell Observatory 21-inch telescope as a dedicated photometric facility on more than 2400 nights since 1974. Throughout this entire interval, the original photometer, photomultiplier, and Strömgren *b, y* interference filters have remained in continuous service. We updated the electronics and data-acquisition computer only twice, in 1982 and 1993. Consequently, the voluminous data from this telescope are very homogeneous and are thus suitable for searching out subtle sources of error, especially those that might become important over the decade-long intervals that typify our planetary and stellar programs. In this paper, we revisit measurements of sunlike stars made from 1984 to 1995 to look anew for instrumental and observational sources of error. These observations are especially suitable for analysis because they were all made by one person, Brian A. Skiff, a highly skilled and consistent observer.

Instrumental errors at the sub-1% level have been notably lacking over the past 25 years. Nevertheless, we remain alert to symptoms of trouble, especially those that might grow in importance over many years. In this paper, we examine three potential problem areas: (1) the intrinsic variability characteristics of the comparison stars; (2) changing observational and temporal circumstances—weather, seeing, moonlight, etc.; and (3) instrumentation effects—temperature artifacts, variations of optical and electronic sensitivity, etc. We consider each category in turn, using simple statistical tests whose power is enhanced by the large quantity and long time span of homogeneous data.

Our photometric system is defined by 50 Strömgren standard stars located around the sky (Lockwood and Thompson, 1999). For the long-term differential photometry programs, occasional standard star measurements keep track of slow changes in the instrumental magnitude scale. These become important on decade timescales. Long-term studies of outer planets and satellites (e.g., Thompson and Lockwood, 1992; Lockwood and Thompson, 1999) and sunlike stars (Lockwood, et al., 1997; Radick, et al., 1998) show that the photometric system has been very stable.

## Demographics of Variability for F, G, and K Stars

Program stars are included in trio or quartet groups containing two or sometimes three ostensibly stable comparison stars that were chosen to match the color and brightness of each program star as closely as possible. In planning our project, we had little to go on in choosing the comparison stars other than approximate HD spectral types and magnitudes, and the presumption that most F, G, and K stars are relatively stable. Main sequence field stars such as our targets tend to be nonvariable (e.g., Jerzykiewicz and Serkowski, 1966), so reliable comparison stars are essential.

Figures 1 and 2 show the statistics of variability in our sample of 41 program and 73 comparison stars on night-to-night and year-to-year timescales. Figure 1 illustrates the root-mean-square (rms) variation of differential magnitudes from night to night within seasons. The distribution for stars deemed "constant" is shown above the central axis on the figure (about two-thirds of the sample) while the distribution for stars deemed "variable" (about one-third of the sample) is shown below. Both distributions peak at 0.002 magnitude (mag) rms. However, the median and third-quartile values are distinctly higher for the variable stars.
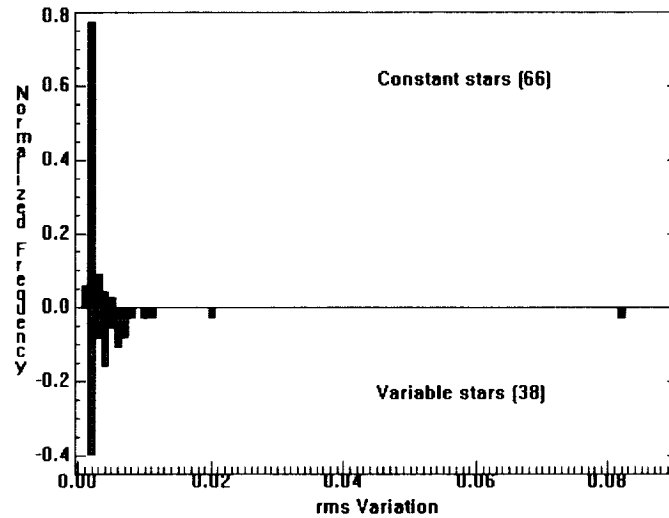


*Figure 1. Relative frequencies of stars found variable or constant on short timescales. From Lockwood et al., 1997.*

Figure 2 provides analogous information for year-to-year variations, except that we chose to display the peak-to-peak range of variation rather than the rms dispersion. The time interval from which this distribution was derived ranges from 7 to 11 years for the individual stars. The proportion of stars deemed variable is again about one-third. Stars that vary on short timescales tend also to vary on long timescales, although there are significant exceptions.
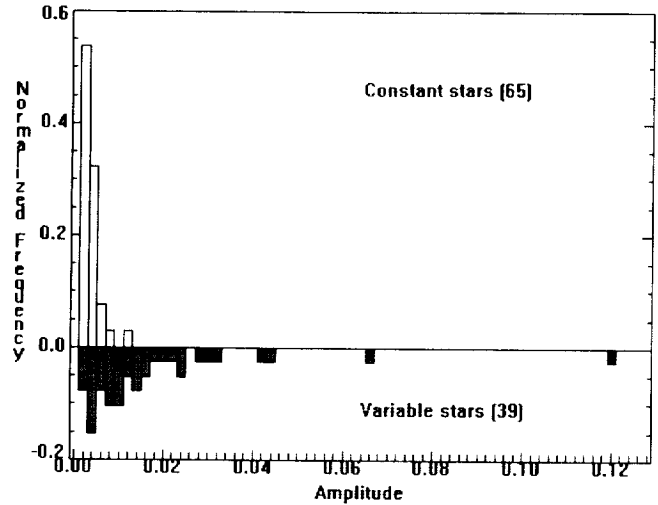
Constant stars (65)

Variable stars (39)

Amplitude

*Figure 2. Relative frequencies of stars found variable or constant on year-to-year timescales. From Lockwood et al., 1997.*

Figure 3 illustrates the demographics of observed variability for our program and comparison stars binned by spectral type and luminosity. Program stars are plotted below the central axis because they represent a sample biased toward increased variability by the high proportion of chromospherically active stars. An unbiased sample of field comparison stars lies above the line. The darkened portion of each bar represents the fraction of stars that we found to be variable.

Upper Panel: Field Stars
Lower Panel: MW Program Stars

Left Bar: Lum. Class IV-V
Center Bar: Lum. Class I-III
Right Bar: Lum. Class ?

Darker Shading =

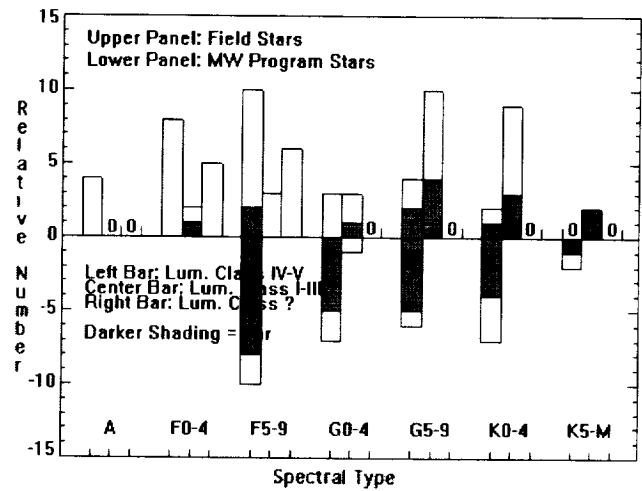A     F0-4     F5-9     G0-4     G5-9     K0-4     K5-M

Spectral Type

*Figure 3. Relative numbers of variable stars (shaded) and constant stars (unshaded) as a function of spectral type. Within each spectral type bin, separate columns are given for luminosity classes IV-V, I-III, and unknown, respectively. The Mount Wilson program stars are plotted below the central axis, and all other stars are plotted above the central axis. From Lockwood et al., 1997.*

Figure 4 illustrates the consequences of comparison star variability. There are 24 boxplots, one for each quartet group. Each boxplot indicates the inter-quartile range and median of the 2 σ values of

night-to-night variations of the most stable pair of stars in that group. Whiskers extend to the 90th percentile, and asterisks denote the more distant outliers.

Poisson noise is not a factor in any of the boxplots we show in this paper. The distributions, therefore, represent other errors plus intrinsic variability. Since the boxplots of Figure 4 typically arise from more than a hundred nights spread over a ten-year span, they robustly characterize night-to-night measurement error and intrinsic variability where present. A distinct measurement error baseline near $2\sigma$, 0.004 mag is indicated by the dashed line. Boxes situated significantly above that line, therefore, signal the presence of slightly variable stars. The proportion of such boxes is consistent with the fraction of stars we find variable from other tests, about one-third. We claim, therefore, that *intrinsic variability of comparison stars is the principal impediment to precision differential photometry at the sub-1% level.*
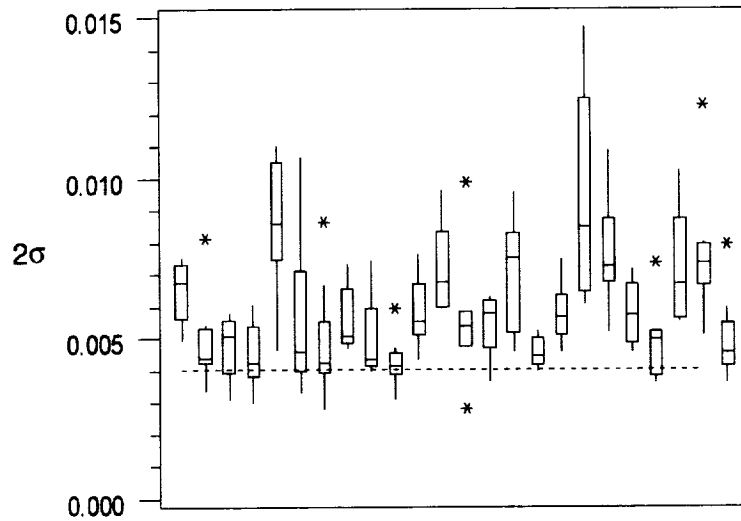


*Figure 4. Boxplots, one per quartet group arranged arbitrarily from left to right, show the distribution of the $2\sigma$ night-to-night dispersion of the differential magnitudes of the most stable pair of stars in each group. At least one star contributing to each boxplot is a comparison star. Each group, therefore, has a distinct internally defined baseline noise level.*

## Circumstances of the Observations

We now examine various observational circumstances to see if some hitherto unrecognized pattern of error may be revealed. Although the instrumental configuration remained essentially unchanged during the 25-year span of photometry at the 21-inch telescope, three events in the 1984–1995 interval are potential sources of trouble. We realuminized the telescope mirrors in February 1989, resulting in a 50% increase in count rates. We switched from a DEC minicomputer to a PC-based data system in September 1993; this also required replacement of the pulse counter circuitry. Finally, to more easily accommodate the tracking errors of a sloppy telescope drive system, we decided after 1987 to use exclusively the larger of two star diaphragms previously interchanged from time to time. The choice of diaphragm had no effect on the errors, so we ignore that distinction in the analysis that follows.

We have faithfully adhered to a strict, unvarying measurement protocol, observing each member of a stellar quartet for six 10-second measurements with a single filter, either $b$ or $y$. These measurements constitute a "cycle" in which the star order is fixed: 1st comparison star with half weight (three integrations), program star, 2nd program star (or 3rd comparison star), 2nd comparison star, 1st comparison star with half weight. Each night, we measure two cycles in each filter in the order $y, b, b, y$—about 35 minutes work. Normally, the observations occur within an hour or two of transit.

Although the measurement scheme was rigorously controlled, other circumstances of the observations could vary. For example, the hour angle restriction applies a repeated seasonal pattern of transit times beginning at dawn at some point in the year and concluding at dusk several months later. There is, therefore, an accompanying pattern of average ambient temperature. In addition, there are random amounts of moonlight and sometimes light pollution from baseball fields less than 1 kilometer (km) away, variable seeing, scintillation, and extinction. Finally, the throughput of the telescope and photometer changes according to the cleanliness of the optics and other factors. In the remainder of this paper, we describe tests we made to uncover possible systematic effects associated with these varying circumstances.

**Temporal Factors**

We now consider factors—however implausible—that might contribute a sensible "signal" to the pattern of photometric errors. We begin by examining the order of measurement of the four quartet members within an 8-minute observation cycle. This analysis addresses the short-term stability of the photometer and sky transparency on a timescale of a few minutes. Figure 5 shows the distribution of short-term scatter of repeated differential measurements of two different star pairs within a group. The two boxplots on the left indicate variation of a star pair observed one right after the other in a cycle, stars 1 and 4. The two on the right indicate the variation of a pair, stars 2 and 4, whose measurements extend over the 8-minute duration of a cycle. Figure 5 shows that there is no penalty for spreading out differential measurements time intervals as long as 8 minutes.

Figure 6 shows the distribution of the scatter of nightly repeats of differential measurements. The distribution incorporates several components of error: imperfect telescope tracking, scintillation, seeing, photon noise (negligible in most cases), and sky transparency fluctuations. The tail beyond 0.005 mag is highly sensitive to the accumulated decisions by the observer about when to quit, the general rule being to cease observing when the raw count rate scatters by more than about 1%.

We now look for possible error patterns on longer timescales. Figure 7 shows that the overall temporal distribution of observations over 11 years is fairly uniform. This provides some assurance that the results of the following discussion will be free of sampling artifacts.

Figures 8 and 9 show the distribution of absolute cycle-to-cycle magnitude differences according to the time of night and the month of the year. Figure 8 hints at the possibility that the observations improve very slightly toward dawn. Is this possible? The median, upper quartile, and especially the number of outliers all report this intriguing tendency. There is a plausible cause related to the diurnal variation of local aerosol. In winter, a temperature inversion that strengthens through the night traps Flagstaff's fireplace smoke and other aerosols below the level of the observatory; in spring, strong diurnal winds die down at dusk and aerosols lofted during the day presumably settle out after dark.
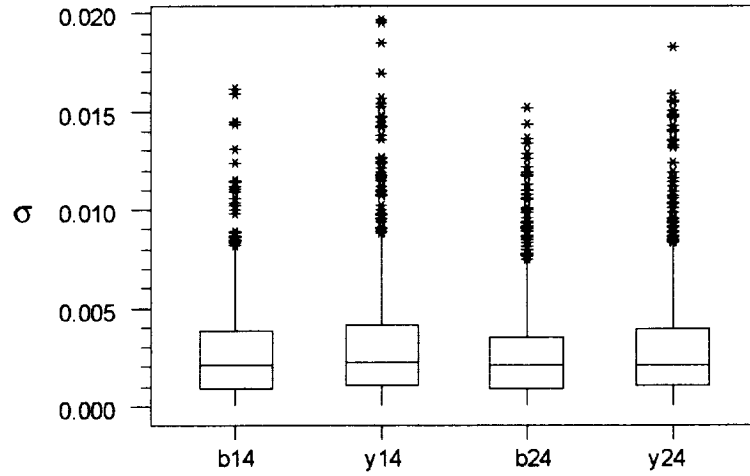
*Figure 5. These boxplots show no pattern of error that depends on the filter (b or y) or star order within cycles. Stars 1 and 4 (left two boxplots) are observed sequentially within 2 minutes; stars 2 and 4 (right two boxplots) are observed over an 8-minute interval.*
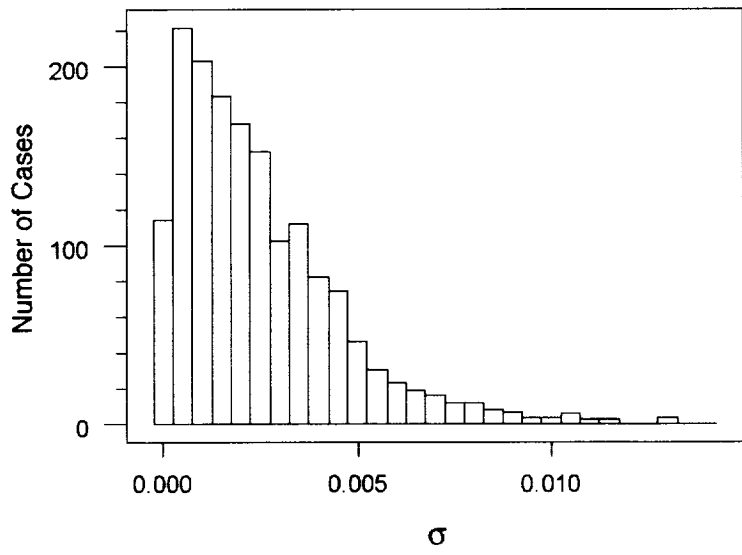


*Figure 6. Distribution of the scatter of differential magnitudes repeated a few minutes apart.*
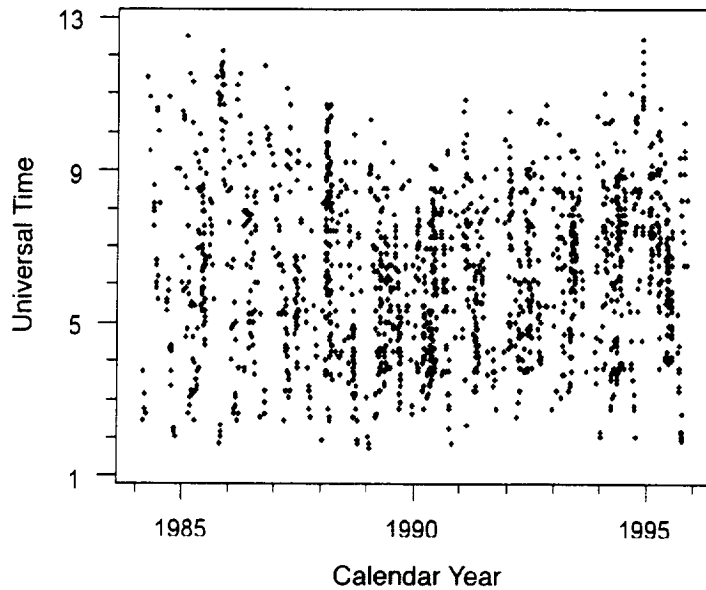
*Figure 7. Time of night of each observation plotted as a function of date. The density of observations is fairly uniform between 3 and 9 hours Universal Time (UT).*
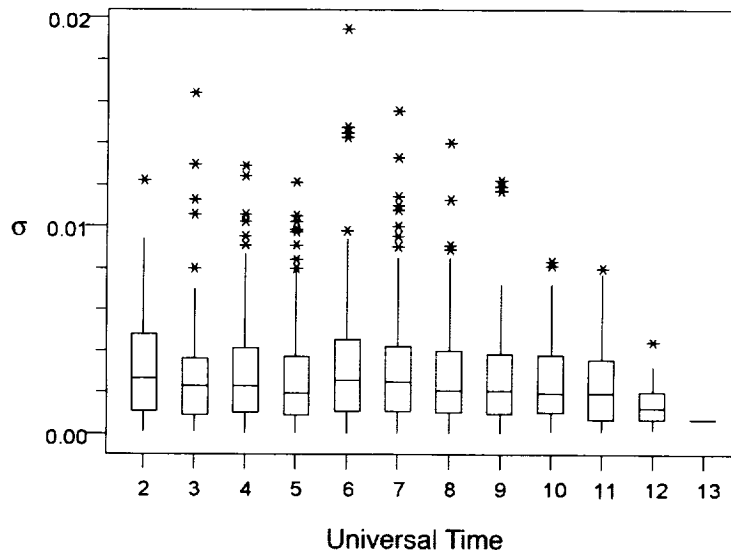


*Figure 8. The distribution of cycle-to-cycle repeats of differential magnitudes binned by UT hour from dusk to dawn.*

Figure 9 shows that there is no month-to-month pattern through the year. This is a bit surprising—we anticipated that the high extinction months from March to July might yield slightly less-precise data. They do not, despite a seasonal range of aerosol extinction ranging from near zero in winter to about 0.1 mag/airmass in spring.

*Figure 9. The distribution of cycle-to-cycle repeats of differential magnitudes by month of the year.*
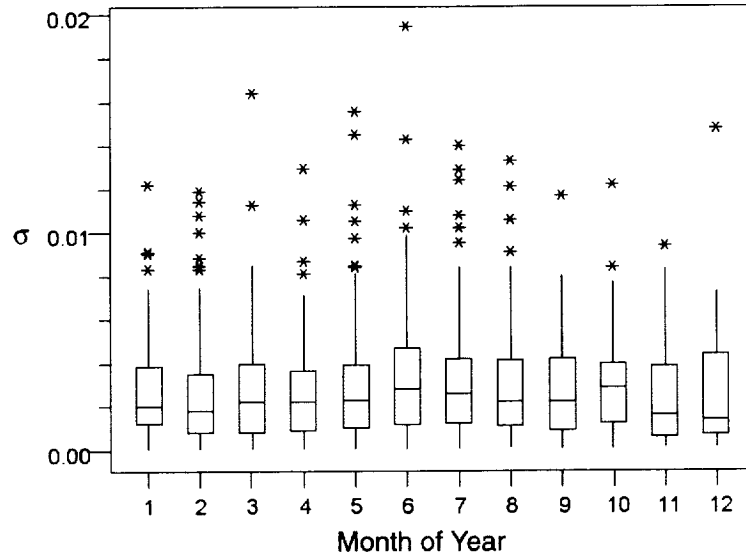
Finally, we look for a pattern of the 2σ night-to-night dispersion of the ensemble of all quartet groups binned by calendar year. The data for this exhibit are the same as shown on figure 4, but here we are looking for evidence of an error that affects all the photometry in some particular time interval. For example, we might expect to see a perturbation caused by the 1989 mirror aluminization or by the added extinction in 1992 from the Mount Pinatubo eruption (Thompson and Lockwood 1996). Figure 10 shows that after 1985 the median and lower quartile values are reasonably constant, with only a 20% range between the "best" and "worst" years. The upper quartiles shift around a bit, not surprising because there was a changing mix of comparison stars as we replaced the bad ones. Figure 10 thus provides assurance that the overall quality of the data remained constant.
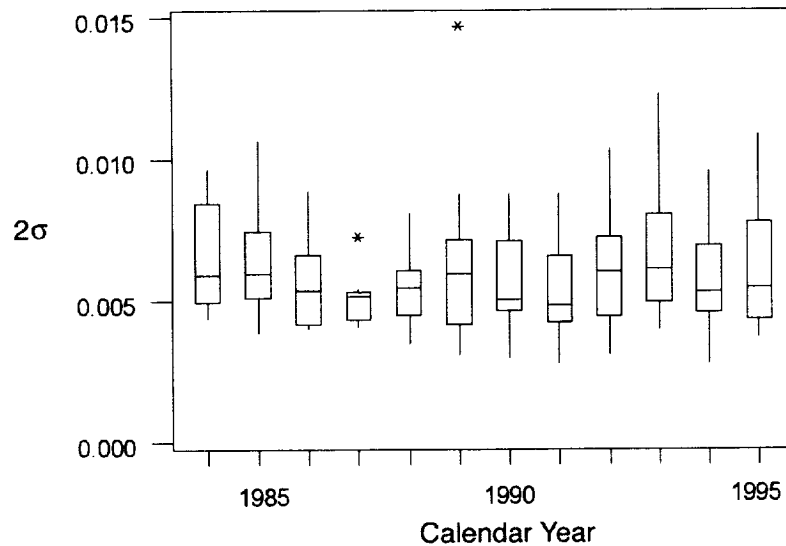


*Figure 10. Boxplots show the distribution of the 2σ night-to-night dispersion of the differential magnitudes of the most stable pair of stars in each group binned by calendar year. Compare to figure 4.*

We conclude that none of the particular temporal factors that we have examined imposes a perceptible pattern on the errors of observation.

## Location in the Sky

Does the airmass of the various stellar groups affect the attainable precision? All groups are observed near transit, but the individual declinations range from −12° to +65°, and the airmasses range from 1.0 to 1.5. Figure 11 shows the results for 14 quartet groups: indeed, there is a tendency for the higher airmass measurements (at the left side of the figure) to be slightly noisier.
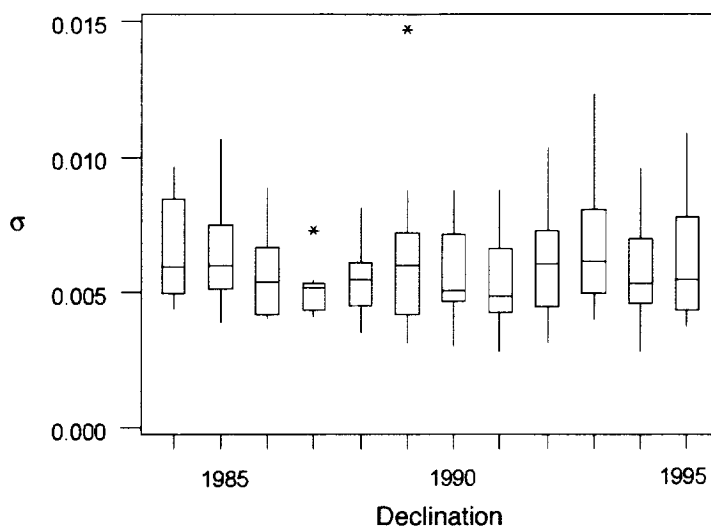


*Figure 11. The distribution of cycle-to-cycle repeats of differential magnitudes arranged from south by north by declination.*

## Instrumental Effects

We have remained alert to the possibility of low-level errors associated with the aging of the photomultiplier and the interference filters. Two types are easily envisioned, and with the extensive homogeneous data set now in hand, are straightforward to investigate. First, monotonic changes in the instrumental response, while compensated in the reductions, could have a residual component at the 0.001 mag level. Second, a pattern of diurnal or seasonal effects caused, for example, by ambient temperature variations, might emerge.

## Changes in Photometer Throughput

The throughput of the telescope and photometer changed over time, as indicated by values of the "zero point" of the magnitude system and by raw counts recorded each night from a $Sr^{90}$ Cerenkov source inside the photometer. These two records allow us to separate, if necessary, the optical and electronic components of the throughput (a distinction that has proven to be of little interest). Figure 12 shows nightly values of the 10-second raw $y$ counts for a typical star and sky background over 14 seasons, and figure 13 shows the ratio of $y$ to $b$. A big jump, accompanied by a change in the instrumental color response, occurred in 1989 when we renewed the mirror coatings. The 1992 drop was due to an adjustment in the operating voltage of the photomultiplier.
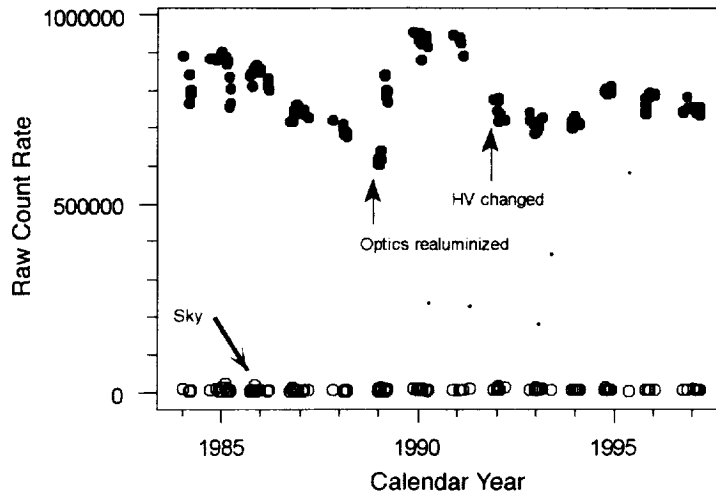
*Figure 12. The variations of the raw count rate for a representative star, over 14 years.*
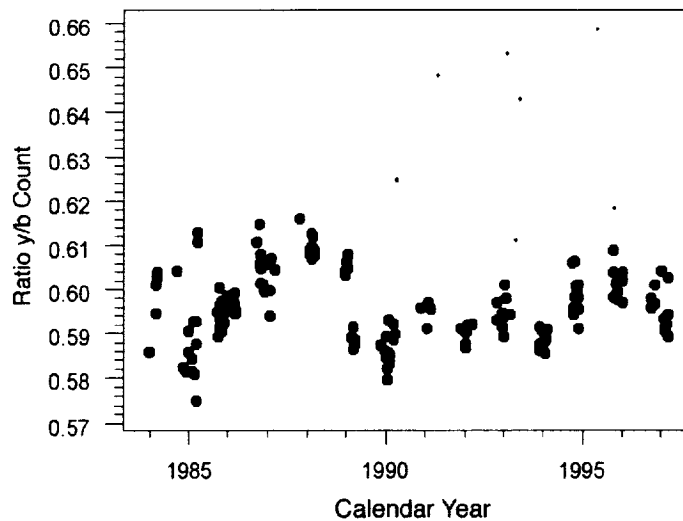


*Figure 13. Variation of the raw count ratio y/b for the same star shown on figure 12.*

These rather substantial variations of instrumental sensitivity did not affect the precision of the photometry at all. If they had, we could have seen evidence, for example in 1989, on figure 10.

**Variation of the Instrumental Color Correction**

Frequent determinations of the color-transformation coefficients early on and less frequent but regular measurements in recent years show that the color response of the photometer changes steadily, but at glacial speed. Over time intervals longer than a few years, the corrections became large enough to emerge from other sources of noise and must, therefore, be applied. If we omitted them, the effect would introduce spurious linear trends in the differential magnitudes of pairs of stars that differ widely in color.

18

The color coefficient for the *b* filter changed by 0.02 from 1985 to 1995. This means that for a star pair with $\Delta(b\text{-}y)$ = 0.2 (a typical value), the accumulated differential magnitude drift from 1985 to 1994 would be 0.02 x 0.2 = 0.004, hardly a negligible amount. The drift in *y* would be somewhat smaller. In recent publications (Lockwood et al., 1997, Radick et al., 1998), we took considerable pains to look for evidence of spurious linear brightness trends in our data. We found none.

**Temperature Effects**

Despite ample warnings (for example, Young 1963, 1967), thermal effects in photoelectric photometry are often ignored. While our photomultiplier tube is maintained at −15 degrees Centigrade (°C) year-round by thermoelectric cooling, the interference filters are exposed to 20 °C diurnal and 30 °C seasonal ambient-temperature variations. Nevertheless, previous efforts to uncover a temperature-related data artifact have produced nothing of significance. According to Young (1967), a passband drift on the order of 0.1—0.2 angstroms (Å)/°C is expected for intermediate-band interference filters such as ours. We now revisit the question of temperature effects anew using a 14-year data series.

For differential photometry, a worst-case scenario involves pairs of stars differing greatly in *b-y* color observed over a large seasonal temperature span; for example, February to June. We picked four star pairs for analysis, two closely matched in color and two whose *b-y* colors differed by about 0.4 mag. In each case, observations began in late winter and ended in early summer. Figure 14 shows the temporal circumstances for the HD114710 group, and figure 15 shows that the corresponding ambient temperatures ranged over 30 ° C.
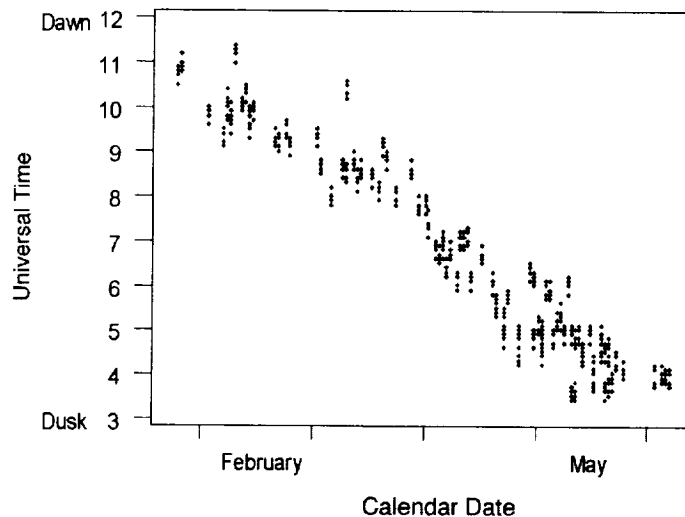


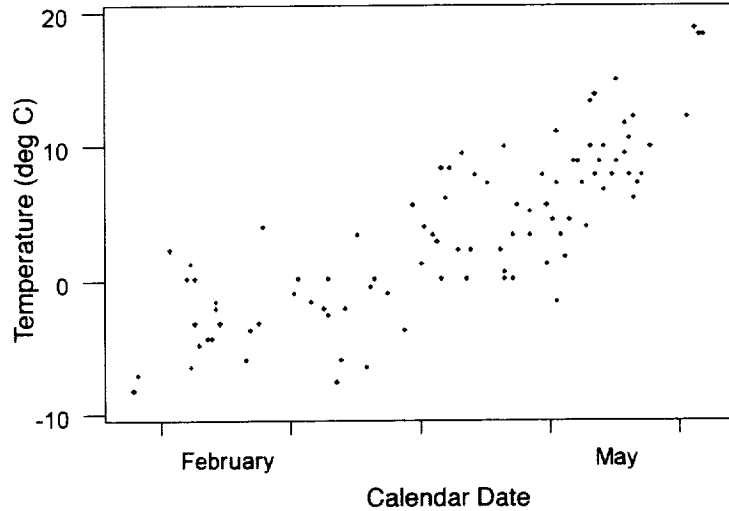*Figure 14. UT time of observation for the HD114710 group as a function of calendar date.*

*Figure 15. Ambient temperature in °C at the time of observation for the HD114710 group.*

On figures 16 and 17, we look for evidence of a temperature effect by plotting the night-to-night deviations from the seasonal mean as a function of the temperatures shown on figure 15. Solid lines indicate the unweighted linear regression and dashed lines indicate the 95% confidence band. For $b$ (figure 16), the slope is 0.00011 mag/°C (significantly nonzero with 99% confidence); for $y$ (figure 17), it is 0.00007 mag/°C (significantly nonzero with 95% confidence). Therefore, in both cases we find a bona fide temperature effect. Surprisingly, however, the effect contributes negligibly to the total variance, only 1.5% for $b$, and 4.2% for $y$. A second star pair, with $\Delta(b\text{-}y) = 0.3$, showed a similar temperature sensitivity, and two pairs with $\Delta(b\text{-}y) <0.02$ showed no effect at all.

We conclude, therefore, that the barely detectable temperature effect has no practical consequences. In other words, it appears to us that controlling the temperature of the interference filters (hitherto a benignly neglected fine point of photometric technique) would not improve our photometry. For the star pair illustrated here, among the most stable stars we measured, the bulk of the observed variance must be due to other causes. Among those, Poisson noise is excluded—we calculate that to be only ±0.0006 mag in $b$ and ±0.0008 mag in $y$.

We now generalize this result to our entire sample of 41 program stars and their preferred comparison stars. Figure 18 shows the circumstances for each pair. The abscissa is the color difference for the pair, $\Delta(b\text{-}y)$ and the ordinate is the nominal seasonal temperature range based on average Flagstaff maximum/minimum temperature data. Contour lines based on the temperature coefficients found above indicate the seasonal range of differential magnitude variation expected for $b$ and $y$. Only six stars (the ones lying above the $b = 0.001$ line) would experience a 0.001 mag or larger temperature drift in $b$, and none in $y$. Moreover, assuming the observations are uniformly distributed in ambient temperature, the rms variations would be a factor of approximately three smaller.

20
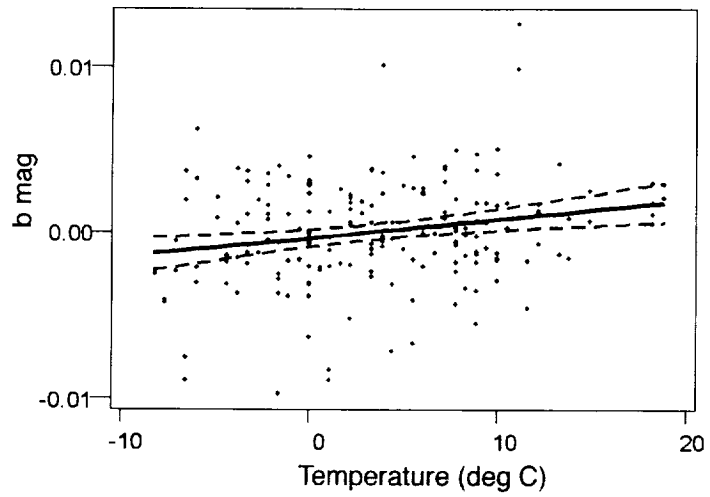
*Figure 16. Seasonal b magnitude residuals as a function of ambient temperature for a star pair in the HD114710 group with Δ(b-y) = 0.4.*
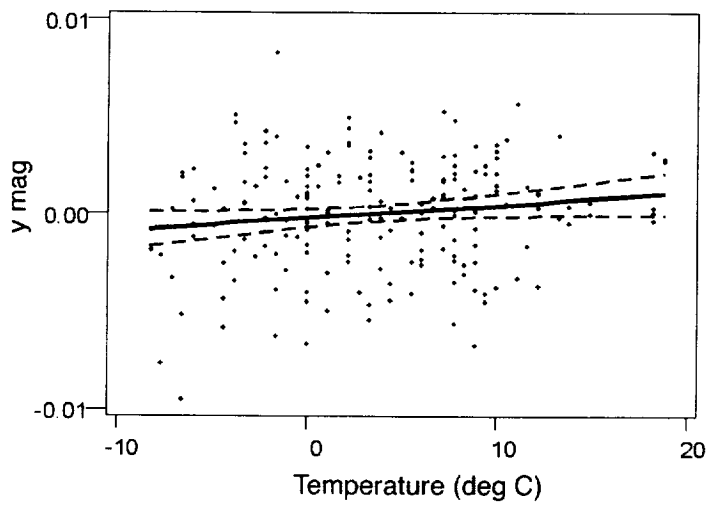


*Figure 17. Seasonal y magnitude residuals.*
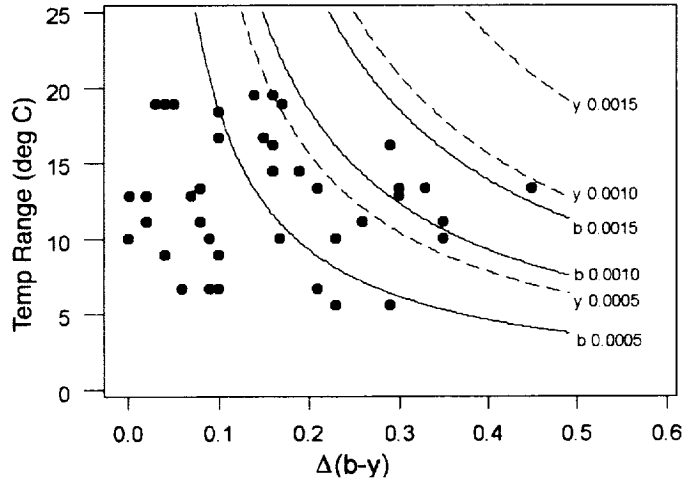
*Figure 18. Contour lines indicate amounts of the seasonal range of error expected in b and y according to color difference and seasonal temperature range. The plotted points correspond to 41 program stars in the study by Lockwood et al., 1997.*

Our analysis substantially diminishes the stature of the temperature variation, but does not dismiss it entirely. As a practical matter, however, we find no convincing evidence that a temperature effect degraded our photometry.

## Acknowledgments

# References

Jerzykiewicz, M.; and Serkowski, K.: Lowell Obs. Bull., vol. 137, no. 6(137), 1966, pp. 295–323.

Lockwood, G. W.; Skiff, B. A.; and Radick, R. R.: Astrophys. J., vol. 485, 1997, pp. 789–811.

Lockwood, G. W.; and Thompson, D. T.: Icarus, 1999, in press.

Radick, R. R.; Lockwood, G. W.; Skiff, B. A.; and Baliunas, S. L.: Astrophys. J., Suppl., vol. 118, 1998, pp. 239–258.

Thompson, D. T.; and Lockwood, G. W.: Geophys. J. Lett., vol. 23, 1996, pp. 3349–3352.

Thompson, D. T.; and Lockwood, G. W.: J. Geophys. Res. Planets, vol. 97, 1992, pp. 14761–14772.

Young, A. T.: Appl. Optics, vol. 2, 1963, pp. 51–60.

Young, A. T.:. Monthly Notices of the Royal Astronomical Society, vol. 135, 1967, pp. 175–180.

24

# Techniques for Automated Single-Star Photometry

Gregory W. Henry

*Center of Excellence in Information Systems,*
*Tennessee State University*
*Nashville, TN 37203*

## Abstract

Tennessee State University operates several automatic photoelectric telescopes (APTs) located at Fairborn Observatory in the Patagonia Mountains of southern Arizona. The APTs are dedicated to photometric monitoring programs that would be expensive and difficult to accomplish without the advantages of automation. I review the operation of two of the telescopes (a 0.75- and 0.80-meter (m) APT) and the quality-control techniques that result in the routine acquisition of single-star differential photometry with a precision of 0.001 mag for single observations and 0.0001-0.0002 mag for seasonal means. I also illustrate the capabilities of the APTs with sample results from a program to measure luminosity cycles in sun-like stars and a related program to search for the signatures of extrasolar planets around these stars.

## Introduction

For the past decade, astronomers at the Tennessee State University (TSU) Center of Excellence in Information Systems have been developing the capability to make photometric, spectroscopic, and imaging observations with automatic telescopes. As part of that effort, I have established a program to monitor stellar brightness changes in a variety of stars with automatic photoelectric telescopes (APTs). The telescopes are located at the Fairborn Observatory site in southern Arizona (figure 1). Fairborn is a private, nonprofit foundation headed by Lou Boyd that has designed, built, and operated automatic telescopes for various institutions for more than 15 years. The telescopes and their photometers operate automatically without human oversight. A site-control computer, interfaced to a weather station, opens the observatory at the beginning of each night if conditions are suitable and signals the individual telescope-control computers to begin observing. The site computer monitors weather conditions during the night and directs the observatory to close whenever conditions deteriorate. The telescopes receive their observing instructions over the Internet from TSU, and the resulting data are returned automatically each morning. The efficiency of the automatic telescopes allows extensive quality-control and calibration measurements to be made each night to maximize the precision of the observations.

Table 1 lists the four APTs currently in the TSU program, along with the number of years they have been operating, the number of observations they have collected, and the type of stars they are monitoring. The 0.75- and 0.80-meter (m) APTs are dedicated to long-term observations of 150 sun-like stars in order to detect subtle brightness changes that accompany their decade-long magnetic cycles. This effort is part of a collaboration with the Harvard-Smithsonian Center for Astrophysics and the Mount Wilson Observatory (Baliunas et al., 1998) and build upon a similar program of manual photometry at Lowell Observatory begun in 1984 (Lockwood, Skiff and Radick, 1997). The detection and characterization of luminosity cycles in a large sample of stars similar to the sun may help us to understand long-term changes in the sun and their effects on Earth's climate (e.g., Soon, Posmentier and Baliunas, 1996).

Table 1. Automatic telescope observations summary (through July 1998)

| APT, meters | Years | Group observations | Program |
|---|---|---|---|
| 0.25 | 12 | 73,052 | Semiregular variables |
| 0.41 | 11 | 131,172 | Chromospherically active stars |
| 0.75 | 6 | 29,579 | Lower-main-sequence stars |
| 0.80 | 3 | 13,785 | Solar-duplicate stars |
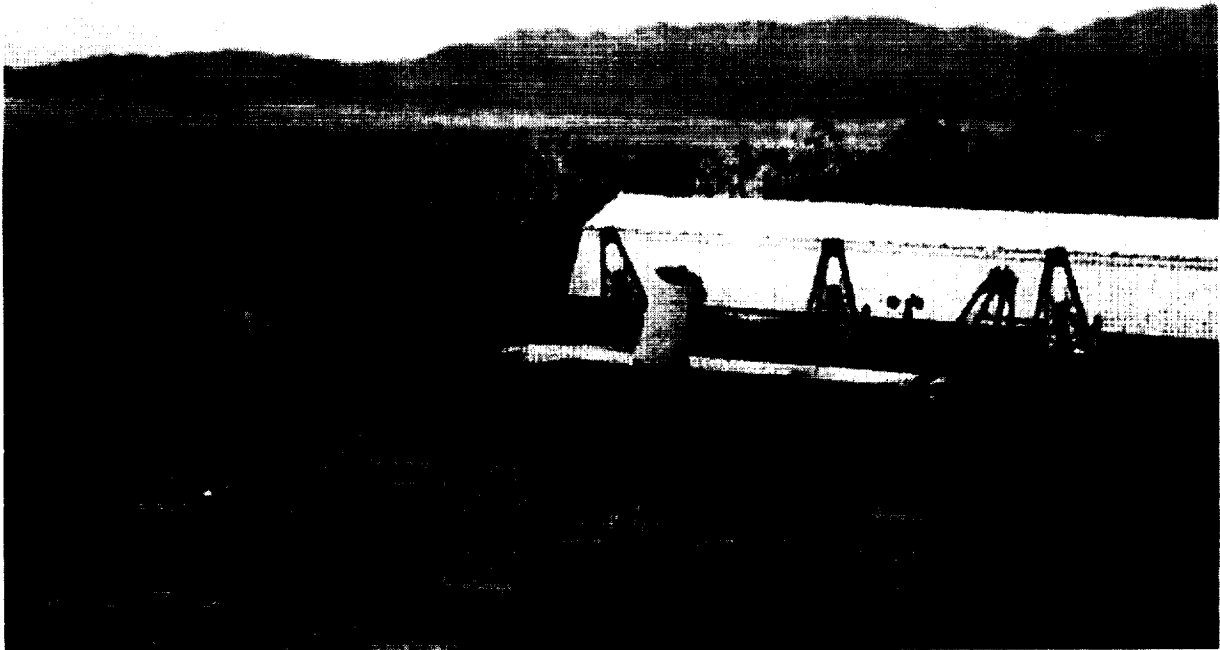


*Figure 1. The automatic-telescope observing site at an altitude of 5700 feet (ft) in the Patagonia Mountains of southern Arizona. Currently, eight operating telescopes owned by various institutions are housed in two roll-off-roof enclosures (shown in their open positions). The 0.75- and 0.80-m APTs, used to monitor brightness changes in sun-like stars and to search for extrasolar planets, are the rightmost two telescopes in the picture. Four additional TSU telescopes (three 0.80-m APTs and a 0.61-m automated imaging telescope (AIT) are under construction in the third (closed) shelter in the background. TSU's new 2.0-m automatic spectroscopic telescope (AST) (Eaton, 1995) is also under construction in its own enclosure nearby.*

Recently, the discovery that several of these sun-like stars host planetary systems has provided added interest to the study of their brightness changes (e.g., Henry et al. 1997).

## The Automatic Telescopes and Photometers

The 0.75-m and 0.80-m telescopes are of similar construction. The horseshoe equatorial mounts and open-tube superstructures were designed by Boyd and fabricated by Rettig Machine Shop of Redlands, California. Both APTs have disk-and-roller drives on both axes driven by stepper motors through sprocket-and-belt reduction systems. The Cassegrain optics were manufactured by Star Instruments of Flagstaff, Arizona. The primary mirrors have f/2 focal ratios; the effective focal ratios are f/8. Boyd, with help from Don Epand (also at Fairborn), produced the control systems that automate the telescopes and photometers. The 0.80-m APT is shown in figure 2.

Both telescopes are equipped with automated photometers: a single-channel photometer on the 0.75-m APT and a two-channel photometer on the 0.80-m. Both were designed and built by Boyd. The optical layout of the two-channel photometer on the 0.80-m APT is shown in figure 3. All components in the figure, as well as the voltage-divider chains and the preamplifier/discriminators for both channels, are contained within an insulated and sealed enclosure maintained at a constant temperature of 33 degrees Fahrenheit (°F) via a liquid coolant bath supplied by an external chiller. In addition to the temperature stabilization, filtered and dried air constantly flows through the photometer to control dust and humidity. Light from the telescope enters through a fused-silica window in the top of the photometer. Between this entrance window and the focal plane is a filter wheel that contains a selection of neutral-density filters that attenuate the light from bright stars. In the focal plane, a diaphragm wheel provides a selection of diaphragm sizes between 30 and 90 arcseconds as well as a fully open position for target acquisition and a closed position that acts as a dark slide. After passing through the diaphragm, the light beam encounters a flip mirror that directs the light either through a transfer lens to a Pulnix 840N charged coupled device (CCD) camera for rapid and accurate centering of target stars in the diaphragm or toward the detectors. In the detector path, the light first passes through a fused-silica Fabry lens and is then split into two beams by a dichroic mirror. Strömgren $b$ and $y$ pass bands are measured simultaneously by two EMI 9124QB bi-alkali photomultiplier tubes operated at −1200 volts (V) provided by two external high-voltage power supplies. The Strömgren $b$ and $y$ filters are fixed directly in front of the cathodes of the phototubes. The single-channel photometer for the 0.75-m APT is very similar except that a single EMI 9124QB phototube measures a star sequentially through Strömgren $b$ and $y$ filters located on an additional filter wheel.

## Program-Star Observations

Program stars on the 0.75- and 0.80-m APTs are each observed with three nearby (on the sky) comparison stars in the sequence:

DARK, A, B, C, D, A, SKY$_A$, B, SKY$_B$, C, SKY$_C$, D, SKY$_D$, A, B, C, D

termed a program-star group, where A, B, and C are the comparison stars, and D is the program star. Integration times are 20-30 seconds (sec) (depending on stellar brightness) on the 0.75-m APT, where the Strömgren $b$ and $y$ observations are made sequentially, and 40 sec on the 0.80-m APT where the two bands are measured simultaneously. A 45-arcsecond diaphragm is generally used for all integrations unless an optical companion needs to be excluded with a smaller diaphragm. The observations are reduced differentially with the standard equations of Hardie (1962) to form six sets of differential magnitudes: (D–A), (D–B), (D–C), (C–A), (C–B), and (B–A). These differential magnitudes are corrected for deadtime and differential extinction and transformed to the Strömgren photometric system with coefficients determined from quality-control observations described in the next section. The program-star observing sequence results in three measures of each of the six differential combinations in both the $b$ and $y$ colors. The three measures of each combination are averaged to form the group mean differential $b$ and $y$ magnitudes, which are treated as single observations in subsequent analysis.

*Figure 2. The 0.80-m APT at Fairborn Observatory. This telescope, along with a similar 0.75-m APT, is dedicated to a long-term program of monitoring luminosity cycles in sun-like stars. The black box mounted behind the primary mirror is the automated photometer.*

Each program-star group requires about 13 minutes of telescope time to complete, so approximately 40 program groups can be completed on an average night by each telescope. The groups are observed once each clear night throughout their observing seasons. Each APT can accommodate approximately 75 program stars on its observing menu, distributed more or less evenly throughout the 24 hours of right ascension. Observations are generally made only when the air mass is less the 1.5. Therefore, declinations must lie north of about −15° for highest precision.
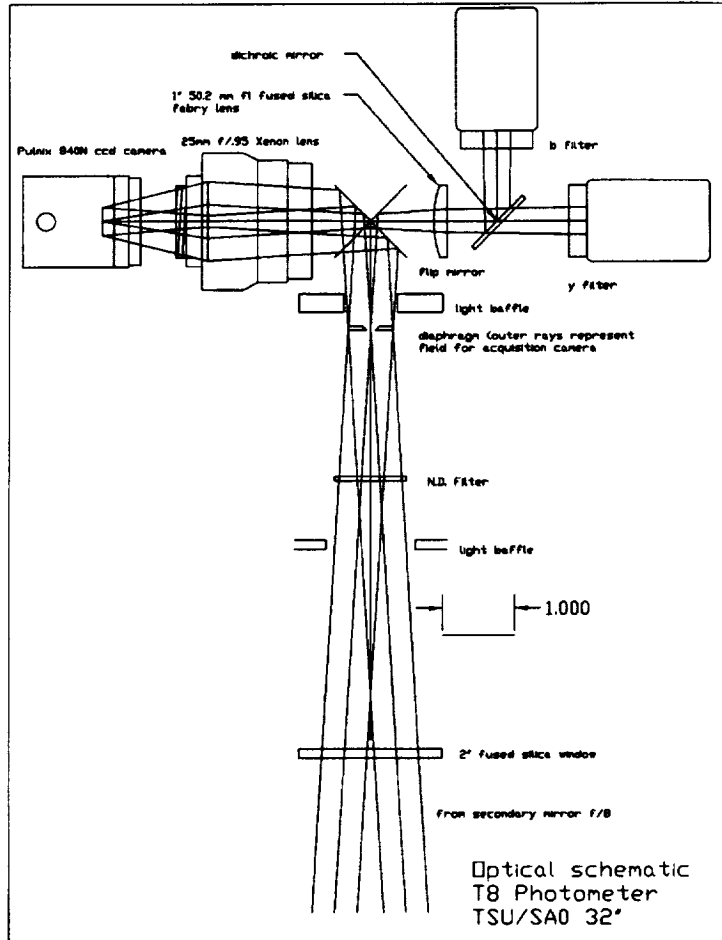
*Figure 3. Optical layout of the two-channel photometer on the 0.80-m APT. The CCD camera allows rapid and accurate centering of the star image in the focal-plane diaphragm, while the dichroic mirror allows two separate photomultiplier tube detectors (PMTs) to obtain simultaneous observations in the Strömgren b and y pass bands.*

## Quality-Control Observations

The combination of stable, dedicated instrumentation and the ability to make extensive quality-control observations each night on each telescope allows the maximum photometric precision of the APTs to be achieved and maintained over the long term. The quality-control observations take the form of additional group observations designed for specific purposes. Deadtime-group observations provide data for the determination of the system deadtime coefficients. Observations of standard-star groups are used to derive extinction, transformation, and zero-point coefficients. Dark counts are made as part of each program-star observing sequence (see above), and Fabry-scan groups are run each night for additional diagnostic purposes. These quality-control observations require only 5% to 10% of the telescope time each night, so they have relatively little impact on the number of program stars that can be observed. They are described in the following paragraphs.

Each night's quality-control observations are reviewed the next morning as part of the daily data-reduction process. Daily review of the data ensures that any problems with the APTs are quickly recognized (by me) and corrected (by Boyd). A series of reduction programs scan through the output file from each telescope and display the results at the computer, starting with the dark counts. Monitoring the dark counts is useful for recognizing such things as changes in PMT characteristics, failures in the temperature-control systems, and other miscellaneous problems (e.g., mice chewing through the coolant and dry-air supply hoses). Figure 4 shows the dark counts from two nights on the 0.75-m APT. The top panel reveals the normal 2-3 cps (median) count rate observed when the system is operating properly; variations in the dark counts shown in the bottom panel were traced to inadequate coolant flow caused by a leak in the external cooler.



Julian Day Fraction
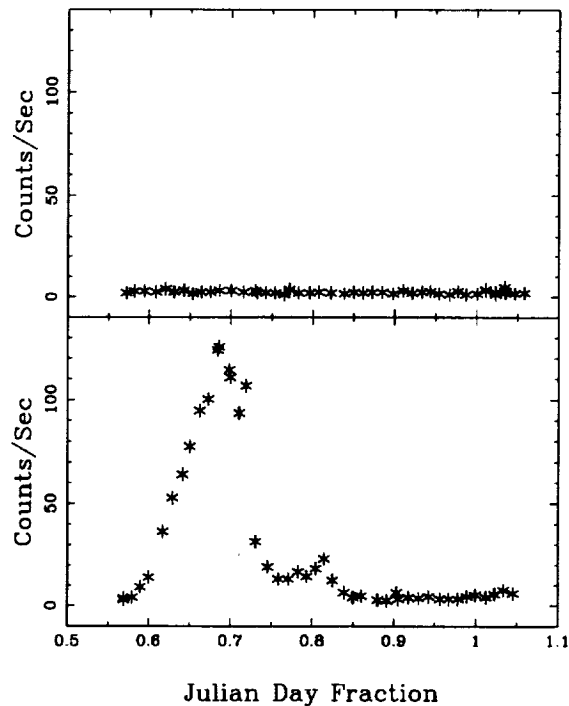
*Figure 4. Dark counts on two nights from the 0.75-m APT. Count rates of 2-3 counts per second (cps) (median) seen in the top panel are normal for the photometer temperature of 33° F and operating voltage of –1200V. Variable dark counts in the bottom panel were due to inadequate coolant flow to the photometer caused by a coolant leak.*

The reduction routines next display the result of the night's Fabry scan, one of the most useful tests of the operation of the APTs. The Fabry lens is designed to project a fixed image of the primary mirror of the telescope onto the cathode of the photomultiplier tube. Therefore, small deviations in the position of a star in the focal-plane diaphragm during an integration will not cause significant changes in the measured signal. There are three Fabry-scan groups on each APT observing menu, spaced at eight-hour intervals in right ascension. Therefore, one of them can be observed on any night of the year near its meridian crossing. The Fabry-scan groups command the telescope to center a relatively bright star and then move it just outside the diaphragm. The telescope then steps the star through the center of the diaphragm in right ascension while the photometer takes an integration at each step. The telescope recenters the star and performs a similar scan across the diaphragm in declination. The results from two

nights are shown in Figure 5, where the right ascension and declination scans in each case have been offset vertically for clarity. The top scan shows not only that the signal is constant as the star is moved through the diaphragm, but also that the telescope is properly focused and collimated and that the star is being properly centered in the diaphragm by the CCD camera. The broad, asymmetrical wings of the scan in the bottom panel reveal that the telescope is poorly focused and poorly collimated. Currently, there are no auto-focus or auto-collimation routines on the APTs, so this condition requires manual adjustments by Boyd. However, errors in focus and collimation can be detected by this technique and corrected before they affect the precision of the photometry.

Steps (2 Arcseconds)
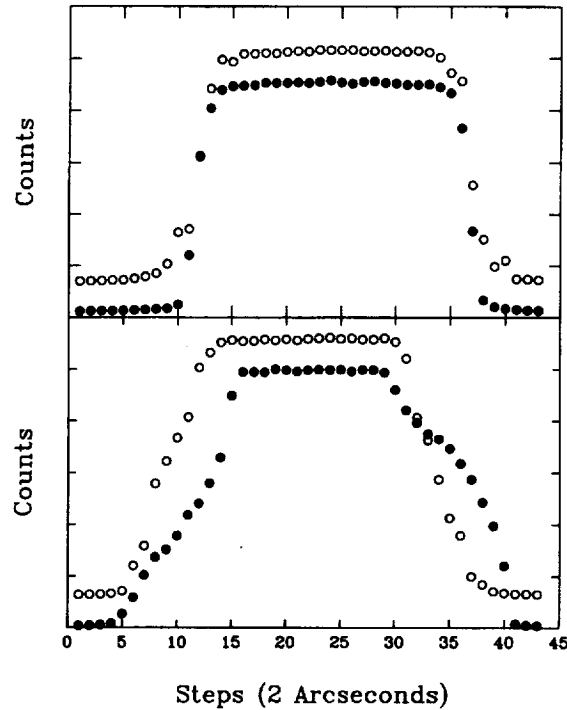
*Figure 5. Sample Fabry scans from the 0.75-m APT. The top panel shows the telescope is properly focused and collimated and that stars are being properly centered in the diaphragm. The bottom panel reveals that the APT is poorly focused and collimated.*

Three deadtime groups, spaced on the sky at eight-hour intervals and observed whenever they cross the meridian, permit the nightly determination of the photometer deadtime coefficients. These groups consist of two stars, one bright enough to provide a count rate of approximately 500,000 cps and a second, nearby star a magnitude or so fainter. Integrations on both stars through all the available neutral-density filters provide the data needed to derive the deadtime coefficient and to calibrate the neutral-density filters (as well as to verify the proper operation of the filter wheels). The daily APT-reduction routines scan through the output file for all deadtime groups and add the nightly results to deadtime coefficient files. Table 2 gives the yearly means of the deadtime coefficients for the first five years of the 0.75-m APT operation. Because a slow change in those coefficients is observed over time, all observations of standard and program stars are reduced with yearly mean deadtime coefficients.

31

Table 2. Yearly mean deadtime and transformation coefficients for the 0.75-m APT

| Year | Deadtime, (nanoseconds) | $b$ Transformation (mag) | $y$ Transformation (mag) |
|---|---|---|---|
| 1993–94 | 36.1 ± 0.5 | 0.0493 ± 0.0007 | 0.0160 ± 0.0006 |
| 1994–95 | 35.5 ± 0.5 | 0.0491 ± 0.0007 | 0.0161 ± 0.0006 |
| 1995–96 | 33.6 ± 0.4 | 0.0508 ± 0.0007 | 0.0152 ± 0.0007 |
| 1996–97 | 33.2 ± 0.5 | 0.0523 ± 0.0008 | 0.0158 ± 0.0007 |
| 1997–98 | 32.7 ± 0.4 | 0.0549 ± 0.0007 | 0.0162 ± 0.0007 |

As a final step before beginning program-star reductions, the daily reduction routines search through the output file to find all standard-star groups to compute the night's extinction, transformation, and zero-point coefficients. Sixty Strömgren standards from the list of Crawford and Barnes (1970) provide a uniform distribution around the sky and a range in color index. Each standard-star group consists of a single star, along with a sky position, to be observed in both the $b$ and $y$ colors. Many of the groups are observed at two or three different hour angles to provide a range of air mass. Typically, each telescope acquires 40 to 50 standard-star observations each night; they are reduced with least squares to solve simultaneously for nightly first-order extinction, transformation, and zero-point coefficients. The reductions automatically reject from the nightly solution standard stars whose residuals exceed 3σ. The final solution must meet the following criteria: root mean square (rms) less than 0.03 mag; number of stars in the final solution must be 20 or more; air mass must cover the range 1.0 to at least 1.8; and the range in Strömgren $(b - y)$ color index must exceed 0.6 mag. If the solution passes these criteria, the night is considered to be photometric, and the resulting coefficients are saved.

Five years of nightly Strömgren $y$ extinction coefficients from the 0.75-m APT are shown in Figure 6. Gaps in the coverage result because the APTs do not operate during Arizona's summer rainy season; each observing year runs from about mid-September to early the next July. Seasonal variations are clearly seen in the extinction coefficients. The slight overall decline during the first three years (the 1993–94 through 1995–96 seasons) resulted from residual effects of the Mt. Pinatubo eruption in the Philippines in June 1991. The slight increase in extinction in the last two seasons (1996–97 and 1997–98) was due to the relocation of the APTs from Mt. Hopkins (altitude 7600 ft) to Fairborn's new site in the Patagonia Mountains (altitude 5700 ft). The program-star observations on the 0.75- and 0.80-m APTs are reduced with these nightly extinction coefficients.

Yearly means of the nightly Strömgren $b$ and $y$ transformation coefficients are shown in Table 2. The formal errors in the yearly means are all less than 0.001 mag. The $y$ coefficients show no significant change over five years; the $b$ coefficients show a trend of approximately 0.001 mag per year with the instrumental band pass getting slightly redder with time. This may be due to aging of the aluminum coatings on the primary and secondary mirrors, which lose reflectivity more rapidly at bluer wavelengths. Nightly observations of the program stars are reduced with these yearly mean transformation coefficients to remove the long-term trends in instrumental sensitivity. This means that final reduction of the program-star differential magnitudes and writing to the archives cannot be done until the end of each observing year in July when the mean coefficients for the year can be derived.
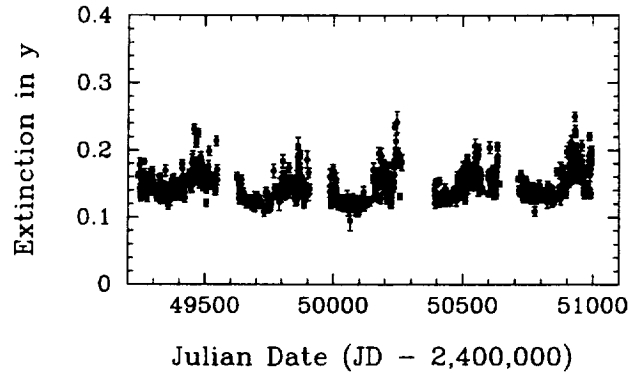
*Figure 6. Nightly Strömgren y extinction coefficients from the 0.75-m APT. Gaps in the record correspond to the summer rainy season in Arizona when the APTs are shut down. Seasonal variations in extinction are clearly seen; extinction is lowest during the winter months and highest during the spring windy season. Additional subtle effects are described in the text.*

Although the photometric zero points are not needed in the differential reductions of the program stars, they are, nevertheless, useful for tracking changes in system sensitivity. In particular, they are help in deciding when to clean the optics. Figure 7 shows two years of Strömgren y zero points from the 0.75-m APT. The zero points decrease slowly over several weeks as dust accumulates on the primary and secondary mirrors as well as on the entrance window of the photometer. When the sensitivity drops 5 to 10 percent (approximately every three months), the optics are washed and the zero points recover.
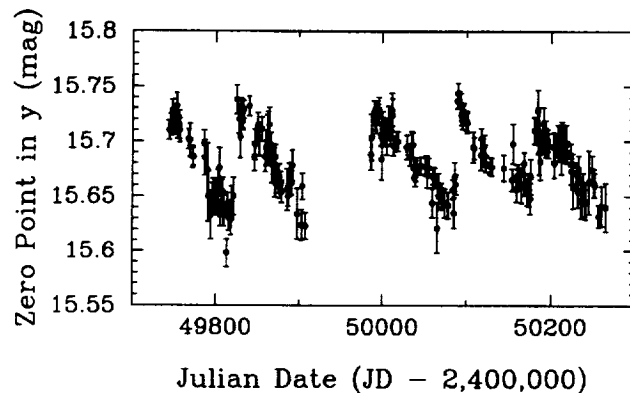


*Figure 7. Nightly Strömgren y zero points from the 0.75-m APT. The system sensitivity decreases several percent over several weeks as dust accumulates on the optics, and then recovers when the optics are washed.*

33

**Automatic Scheduling of the Observations**

The APTs have no provision for manual operation; there are no eyepieces with which to view the fields or control paddles to slew the telescopes. Observational requests are accepted only via ASCII input files containing such requests in the Automatic Telescope Instruction Set (ATIS) language. These files are communicated to the telescopes from TSU over the Internet. (The last leg of the link to the site is a dedicated phone line to an Internet point of presence in southern Arizona.) In ATIS, a group observation is the primitive unit to be scheduled and executed by the telescope. The various program-star and quality-control group sequences executed by the 0.75- and 0.80-m APTs have been described above. ATIS provides a detailed set of commands with which these group sequences can be composed, including commands to move the telescope to a specified target, acquire and center the star in the diaphragm, set the positions of the diaphragm and filter wheels, and make integrations in a specified sequence. Complete details of the ATIS language have been published by Boyd et al. (1993) as part of a special issue on ATIS in the *International Amateur-Professional Photoelectric Photometry Communications*. The control systems of the APTS interpret the ATIS commands and generate the hardware-control signals that carry out the requested observations.

In addition to specifying the syntax and semantics for composing group-observation requests, ATIS provides a set of group-selection rules that are used by the telescope-control software to determine the execution order of groups during the night. These rules operate on parameters specified by the observer and located in the header of each group-observation request. These parameters include the Julian Date range over which group observations should be made, the hour-angle limits that are suitable for the group, the number of times the group should be executed within a night, the moon status (up, down, or either) required for the group observation, and a priority. When the telescope is ready to make an observation, the ATIS scheduler first checks all group requests and determines which ones are currently enabled, i.e., which groups are within the limits specified by the group header. From among the enabled groups, any one of which *could* be executed next, the ATIS scheduler must select the one group that *will* be executed next. In a simple winnowing process, the scheduler first considers all enabled groups that have the highest priority level. Within that subset of enabled groups, it looks for the ones with the highest observation-request count. From among those, the scheduler selects the group that is closest to the end of its hour-angle window, implementing essentially a first-to-set-in-the-west policy. In the unlikely event that two or more groups are still tied for next execution, the scheduler simply picks the one that appears first in the ATIS request file. When a group observation has been completed, the scheduler repeats the same process to dispatch the next group for execution and continues doing so for the rest of the night.

This simple ATIS-dispatch scheduling procedure, which has been used successfully to schedule all of the Fairborn APTs, has several advantages. First, it is completely robust; i.e., the group selection rules will always converge to the selection of a unique group for execution unless all observation requests have been satisfied. In that case, the telescope simply pauses until additional groups become enabled (for instance, by moving into the beginning of their hour-angle windows) or the night ends. Second, the scheduler can recover easily from any interruptions due to clouds or equipment failure. Third, a set of groups covering the entire observable sky can be submitted at one time, and the ATIS scheduler will continually schedule the appropriate groups in season for as long as they remain on the observing menu. Fourth, by suitable use of small hour-angle ranges and higher priorities, the standard-star and other quality-control groups can be set up around the sky, and they will be interleaved with the program-star groups at the appropriate times. The higher priorities of the quality-control groups ensure the necessary calibration observations are always performed at the optimum times, but since they require only a few percent of the observing time, most of the time is still available for program-star observations. Finally, good schedules result from the ATIS scheduler if the telescope is properly loaded; i.e., when the observing requests contain a suitable density and distribution of groups on the sky. In such cases, the

APTs execute program-star groups beginning at the western limit in the early evening, working toward the meridian by local midnight, ending at the eastern limit at dawn, and interspersing higher-priority quality-control groups throughout the night as they become enabled. Although simple and robust, the ATIS scheduler is not without its limitations, and improved scheduling methods are under development for the automatic telescopes (e.g., Henry, 1996; Edgington et al., 1996).

## Precision of the Program-Star Observations

Since no human operator is on hand during data acquisition to monitor the photometric quality of the night, the APTs are programmed to collect data as long as they can find stars. Therefore, data taken under nonphotometric conditions must be recognized *ex post facto* because all program-star observations are written to the data archives. The first step is to employ a "cloud filter." Neither the comparison stars nor the program stars being observed with the 0.75- and 0.80-m APTs are expected to vary significantly over the several minutes it takes to obtain a program-star group observation. Therefore, the *internal* precision of a group observation, measured as the standard deviation of the mean differential magnitude, can be used to filter the data. Figure 8 plots the internal precision of all program-star group observations from the 0.80-m APT for the 1997–98 observing season against the air mass of the group observation. Most observations on good nights have internal precisions near 0.001 mag, although this increases slightly at higher air mass. Therefore, when extracting observations from the data archives for analysis, I use a 0.005-mage cloud filter for rejecting observations with uncertainties greater than this approximately $3\sigma$ limit. An entire group observation is rejected by the cloud filter if the internal precision of any of its six differential magnitudes in either color exceeds this limit.

Since the measurement of subtle brightness changes in sun-like stars requires data of the highest possible precision, further cleaning of the reduced data, beyond the cloud-filtering process, is necessary. This is accomplished by selecting only observations that were made on nights with good all-sky standard-star solutions. This ensures that the data used in an analysis were taken on good photometric nights and were reduced with well determined nightly extinction coefficients. These two filtering steps are done routinely and automatically whenever data are extracted from the archives. This results in the rejection of about half the observations, because the APTs collect data in both photometric and spectroscopic conditions. These automatic filtering techniques work very well and eliminate most of the poor-quality data. To identify any remaining outliers, correlation plots of the pairwise differential magnitudes are used to manually reject any remaining discrepant observations before a given data set is analyzed.

After program-star data are cleaned by this filtering process, their *external* precision can be determined. External precision is measured on two time scales: short term (night to night) and long term (year to year). Short-term external precision is measured as the standard deviation of a single group mean observation from the corresponding seasonal mean differential magnitude. This can be easily computed from observations of constant pairs of stars. Table 3 lists results from the 0.75-m APT from differential magnitudes of the constant stars HD 124570 (F6 IV) and HD 121560 (F6 V). Here, the yearly menu Strömgren $\Delta b$ and $\Delta y$ magnitudes have been combined into a single $\Delta(b + y)/2$ differential magnitude to increase precision, as done by Lockwood, Skiff, and Radick (1997) in their program of sun-like star photometry. Column 4 lists the short-term or nightly precision for each of the six observing seasons. The mean of those six standard deviations is 0.0014 mag, which I take to be the typical external precision of a single observation from the 0.75-m APT. A similar analysis of data from the same pair of stars for the first three years of operation of the 0.80-m APT gives 0.0011 mag for its short term external precision. This is slightly better than the 0.75-m APT because longer integrations are used with the 0.80-m two-channel photometer to reduce scintillation noise, which accounts for most of the APT measurement errors.
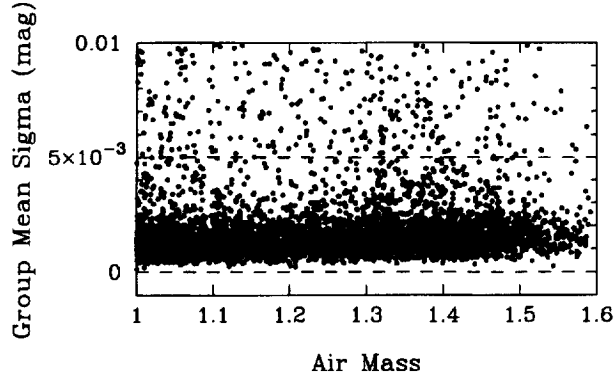
*Figure 8. Internal precision (measured as the standard deviation of the mean magnitude) of program-star observations from the 0.80 m APT for all nights of the 1997–98 observing season plotted against air mass. (Only those with a precision better than 0.01 mag are shown.) Each point corresponds to one complete program-star group observation. This distribution is used to derive the cloud-filter level of 0.005 mag, designated by the upper dashed line.*

The observations in table 3 also allow the determination of the long-term (year-to-year) external precision of the 0.75-m APT observations. This is measured as the standard deviation of the yearly mean magnitudes from the mean of the yearly means. The total ranges of the yearly means in Column 3 is only 0.0004 mag; the long-term external precision is 0.00015 mag. Thus, the observed long-term precision agrees with the predicted 0.0002-mag uncertainties in the yearly means from Column 5, computed as $\sigma_{short}$ divided by the square root of the number of observations for each year. This 0.0001–0.0002 mag level of precision is also reached by the 0.80-m APT for suitably constant pairs of stars.

Table 3. Yearly photometric $\Delta(b + y)/2$ means of the constant pair HD 124570/HD 121560 from the 0.75-m APT

| Year | $N_{obs}$ | Yearly mean (mag) | $\sigma_{short}$ (mag) | $\sigma_{mean}$ (mag) |
|------|-----------|-------------------|------------------------|------------------------|
| 1993 | 27 | −0.6315 | 0.0015 | 0.0003 |
| 1994 | 30 | −0.6317 | 0.0011 | 0.0002 |
| 1995 | 42 | −0.6319 | 0.0013 | 0.0002 |
| 1996 | 28 | −0.6316 | 0.0012 | 0.0002 |
| 1997 | 53 | −0.6315 | 0.0016 | 0.0002 |
| 1998 | 61 | −0.6316 | 0.0016 | 0.0002 |

**Variability in Comparison Stars**

The greatest impediment to routinely achieving the precision documented above is low-amplitude, intrinsic variability in the comparison stars (see also Lockwood, this volume). Criteria for the selection of comparison stars include closeness on the sky to program star; color index similar to the program star; brightness (8th mag or brighter to minimize errors arising from photon statistics); membership in a spectral class predominately populated by constant stars; and absence of known

variability. Most comparison stars were chosen from spectral class F, but numerous cooler stars were used as well, especially G and K giants. However, most of the comparison stars were selected before the release of the *HIPPARCOS CATALOGUE* (Perryman et al., 1997) and, therefore, without the improved parallaxes, magnitudes, color indices, and photometric variability statistics now available from *HIPPARCOS*. Many were chosen based only on their HD spectral classifications and proper motions.

Figure 9 shows observed short-term photometric variability of comparison and program stars from both APTs in the HR diagram. The *HIPPARCOS* magnitudes, color indices, and parallaxes were used to locate the stars on the diagram because nearly every star (714) had an entry in the *HIPPARCOS CATALOGUE*. Main-sequence stars redder than $B - V \sim 0.5$ are the program stars; the others are the comparison stars. Constant stars are plotted as small filled circles. Stars with $\sigma_{short} \geq 0.002$ mag are designated short-term variables and are plotted with open circles. A few new comparison stars with, as yet, undetermined photometric variability are plotted with x's. This 0.002-mag level of observable variability is derived from our observations of short-term variability in sun-like stars in figure 11 (below). In that sample, only stars younger than the sun have $\sigma_{short} \geq 0.002$ mag, and all stars older than the sun have $\sigma_{short} \leq 0.002$ mag, consistent with expected variability patterns in those stars. Therefore, observed $\sigma_{short} \geq 0.002$ mag in the APT observations implies that photometric variability has, indeed, been detected.



(B—V)o (mag)
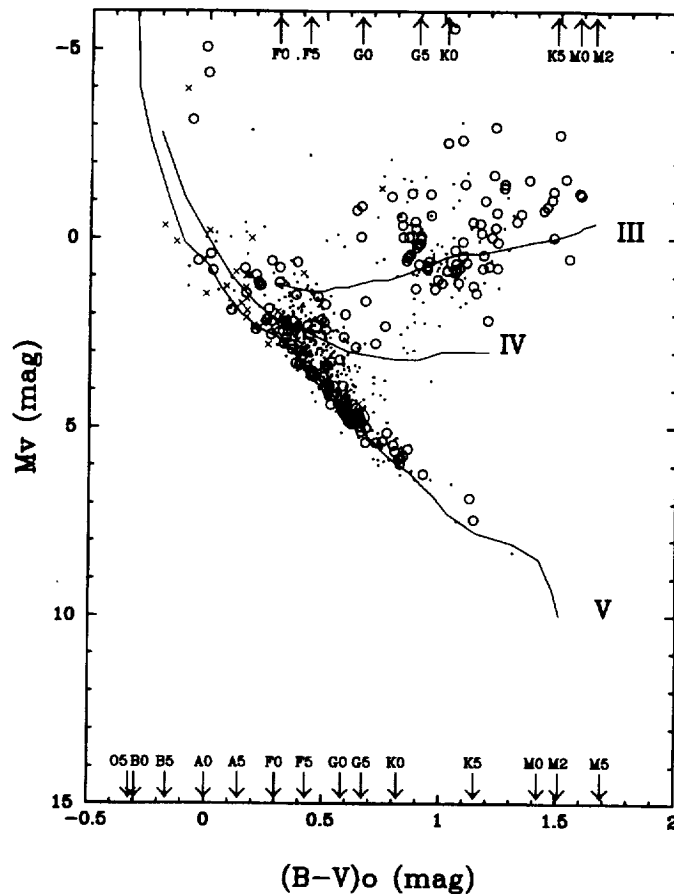
*Figure 9. Short-term photometric variability in the HR diagram of 714 comparison and program stars from both the 0.75- and 0.80-m APTs. Main-sequence stars redder than $B - V \sim 0.5$ are the program stars; the rest are comparison stars. Constant stars are plotted with small filled circles; stars with detectable short term variability ($\sigma_{short} \geq 0.002$ mag) are plotted as open circles. A few new comparison stars with undetermined photometric variability are plotted with x's.*

It is clear from figure 9 that low-amplitude, short-term variability occurs throughout the HR diagram. Young, lower-main-sequence (late F though K) program stars are variable because of their rapid rotation and dynamo-induced spot activity (e.g., Baliunas et al., 1998; Radick et al., 1998). Many of the comparison stars are F0–F8 dwarfs and subgiants, and short-term variability occurs in this range as well. At the cooler end of this range, the variability mechanism is probably still spot activity, because variability occurs predominantly in the stars closest to the zero-age main sequence (i.e., the youngest stars), as is the case for the program stars. Variability occurs in the early F (and late A) stars both on and above the main sequence. This variability arises from radial and nonradial pulsations in variables like the δ Scuti and γ Doradus stars (e.g., Aerts, Eyer and Kestens, 1998). Most of the G and K giants chosen as comparison stars are also short term variables. The variability mechanism in those stars is still unknown (Hatzes and Cochran, 1998).

These results on short-term variability are summarized in table 4 for various ranges of $B - V$ color index. Corresponding approximate spectral-type ranges given in the table are for main-sequence stars. Constant stars are most likely to be found in the $B - V$ range 0.4–0.5, corresponding to spectral types F4–F7, where only 8.6% of stars are variable from night to night. Among stars in $B - V$ later than 0.5 (F8 and later) are either the main-sequence program stars or the G and K giant comparison stars; both groups exhibit frequent variability. All stars redder than $B - V = 1.4$ were found to be variable. Stars bluer than $B - V = 0.3$ are also quite likely to be variable. Although the HIPPARCOS results are useful for locating candidate comparison stars on the HR diagram, it is unfortunate that the HIPPARCOS photometry lacks the precision to identify a priori which candidate comparison stars are low-amplitude variables. For instance, in a study of 187 of the G and K giant comparison stars, most of which were variable, Henry et al., (1999) found that only a few percent of the variables (those with amplitudes of 3% to 4% or greater) were identified as such in the HIPPARCOS CATALOGUE.

Table 4. Percentage of stars with short term variability ($\sigma_{short} \geq 0.002$ mag) as a function of $B - V$

| B – V range (mag) | Main sequence spectral type | $N_{stars}$ | No. variable (%) |
|---|---|---|---|
| –0.1–0.0 | B8–B9 | 2 | 0.0 |
| 0.0–0.1 | A0–A3 | 8 | 37.5 |
| 0.1–0.2 | A4–A7 | 8 | 25.0 |
| 0.2–0.3 | A8–A9 | 16 | 62.5 |
| 0.3–0.4 | F0–F3 | 57 | 29.8 |
| 0.4–0.5 | F4–F7 | 151 | 8.6 |
| 0.5–0.6 | F8–G0 | 132 | 18.9 |
| 0.6–0.7 | G1–G6 | 87 | 33.3 |
| 0.7–0.8 | G7–G9 | 29 | 24.1 |
| 0.8–0.9 | K0–K1 | 32 | 31.2 |
| 0.9–1.0 | K2–K3 | 47 | 34.0 |
| 1.0–1.1 | K4 | 37 | 35.1 |
| 1.1–1.2 | K5 | 27 | 40.7 |
| 1.2–1.3 | K7 | 18 | 66.7 |
| 1.3–1.4 | K7–M0 | 11 | 54.6 |
| 1.4–1.8 | M0–M8 | 16 | 100.0 |

These results seem to indicate that the best comparison stars should be chosen from the spectral range F4–F7. However, when excellent long-term stability is also required in the comparison stars, the choice is not so clear. Since long-term (year-to-year) variability can be measured to a precision of 0.0001–0.0002 mag with the APTs, many stars that are constant to 0.001 mag from night to night are still observed to vary significantly from year to year. Table 5 shows the percentage of stars with measurable long-term variability ($\sigma_{long} \geq 0.0005$ mag) derived from the 0.75-m comparison and program stars. The 0.80-m APT results are not included because it has not been operating long enough to characterize long-term variability. In the range F4–F7, where less than 10% of stars are short-term variables, nearly 60% have detectable long-term variability. A better place to find long-term stability is in the range F0–F3; even better odds occur at A8–A9. However, the chance for short-term variability in these ranges increases from less than 10% at F4–F7 to over 60% at A8–A9. The mid-F stars presumably have sufficient convection zones in which magnetic dynamos still operate and drive small, but significant, long-term brightness changes. The late-A and early-F stars lack the magnetic dynamo, but many are pulsating $\delta$ Scuti and $\gamma$ Doradus variables. The disappointing and frustrating result: there seems to be no location in the HR diagram where stars are likely to be found with the desired level of short- and long-term stability.

Since many of the program stars on the 0.75- and 0.80-m APTs are solar-age and older, with very small luminosity changes from year to year, the highest possible stability is needed in the comparison stars to resolve unambiguously the variability in the program stars. Consequently, as comparison stars are proven variable, they are replaced with new ones. The replacements are now chosen primarily from among the late-A and early-F spectral types, because long-term stability is so important. Although many will turn out to be new short-term variables, these can be identified in a single season and quickly replaced. Alternatively, if new comparisons are chosen from the F4–F7 stars, several years might pass before it becomes obvious that they are variable. The A8–F3 stars have a very good chance of exhibiting

Table 5. Percentage of stars with long term variability ($\sigma_{long} \geq 0.0005$ mag) as a function of $B - V$

| B – V range (mag) | Main sequence spectral type | $N_{stars}$ | No. variable (%) |
|---|---|---|---|
| 0.1–0.2 | A4–A7 | 4 | 0.0 |
| 0.2–0.3 | A8–A9 | 8 | 12.5 |
| 0.3–0.4 | F0–F3 | 30 | 36.7 |
| 0.4–0.5 | F4–F7 | 76 | 57.9 |
| 0.5–0.6 | F8–G0 | 61 | 59.0 |
| 0.6–0.7 | G1–G6 | 38 | 65.8 |
| 0.7–0.8 | G7–G9 | 14 | 57.1 |
| 0.8–0.9 | K0–K1 | 21 | 81.0 |
| 0.9–1.0 | K2–K3 | 17 | 70.6 |
| 1.0–1.1 | K4 | 9 | 33.3 |
| 1.1–1.2 | K5 | 9 | 66.7 |
| 1.2–1.3 | K7 | 2 | 100.0 |

long-term stability if they lack the short-term variability. In fact, even most of those *with* observable low-amplitude, short-term variability appear to be constant from year to year.

## Observations of Sun-Like Stars

The approximately 150 sun-like stars being monitored by the 0.75- and 0.80-m APTs are plotted in figure 10, which shows their distribution in the $logR'_{HK}$ (age) versus $B - V$ (mass) plane. Open circles are from the 0.75-m APT; filled circles are from the 0.80-m APT. The stars range in mass from about $1.3M\odot$ on the left to $0.7M\odot$ on the right. They range in age from 100 Myr at the top to 10 Gyr at the bottom. The chromospheric emission ratios ($logR'_{HK}$) are computed from the Ca II H & K index as defined and determined by the Mount Wilson HK Project (Baliunas et al., 1998). For comparison, the sun is plotted as a circled point at a $B - V$ of 0.642 and a $logR'_{HK}$ of –4.901. Most of the 0.80-m APT stars were selected to be close to the sun in both mass and age. Therefore, this plot does not represent the natural distribution of nearby sun-like stars.
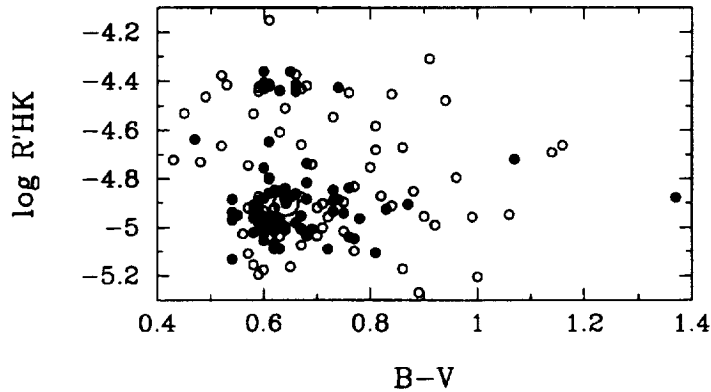


*Figure 10. The distribution in $logR'_{HK}$ (age) and $B - V$ (mass) of the 150 sun-like stars being monitored with the 0.75-m (open circles) and 0.80-m (filled circles) APTs. The position of the sun is plotted for comparison.*

Short term photometric variability ($\sigma_{short}$) in this sample of stars is shown in figure 11, where the symbols are used in the previous figure. The standard deviations are derived from the differential magnitudes computed with respect to a constant comparison star in each case. In this figure, age increases from left to right from 100 Myr to 10 Gyr. As a lower main-sequence star ages, its rotation slows, its dynamo weakens, and its chromospheric emission ratio decreases. As seen in the figure, this is accompanied by a decrease in the amplitude of short-term photometric variability. Corresponding standard deviations ($\sigma_{short}$) decrease from nearly 0.03 mag to below ~ 0.0010 mag, which represents the limit of precision for a single observation. The standard deviations from the 0.80-m APT lie systematically somewhat below those from the 0.75-m APT because longer integration times were used with the two-channel photometer on the 0.80-m APT. The day-to-day photometric variability of the sun is represented by the two circled points, based on satellite radiometer measurements and corrected for the difference between total solar irradiance and the Strömgren $b$ and $y$ band passes (Radick et al., 1998). The lower of the two represents the photometric variability of the quiet sun during sunspot minimum, while the upper symbol represents solar variability during sunspot maximum. It is clear that the APT observations will not, in general, resolve night-to-night variations in sun-like stars older than the sun.
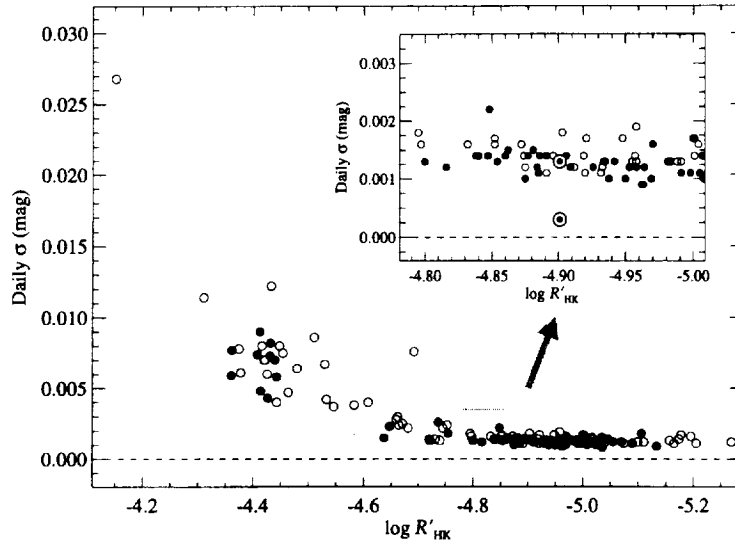
*Figure 11. Short term variability ($\sigma_{short}$) in the sample of 150 sun-like stars observed with the 0.75-m APT (open circles) and the 0.80-m APT (filled circles) as a function of chromospheric emission (age). The photometric variability of the sun during sunspot maximum and minimum is shown by the upper and lower circled points in the inset panel. Night-to-night variability less than about 0.0010 mag cannot be resolved.*

Figure 12 shows an example of long-term variability for one of the 0.75-m program-star groups. There are two program stars and two comparison stars in this particular group. Star D is $\chi^1$ Ori (HD 39587), a young ($\sim$ 800 Myr) G0 V star. Star C is 111 Tau (HD 35296), a young ($\sim$ 300 Myr) F8 V star. Stars A and B are F0 III and F0 V comparison stars, respectively. The six panels plot the six combinations of differential ($b + y$)/2 yearly mean magnitudes over five years. Error bars are the $1\sigma$ uncertainties computed as the standard deviation of a single observation from its yearly mean divided by the square root of the number of observations for the year. Dotted horizontal lines mark the mean of the yearly means. The total ranges in magnitudes of the yearly means are given in the lower-left corner of each panel; the standard deviations of the yearly means from the mean of the means ($\sigma_{long}$) are given in the lower-right corners. Comparison stars A and B exhibit good long-term stability with $\sigma_{long}$ = 0.00022 mag for the (B–A) differentials. The (D–A) and (D–B) panels clearly show a long-term 0.005-mag variation in $\chi^1$ Ori, and the (C–A) and (C–B) panels show a similar variation in 111 Tau. The (D–C) panel shows the relative brightness variation between the two variable program stars. It is clear from these observations that long term variations of 0.003–0.005 mag can be followed easily with the APTs.
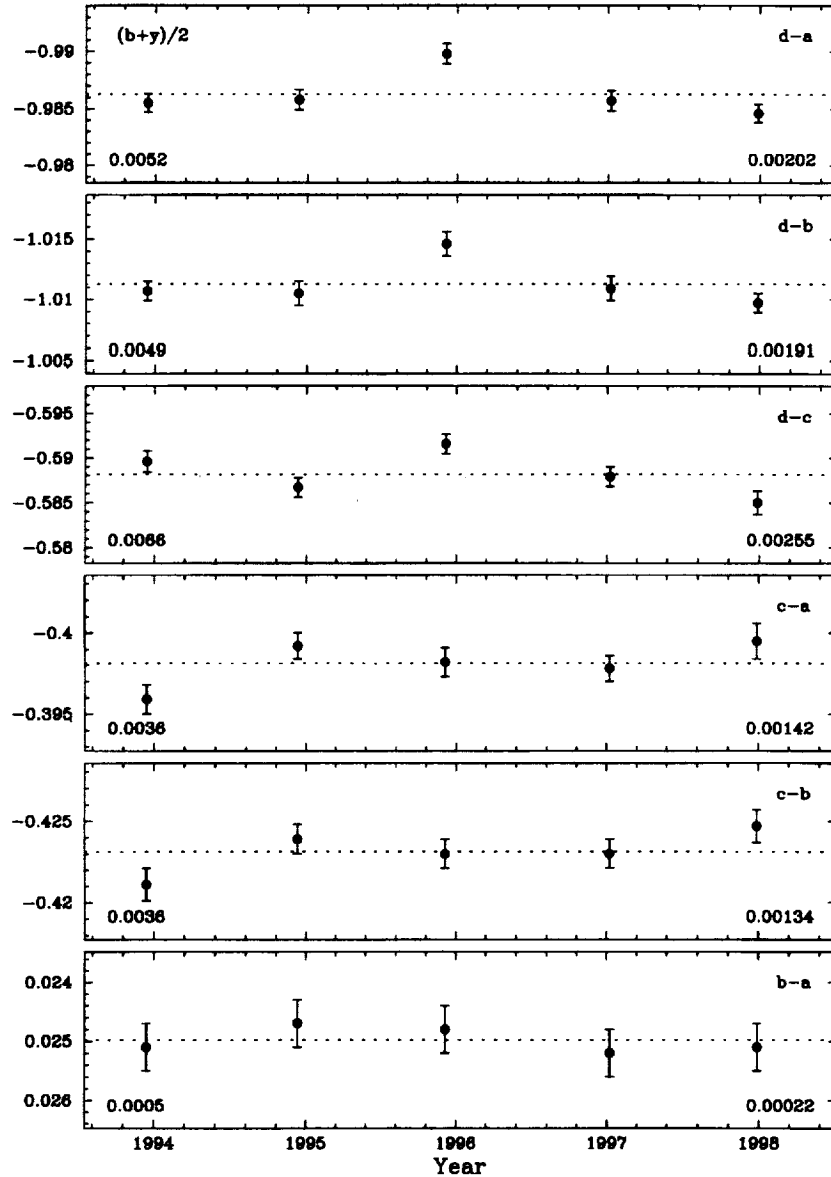
*Figure 12. Long-term variability in the young G0 V star χ¹ Ori (star D) and the young F8 V star 111 Tau (star C) as observed relative to two constant comparison stars (A and B) with the 0.75-m APT. Long-term variations of 0.003–0.005 mag can be followed easily with the APTs.*

Figure 13 shows the long-term photometric behavior of the older (~ 4 Gyr) G0 V star HD 176051 (star D) relative to three comparison stars HD 173417 (F1 III-IV, star A), HD 178538 (F0, star B), and HD 172742 (F5, star C). Stars A and B show good long-term stability with $\sigma_{long}$ = 0.00021 mag for the (B–A) differential magnitudes. HD 176051 shows clear long-term variability of about 0.0015 mag in panels (D–A) and (D–B). Comparison star C also shows obvious long-term variability of about 0.002 mag over six years in panels (C–A) and (C–B). Thus, with suitably constant comparison stars, the APTs are also capable of resolving small luminosity changes in the solar-age program stars.
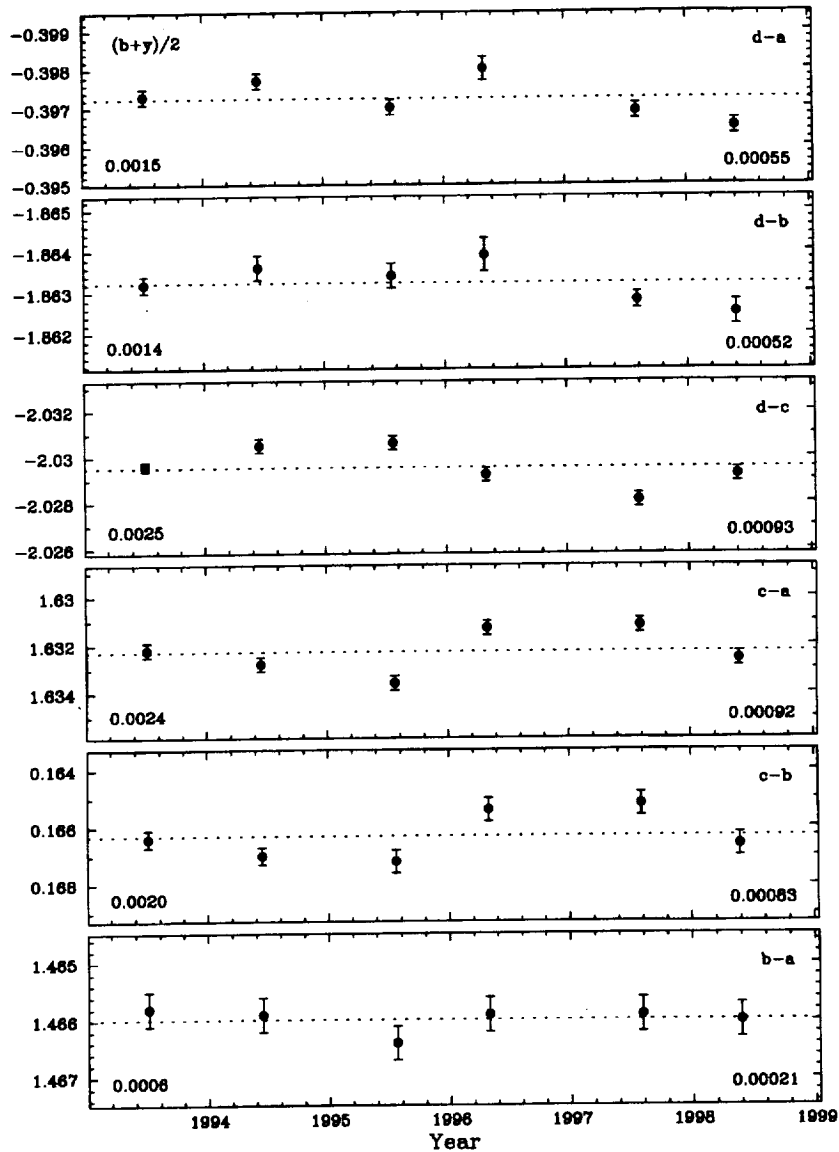
*Figure 13. Long-term variability of only 0.001 mag over several years in the solar-aged G0 V star HD 176051 (star D) is clearly resolved relative to comparison stars A and B with the 0.75-m APT. Comparison star C is also a long-term variable.*

## Search for Extrasolar Planets

Recently, several of the sun-like stars being monitored by the 0.75- and 0.80-m APTs have been discovered to have planetary-mass companions with surprisingly short periods (e.g., Marcy and Butler, 1998, and references within). Since all the new extrasolar planets have been detected indirectly via radial-velocity techniques, independent observations are needed to confirm that the observed radial-velocity variations are not due to star-spot effects or pulsations in the stars themselves. Since star spots and pulsations should both be accompanied, at some level, by light variations, the APTs can assist in the confirmation of extrasolar planetary candidates by searching for brightness variations in the stars on the reported planetary-orbital periods (Henry et al., 1997; Baliunas et al., 1997).

Figure 14 shows six seasons of nightly Strömgren $(b + y)/2$ differential magnitudes of the F7 V star $\tau$ Boo from the 0.75-m APT. The observations are plotted modulo the 3.31275-day orbital period of the $\geq 3.39M_{Jup}$ planetary companion, reported by Butler et al. (1997). Phase 0.0 corresponds to the time of conjunction when the companion would transit the star for suitable orbital inclinations. A least-squares sine fit at the orbital period yields a semi-amplitude of 0.00011 $\pm$ 0.00009 mag, indicating no light variability on the planetary period to one part in $10^4$. This supports the hypothesis that the observed radial-velocity variations in $\tau$ Boo are, indeed, due to a planetary companion. The APT photometry also supports similar conclusions for other sun-like stars with reported planetary companions (Henry et al., 1997; Baliunas et al., 1997; Henry et al., 1999).
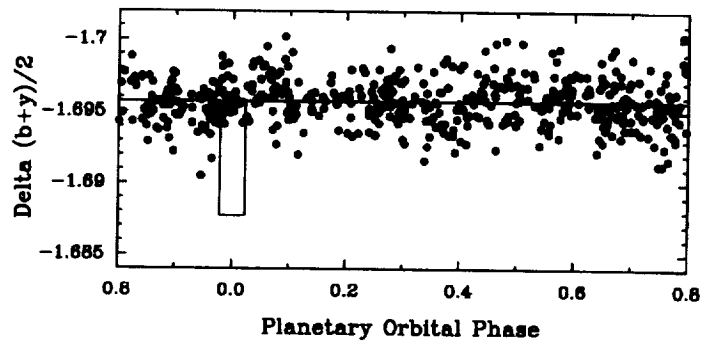


*Figure 14. Six seasons of nightly Strömgren (b + y)/2 differential magnitudes of the F7 V star $\tau$ Boo from the 0.75-m APT plotted modulo the 3.31275-day orbital period of the purported > 3.39MJup planetary companion. No light variability is observed to one part in 104, supporting the existence of the planetary companion as the cause of the observed radial-velocity variations in this star.*

Figure 15 shows the observations of $\tau$ Boo from figure 14 near the time of conjunction replotted with an expanded scale on the abscissa. An additional night of monitoring observations with the 0.80-m APT has been added. The solid line shows the predicted depth (0.008 mag) and duration (3.6 hr) of the transit for a $1.2R_{Jup}$ planet across the $1.4R\odot$ star. The detection of such a transit would resolve the inclination-angle ambiguity and allow the actual, as opposed to the minimum, mass of the planet to be computed from the radial-velocity observations. The observed depth of the transit would provide a measure of the size of the planet and, thus, its density. These parameters are important for improving theoretical models of the compositions and origins of these strange, new planets. Figure 15 shows conclusively that transits do not occur in $\tau$ Boo. Similar APT observations of six additional sun-like stars with Jupiter-mass planets in short-period orbits also reveal no transits, in spite of an overall 50% probability of finding at least one transit in the sample. With the discovery of a few additional short-period planets, the probability for the detection of a transit will increase to about 70%. The successful observation of a transit would represent the first direct detection of an extrasolar planet.
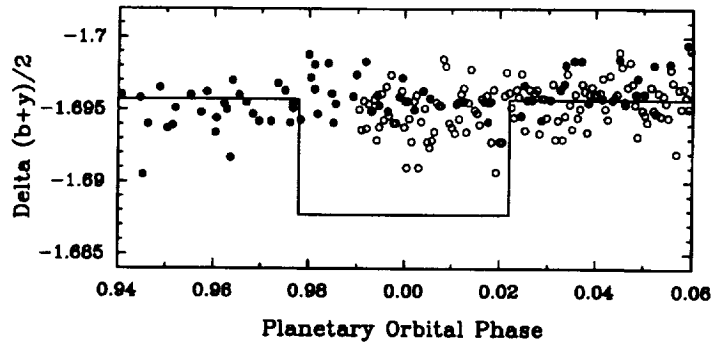
*Figure 15. Photometeric observations of τ Boo from figure 14 (closed circles) replotted with an expanded scale on the abscissa. An additional night of monitoring observations with the 0.80-m APT has been added (open circles). The solid line shows the predicted depth and duration for the transits of the planetary companion. Although the probability of transits is 14% in this system, the observations clearly show that they do not occur.*

## Acknowledgements

# References

Aerts, C.; Eyer, L.; and Kestens, E.: Astronaut & Aeronaut., vol. 337, 1998, p. 790.

Baliunas, S. L.; Donahue, R. A.; Soon, W.; and Henry, G. W.: In The 10th Cambridge Workshop on Cool Stars, Stellar Systems, and the Sun, ASP Conf. Ser. 154, R.A. Donahue and J. A. Bookbinder eds., San Francisco: ASP, 1998, p. 153.

Baliunas, S. L.; Henry, G. W.; Donahue, R. A.; Fekel, F.C.; and Soon, W. H.: Astrophys. J., vol. 474, no. L119, 1997.

Boyd, L. J., et al.: International Amateur-Professional Photoelectric Photometry Communication No. 52, 1993, p. 23.

Butler, R. P.; Marcy, G. W.; Williams, E.; Hauser, H.; and Shirts, P.: Astrophys. J., vol. 474, no. L115, 1997.

Crawford, D. L.; and Barnes, J. V.: Astrophys. J., vol. 75, 1970, p. 978.

Eaton, J. A.: In Robotic Telescopes: Current Capabilities, Present Developments, and Future Prospects for Automated Astronomy, ASP Conf. Ser. 79, G. W. Henry and J. A. Eaton, eds., San Francisco: ASP, 1995, p.226.

Edgington, W.; Drummond, M.; Bresina, J.; Henry, G. W.; and Drascher, E.: In New Observing Modes for the Next Century, ASP Conf. Ser. 87, T. Boroson, J. Davies, and I. Robson, eds., San Francisco, ASP, 1996, p. 151.

Hardie, R. H.: In Astronomical Techniques, W. A. Hiltner, ed., Chicago: University of Chicago Press, 1962, p. 178.

Hatzes, A. P.; and Cochran, W. D.: in The 10th Cambridge Workshop on Cool Stars, Stellar Systems, and the Sun, ASP Conf. Ser. 154, R. A. Donahue and J. A. Bookbinder, eds., San Francisco: ASP, 1998, p. 311.

Henry, G. W.: In New Observing Modes for the Next Century, ASP Conf. Ser. 87, T. Boroson, J. Davies, and I. Robson, eds., San Francisco, ASP, 1996, p. 145.

Henry, G. W.; Baliunas, S. L.; and Donahue, R. A.: Astrophys. J., 1999, in preparation.

Henry, G. W.; Baliunas, S. L.; and Donahue, R. A.; Soon, W. H.; and Saar, S. H.: Astrophys. J., vol. 474, 1997, p. 503.

Henry, G. W.; Fekel, F. C.; Henry, S. M.; and Hall, D. S.: Astrophys J., 1999, in preparation.

Lockwood, G. W.; Skiff, B. A.; and Radick, R. R.: Astrophys, J., vol. 485, 1997, p. 789.

Marcy, G. W.; and Butler, P. B.: In The 10th Cambridge Workshop on Cool Stars, Stellar Systems, and the Sun, ASP Conf. Ser. 154, R. A. Donahue and J. A. Bookbinder, eds., San Francisco: ASP, 1998, p.9.

Perryman, M. A. C., et al.: The Hipparcos and Tycho Catalogues (ESA: The Netherlands), 1997.

Radick, R. R.; Lockwood, G. W.; Skiff, B. A.; and Baliunas, S. L.: Astrophys. J., vol. 118, 1998, p. 239.

Soon, W. H.; Posmentier, E. S.; and Baliunas, S. L.: Astrophys. J., vol. 472, 1996, p. 891.

# Semiautomated Precise Photometry

Edward W. Dunham
*Lowell Observatory, 1400 Mars Hill Road,
Flagstaff, AZ 86001*

## Abstract

Application of the transit photometry method for detecting extrasolar giant inner planets requires acquisition of a large amount of photometric data on each of several thousand stars over a period of many weeks. The observational workload is very high if these data are obtained manually, so we have made a semiautomated system to carry out the observations at Lowell's Mars Hill location. This is a compromise between the observational effort of a manual system and the complexity of a robotic system.

The equipment currently in use consists of a Loral 2Kx2K charged coupled device (CCD) mounted at the focal plane of an Aero-Ektar $f/2.5$ aerial camera lens with 30.5-centimeter (cm) focal length. The CCD camera system is the modified SNAPSHOT camera system (Dunham, et al., 1985; Dunham, 1995). It is set up to take a large number of exposures unattended during the night. The camera and dewar are mounted on a Celestron Computstar 14 telescope mount and autoguided with an SBIG ST4 autoguider attached to a Celestron C90 guide telescope.

The current system needs to be set up manually each night and stowed each morning. In addition, if the weather deteriorates during the night, the equipment must be manually stowed for protection. A proposed upgrade to the current hardware will allow these functions to be handled remotely. This in turn will allow the system to operate efficiently at Lowell's darker but more remote Anderson Mesa site.

## Introduction

The recent discovery of giant planets orbiting other stars in orbits with very small semimajor axes has dramatically increased the a priori probability of detecting transits by extrasolar planets. This development has prompted investigators at Lowell Observatory, the High Altitude Observatory, and the NASA Ames Research Center to begin work on photometric searches for transits by extrasolar giant inner planets. This paper describes the instrumentation and observational processes used in the search that is beginning at Lowell Observatory.

The photometric problem is defined by two main factors: 1) the probability that a given field star possesses a giant inner planet with suitable orbital inclination and period; and 2) the photometric signature of the transit by the planet.

Within the 120-star sample searched by Butler and Marcy, approximately 3% have giant inner planets (Butler, et al., 1997). The probability that an extrasolar planet will transit its parent star is $R_*/R_{orbit}$. For the giant inner planets already known, this is approximately 10%. Thus the odds that a star in the Butler and Marcy sample will show transits is ~1:300. The overall probability that a field star will show transits is not as clearly defined because of the selection criteria that were applied in deriving the Butler and Marcy sample. They included stars with surface temperatures similar to the sun's and low rotational velocities, and excluded known spectroscopic binaries. If we assume that close binaries account for half of all stars (Allen, 1976), and that half of the stars in a given field

at 10th-12th magnitude are F-K main sequence stars (Allen, 1976), we conclude that the fraction of stars in a given field that are F-K dwarfs showing transits by giant inner planets will be ~1:1200.

Figure 1, provided by T. Brown, shows the fraction of transits detected as a function of orbital period for a six-week observing run. It shows the case for both a single site and a network of three sites all located in the western U.S. The weather is assumed to be good enough for differential photometry 35% of the time at each site, and is further assumed to be uncorrelated among sites. Observations are assumed to be taken for seven hours per night. The top pair of curves is for detection of two transits, the middle pair for three transits, and the bottom one for four detected transits. The solid curves are the detection rates for three sites and the dashed curves are for a single site. With three sites, the fraction of stars with two or three detected transits is approximately 75% or 40% respectively, depending on the distribution of sites. This figure, together with the odds that field stars will show transits, indicates that we will need to observe approximately 1600 or 3000 stars for every star showing two or three detected transits in a six-week coordinated observing run at three sites.
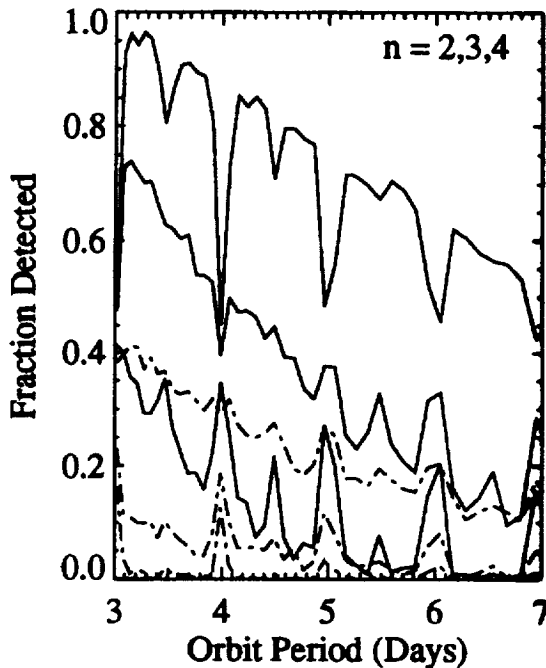


Figure 1. The predicted fraction of stars exhibiting transits that are actually detected in a six-week observing run at either one (dashed line) or three (solid line) sites located in the western U.S., accounting for weather and the diurnal cycle. The top pair of curves shows the fraction of transiting systems for which two transits are detected. The middle pair reflects the fraction with three detected transits, and the bottom pair shows the fraction with four detected transits.

The giant inner planet models of Guillot, et al. (1996) indicate that the radii of these objects depend only weakly on their mass in the range of 0.5–3 Jupiter masses. Radii range from approximately 0.5 Jupiter radii to about 1.2 Jupiter radii, depending on composition. Thus we expect a transit depth on the order of 1/4% to 1.4% depending on planetary composition and stellar size. The duration of a transit is approximately 2.5–3 hours for objects with periods of ~4 days and orbital

48

radii of ~0.05 astronomical unit (AU). Therefore, to detect a transit reliably, we need to achieve a differential signal/noise (S/N) ratio of 0.1% to 0.5% in an integration time of ~30 minutes.

In summary, the photometric problem to be solved requires millimagnitude differential photometry of several thousand stars in a crowded field. It turns out that star densities are such that the aperture of the telescope used for the photometric search is not very important, but the focal ratio is very important. For a given $f$/ratio and detector, a larger telescope can achieve a good S/N ratio on fainter stars, but the field area is smaller, so the number of target stars remains approximately the same. We have elected to pursue the small telescope, wide-field option because follow-up radial velocity observations will be more successful with brighter stars, and because the equipment is less expensive.

## Instrumentation

The instrumentation in current use for the Lowell extrasolar planet search project is largely borrowed because the project is not funded. The detector system is the modified SNAPSHOT CCD camera described by Dunham (1995) and Dunham, et al. (1985). This system incorporates a front-illuminated Loral 2Kx2K CCD. The "telescope" is an $f$/2.5 Aero-Ektar aerial camera lens with 12-inch focal length that was in storage at Lowell. The complete system provides a plate scale of 10.0 arcseconds (arcsec)/pixel and a field of view of 5.7 degrees. The camera lens and CCD dewar are mounted on a Celestron Compustar 14 telescope mount. A Celestron C90 guide telescope is used with an SBIG ST-4 CCD autoguider to provide guiding for the system. The entire assembly, shown in figure 2, is mounted in a small roll-off roof building at Lowell's Mars Hill site not far from the astrograph used by Clyde Tombaugh to discover Pluto.



*Figure 2. The equipment used for the Lowell search for extrasolar giant inner planets. The Aero-Ektar lens is in the gray cylindrical housing. The CCD dewar is normally mounted on the rectangular part of the lens housing, but is not mounted in this image. The filter wheel is located inside the lens assembly. The built-in shutter in the lens is used as the system shutter.*

The filter used for observations to date, which we call the VR filter, is essentially a combination of the V and R passbands (Bessell, 1976, and Bessell, 1990). It consists of 2 millimeters (mm) of Schott GG-495, normally used to provide the blue cutoff for a V filter, and 2 mm of Schott KG-3, normally used to provide the red cutoff for an R filter. This filter was selected in order to maximize the bandpass within the image quality constraints imposed by the chromatic aberration of the lens. The chromatic behavior of the lens was found by finding the focus blur as a function of wavelength. Image full width at half maximum (FWHM) values were found to be 7, 3.4, 2.5, and 9 pixels in the B, V, R, and I passbands, respectively. Neither a calculation nor an observational check has been carried out to see if the VR filter provides the best S/N ratio compared to, say, V or R.

The flat-field screen consists of an aluminum plate painted flat white. This plate is illuminated by the twilight sky to minimize gradients over the wide field of the system, following the suggestion of Chromey and Hasselbacher (1996).

It was found during the first full-moon observing cycle that scattered moonlight from the lens was the major contributor to the sky brightness. As a result, a moon shade was made that did not vignette the field of view, but succeeded in keeping moonlight from falling directly on the lens. This shade reduced the sky background by about a factor of three.

The SNAPSHOT control program is written in C language and runs under UNIX. It is command-line driven, with input coming from the standard input. As a result, it is trivial to run the program with its input redirected from a text file. A few modifications to the program were made to facilitate this mode of operation, and it can run unattended for an entire night under reasonably good weather conditions. The system is capable of operating in the presence of thin cirrus cloud cover, but cannot cope if the weather deteriorates substantially. Occasional crashes of the control software cause loss of data for the rest of the night because the system operates unattended after it is set up.

**Observing Procedure**

The activity for a typical observing night begins with acquisition of bias, dark, and flat-field frames. A SNAPSHOT control script was written to take dark and bias frames, and another script for flat-field frames was also written. In principle, these could have been combined, but manual intervention is currently needed to ensure that light leaks in the camera do not corrupt the dark frames. The flat-field script was "tuned" so that good signal levels are obtained as twilight progresses. All that needs to be done is for the script to be started at a particular solar depression angle.

When the calibrations are complete, the telescope is pointed at the target field and the liquid nitrogen dewar is filled to capacity. Then the field is acquired and the autoguider is "trained" and autoguiding begins. Finally, a test frame is taken to ensure that the system is operating correctly and the SNAPSHOT program is restarted using the night's observing script. The system is then left until the next morning. A microswitch turns off the telescope drive when the hour angle reaches a predetermined value. In the morning, the telescope is stowed, the dewar is topped off, and a tape backup of the previous night's data is generated.

The ST-4 autoguider has an annoying cutoff on the guide star brightness. If the brightness of the peak pixel of the guide star drops below half of the value it had when the ST-4 was set up, it will automatically stop trying to track. If it gives up tracking long enough for the guide star to leave its small field of view, it will fail to regain track and the remainder of the night's work will be lost. This problem can occur if cirrus clouds pass through during an otherwise good night. Also, the C90 guide

telescope focus drifts somewhat as a function of zenith distance, causing the peak pixel brightness to change.

We circumvent loss of track in two ways. First, we cover half the aperture of the C90 during setup so that it is "fooled" into "thinking" that it is tracking on a fainter star. This works very well; evidently the ST-4 has no cutoff if the guide star becomes too bright! Second, we calibrated the C90 focus as a function of hour angle for a given field and offset it so that the focus is set in the middle of the focus variation range.

The amount of manual intervention required is marginally acceptable because the instrumentation is located near the Lowell offices on Mars Hill. If the equipment is moved to a darker, more remote site, additional automation and remote operation capability will be needed for efficient operation.

## Performance

**Image Quality.** The system as described provides star images in the VR filter with 2.5 pixels or 25 arcsec FWHM. The image profile has a sharp core with rather extended wings. This is probably chromatic in nature since these lenses were designed to be used over a more restricted bandpass using photographic materials.

**Tracking Performance.** The autoguider works quite well, but the C90 guide telescope has internal flexibility that causes tracking errors to occur, as well as the focus drift already mentioned. The tracking errors are mainly in the east-west, or column, direction, as seen in figure 3. No attempt was made to correct for these drifts during a night, and so far no analysis results are available to determine how important the drifts are from a photometric point of view.

**Duty Cycle.** The SNAPSHOT system can read out and store an unbinned 2Kx2K CCD frame in 94 seconds, so the standard 240-sec (4-minute) exposures were obtained at a rate of nearly 11 frames per hour. The observing efficiency was 72% for this exposure time.

**Polar Alignment.** A very effective method of polar alignment is to point the camera system toward the north celestial pole and take a series of exposures with the telescope tracking on. The star positions move between exposures at a rate that is proportional to the time between exposures and the angular offset of the telescope RA axis from the refracted pole. The position angle of the apparent motion vector is related to the position angle of the offset of the telescope axis from the refracted pole.

This method was unfortunately not possible to use for the Lowell system because the building blocked access to the polar region. Instead, we used a scheme making use of the Compustar pointing system. We set on a star and updated the telescope mount coordinates. The telescope was then swung through a few hours of RA to another star with nearly the same dec, and the difference in dec between the actual position of the star and the telescope dec readout was used to derive the offset of the telescope RA axis from the pole. After adjusting the telescope mount, the process was repeated, and iteration continued until the offset was about 3 arcminutes, which is about the limiting accuracy for the hardware used. This will result in field rotation on the order of ±3 arcminutes over a night. The corresponding image motion of a star image near the edge of the CCD, if the guide star is near the center of the CCD, should be about ±1 pixel.

51

**Autoguiding Performance**
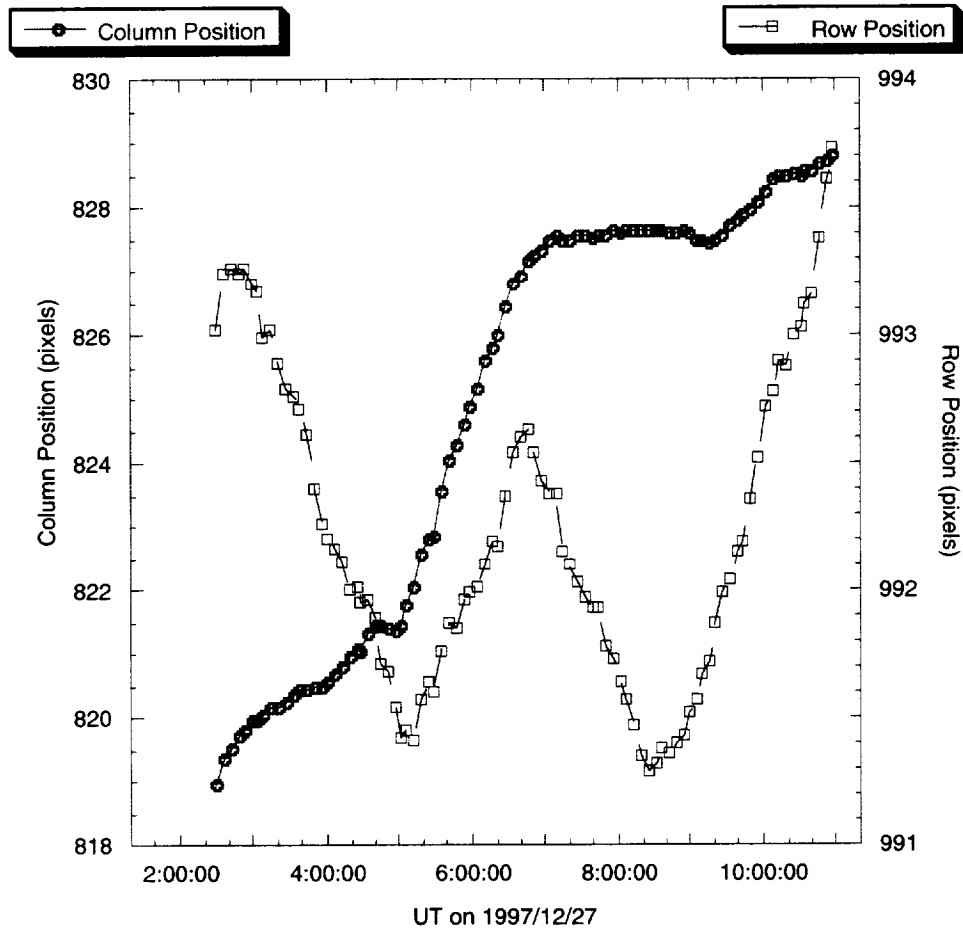


*Figure 3. The autoguider tracking performance. The column coordinate corresponds to right ascension (RA) and the row coordinate to declination (dec). The guide star, λ Aur, passed the meridian at 7:06 universal time (UT).*

**Theoretical Photometric Performance.** The data from the 1997–1998 observing season have not been analyzed yet, so photometric performance can be discussed on only a theoretical basis. It is important to recognize that the photometric problem is purely differential, not requiring transformation to standard photometric systems or all-sky photometry.

Five sources of noise are significant for wide-field differential photometry: shot noise on the target stars, shot noise on the sky background, scintillation noise, differential extinction from thin cirrus clouds, and noise introduced by motion of the target stars across the CCD. CCD read noise and dark current are negligible contributors. The contributions from the first three noise sources in a 30-minute period (factoring in the duty cycle of the current system) are shown as a function of stellar magnitude for moonless conditions in figure 4. The shot noise values are based on measured signals from data obtained in January 1998. Following Young (1974; also Dravins, et al., 1998), we find

that the fractional noise due to scintillation for our 12-centimeter (cm) camera aperture is about 0.0007 in a 30-minute integration at two airmasses, accounting for our present duty cycle. Note that the dominant noise source for most stars is shot noise on the 19.8-magnitude-per-square-arcsecond sky background at Mars Hill in the "VR" filter.

We found during observations in November 1997 through January 1998 that many nights suffered from thin cirrus clouds. With a wide field of view, noticeable transparency variations across the field occur. This problem can be mitigated, if not eliminated, by using only nearby stars as comparison stars for a given star. This will reduce the number of comparison stars from thousands to tens, but should substantially decrease the cirrus-induced noise, allowing operation during nights that would otherwise be lost.

Potentially the most serious noise source is motion of the star images across the CCD. We have carried out laboratory tests at NASA Ames dealing with this issue (Robinson, et al., 1995, and Jenkins, et al., 1997). These tests indicated that if the star images are somewhat defocused, they are kept within a pixel of the same location, and the apparent brightness change with position and focus is measured, fit, and subtracted from the raw brightness, the fractional stability of differential photometry with commercial CCDs is better than $10^{-5}$. Common experience with CCD photometry in which star images are not kept in the same place is that precision substantially better than 0.5% is very difficult to achieve. The autoguider performance shown in figure 3 thus may be troublesome. Image motion due to differential refraction is less than a pixel above two airmasses and, as noted earlier, polar alignment can be sufficiently accurate that field rotation can be reduced to this level as well.

## Proposed Improvements

We have proposed to make many improvements to the system described here. The overall goal of the upgrades is to improve the data quality and reduce the manual intervention required to obtain the data. The major improvements include:

- Move the operation from Mars Hill to Lowell's dark Anderson Mesa site to reduce the shot noise on the sky.

- Reduce the flexure in the guiding system so guiding is good to about a pixel to reduce the noise induced by image motion.

- Incorporate new CCD control hardware and software to improve the observational duty cycle and improve the ability of the system to work remotely and autonomously.

- Modify the telescope control and autoguider systems to allow remote operation with reduced manual intervention.

- Modify the CCD dewar to use a cryocooler instead of liquid nitrogen to maintain low-temperature operation while eliminating manual nitrogen fills.
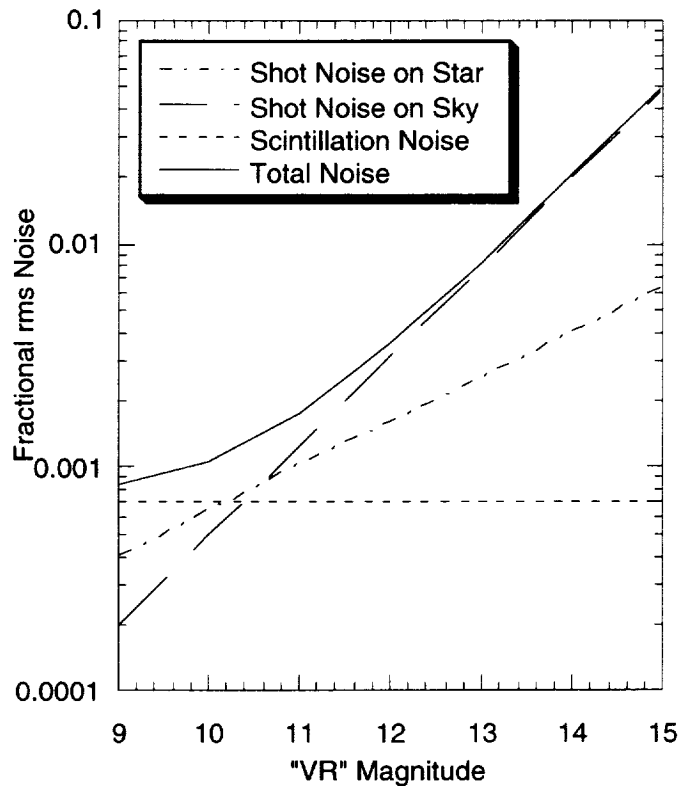
*Figure 4. The predicted differential S/N ratio for stars of various brightnesses. The contributors considered are shot noise on the star, shot noise on the sky, and scintillation noise. The solid line shows the Root Sum of Squares (RSS) total noise from these sources. See text for details and for discussion of additional noise sources.*

## An Optimized Optical System?

During the workshop we discussed the advantages of an optical system with an optimally blurred point-spread function (PSF) with minimal sharp edges or sharp features in it. I examined a folded field-flattened Schmidt design. The folding secondary mirror is nominally flat, but if it is intentionally bent slightly, it introduces astigmatism. Although the resulting PSF is not optimal, it is far superior to the PSF of the Aero-Ektar lenses, and is worth consideration. The additional complication of an achromatic Schmidt provides better image quality, but may not be justified for this application.

The basic optical system is a 10-inch $f$1.5 Schmidt, and is shown in figures 5a and 5b. Its corrector plate has a spherical curve, so reflections off the detector and back from the corrector plate are grossly out of focus by the time they reach the focal plane again. For manufacturing convenience, the radius of the convex spherical side is the same as the radius of the primary mirror. The primary mirror is an $f$1.5 sphere, and the secondary is a stock flat mirror. A 4-mm-thick filter is the next optical element, followed by a two-element field flattener. The leading element is thick enough to serve as a dewar window. When used with a 2Kx2K CCD with 15 micron pixels, the image scale is 8.12 "/px and its square field of view is 4.6 degrees on a side. All transmissive optics can be optimized using either silica or BK7 with almost identical image quality.

The most likely mechanical configuration for this system would be to build the CCD camera mount into the primary mirror mount and attach the filter and shutter mechanism to the front of the CCD dewar. The secondary mirror could be supported from the dewar as well, but would more likely be supported from a "tub" attached to the primary mirror mount.
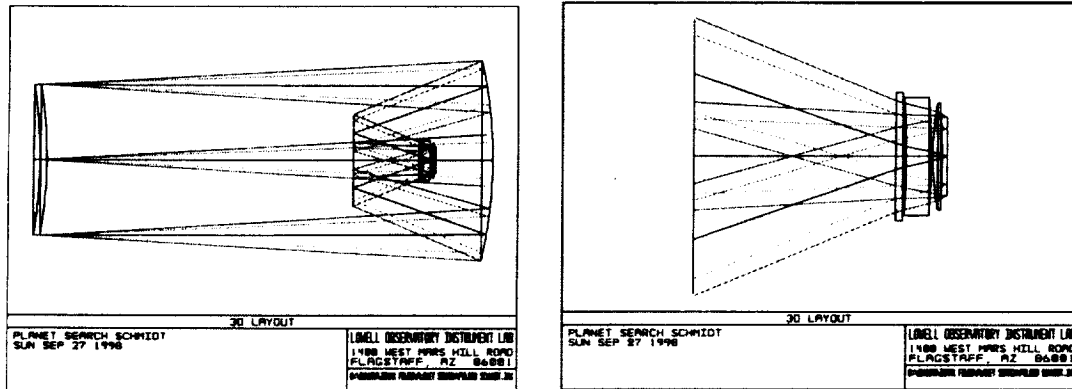


*Figure 5a (left). Diagram of the folded Schmidt system. Figure 5b (right) Detailed view of the section from the secondary mirror to the focal plane.*

The optical design optimization was done for a spectral range running from 0.4 to 0.85 microns. The performance of the system would be improved if the wavelength range were reduced by use of a filter.

The optical performance of the system is shown in the spot diagrams (figures 6a and 6b) and enclosed light curves (figures 7a and 7b). In these figures, the left frame is for the system without additional astigmatism and the right figure has the flat secondary mirror bent to a radius of 350 meters corresponding to a sag of about 8 microns at the edges of the mirror relative to its center. This amount of astigmatism is shown as an example, and a wide choice for this amount is available. The PSF is not as smooth as one would like, but on a gross scale it is relatively flat. If this PSF is convolved with seeing blur, much of the small-scale structure will be smoothed out.

Compared to the Aero-Ektar lenses we are currently using, the Schmidt system has 2.8 times the collecting area and 0.64 times the solid angle coverage on the sky. The sky brightness per pixel would be 80% higher, so the faintest star detectable at a given S/N ratio would be fainter by about a factor of two. We would, therefore, be able to observe about twice as many stars per square degree, or 30% more, accounting for the smaller field, than with the Aero-Ektars. If the throughput of the Aero-Ektars is low, the throughput advantage would be correspondingly larger for the Schmidt system.

The PSF of the Schmidt system is far better behaved than the Aero-Ektar PSF. The wings are fully enclosed in a diameter of 3–4 pixels, depending on whether additional astigmatism is included in the optical system, and the "peakiness" of the PSF is reduced. Tim Brown's recent discovery that the Aero-Ektar PSF extends out to 500 microns radius suggests that a better optical arrangement will be mandatory, and that the gain to be had by going to a Schmidt system will be far greater than indicated above.
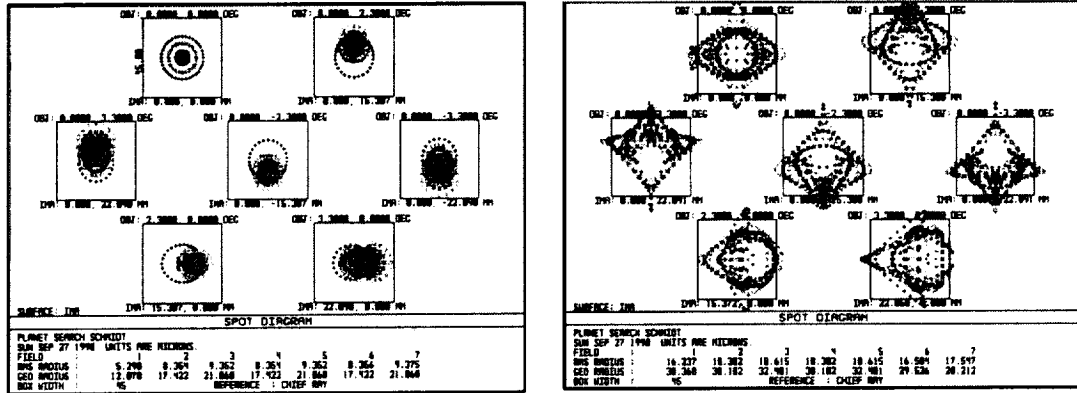
*Figure 6a (left). The spot diagrams of the folded Schmidt system for fields corresponding to the center, edge, and corner of a 2K x 2K CCD with 15 micron pixels. The upper-left spot diagram is for the field center, the upper right is for the edge in the +y direction, and the center left is for a "corner" in the same direction as the edge but 1.4 times farther from the field center. The next two spot diagrams are for the same two off-axis fields but in the opposite direction, so they are upside down. The two fields in the bottom row are for the edge and corner, but in the +x direction. In this figure, the secondary mirror is flat and does not introduce astigmatism. Figure 6b (right) is the same thing but with the secondary bent to a radius of 350 meters in one direction. The central obscuration is showing up in these images. The boxes are 45 microns, or 3 pixels, on a side.*

*Figure 7a (left). The enclosed energy diagram of the folded Schmidt system with no additional astigmatism introduced. The 80% enclosed energy radius is 8 microns. Figure 7b (right) is the same thing but with the secondary bent to a radius of 350 meters in one direction. The 80% enclosed energy radius is 18 microns.*

A more complex design with an achromatic corrector plate is also possible at substantial additional cost. In this design the corrector plate is a cemented doublet with aspheric curves on the outer faces of the two elements. The crown element of the corrector is made of BK7 and the flint is LLF6. This design gives superior image quality and would be a better arrangement for a 4K x 4K CCD with 9 micron pixels. The image quality measured in pixels (9-micron rather than 15-micron pixels) is somewhat better than in the previous design, and the sky brightness per PSF area is smaller by approximately a factor of four; confusion would also be reduced. Thus with this design, the magnitude limit would be reduced by nearly another magnitude. The spot diagrams and enclosed

56

energy curves are given in Figures 8 and 9 below. Because of the improved image quality, the astigmatic radius introduced in the secondary is 700 meters instead of 350 meters.
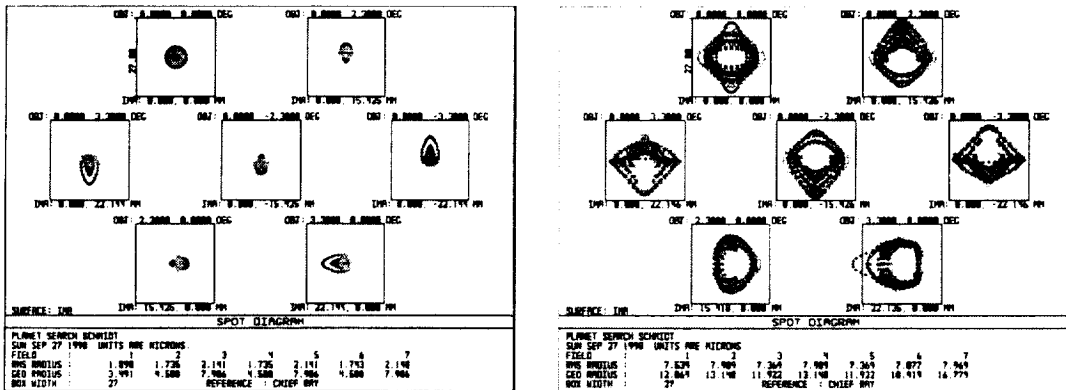


*Figure 8a (left). The spot diagrams of the achromatic Schmidt system, analogous to Figure 6a. In this figure, the secondary mirror is flat and does not introduce astigmatism. Figure 8b (right) is the same thing but with the secondary bent to a radius of 700 meters in one direction. The central obscuration is showing up in these images. The boxes are 27 microns, or 3 pixels, on a side.*
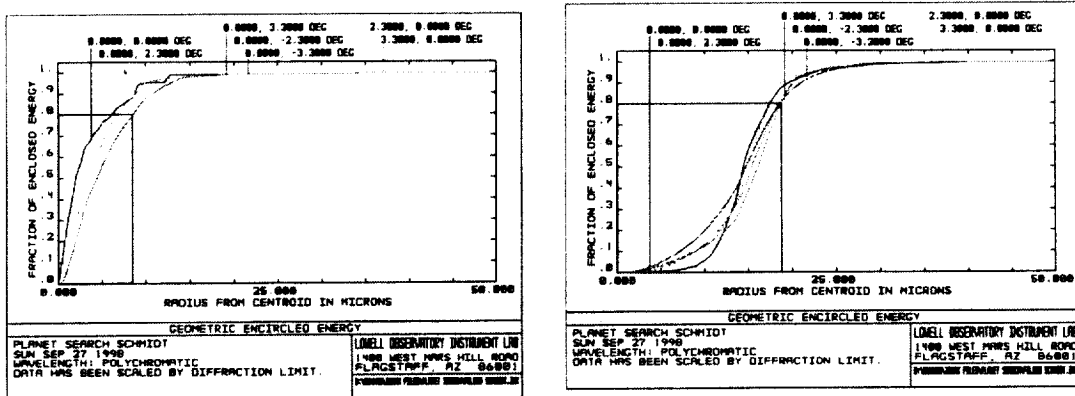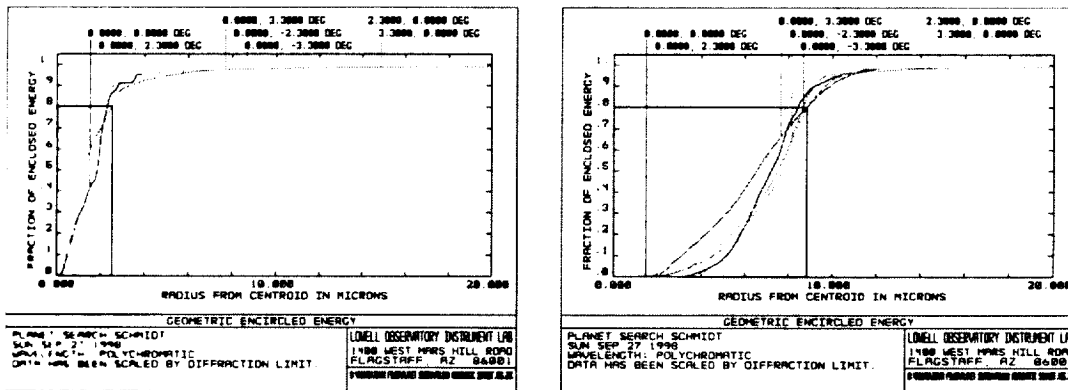


*Figure 9a (left). The enclosed energy diagram of the achromatic Schmidt system with no additional astigmatism introduced. The 80% enclosed energy radius is 2.5 microns. Figure 9b (right) is the same thing but with the secondary bent to a radius of 700 meters in one direction. The 80% enclosed energy radius is 9 microns.*

It is interesting to see if a commercial Schmidt–Cassegrain Telescope (SCT) could be modified to become a good wide-field system. I found what appears to be the prescription for an 8-inch SCT in the ZEBASE design database (lens N-069). I scaled this up to be a 14-inch SCT, moved the corrector to the center of curvature of the primary, replaced the secondary with a flat, and added a two-element field flattening lens. The result is shown in figure 10.

Figure 10. Modified SCT. The top row includes a list of design parameters and a layout drawing. Below these are spot diagrams for each field at different focus positions and an enclosed energy diagram. The bottom left figure shows the "footprint" of the beams from the various fields on the secondary mirror to illustrate the vignetting of the system. The bottom right shows the longitudinal chromatic aberration.

The idea of using a commercial SCT is worth consideration, even though it is substantially inferior to a custom design, because the PSF is much better behaved than the Aero-Ektar. The main problems in the design are significant spherical aberration, serious vignetting (about 40% throughput), and an f/2.8 focal ratio. The vignetting and slower f/ratio together imply that this system would actually detect about half as many stars as the Aero-Ektar, neglecting its poor PSF and

possible poor throughput. In practice, the situation would not be so bad, but experimentation would be required to see how well it would do.

The initial price estimate I got for a Schmidt system was high enough that I looked at a purely refractive alternative, shown in Figure 11. This system has the same focal length as our current Aero-Ektars, but is $f/1.9$ instead of $f/2.5$. This works out to have about the same performance as the $f/1.5$ Schmidt because it is slower, but unobscured. The image quality is also nearly the same. It makes heavy use of FK51, a glass with nice optical qualities but one that is susceptible to thermal shock and breakage. In many respects it is like calcium fluoride, but not quite as volatile. We flew a 6-inch-diameter, 1-inch thick calcium fluoride window on the KAO and the Learjet and it didn't break. The last element in the lens is effectively a field flattener and could double as a dewar window. There is no filter in the design, but the most likely place for it to go is in the gap forward of the last two elements.

Price estimates have been made, but it is still not clear which approach would be best. Our options seem to be: 1) make one of the new optical systems; 2) try to make a new design that is much less expensive but still "good enough," an option that would require more funding; 3) try a modified commercial SCT; 4) use the Aero-Ektars; or 5) try to find a commercial lens that is affordable and adequate.

## Acknowledgements

Figure 11. Custom Lens Option. At top left is a list of design parameters. Next to it is a layout drawing. Below these are spot diagrams for each field at different focus positions and an enclosed energy diagram. The bottom left figure shows the field curvature and distortion for each wavelength. The bottom right shows the longitudinal chromatic aberration. This system is unvignetted.

60

## References

Allen, C.W.: Astrophysical Quantities (Third Edition). The Athlone Press, London, 1976.

Bessell, M.S.: UBVRI Photometry with a Ga-As Photomultiplier. *Publ. Astron. Soc. Pacific*, vol. 88, 1976, pp. 557–560.

Bessell, M.S.: UBVRI Passbands. *Publ. Astron. Soc. Pacific* vol. 102, 1990, pp. 1181–1199.

Butler, R.P.; Marcy, G.W.; Williams, E.; Hauser, H.; and Shirts P.: Three New "51 Pegasi-Type" Planets. *Astrophys. J.* vol. 474, 1997, pp. L115–L118.

Chromey, F. R.; and Hasselbacher, D. A.: The Flat Sky: Calibration and Background Uniformity in Wide-Field Astronomical Images. *Publ. Astron. Soc. Pacific*, vol. 108, 1996, pp. 944–949.

Dravins, D.; Lindegren, L.; Mezey, E.; and Young A.T.: Atmospheric Intensity Scintillation of Stars. III. Effects for Different Telescope Apertures. *Publ. Astron. Soc. Pacific*, vol. 110, 1998, pp. 610–633.

Dunham, E. W.; Baron, R. L.; Elliot, J. L.; Vallerga, J. V.; Doty, J. P.; and Ricker G. R.: A High-Speed, Dual-CCD Imaging Photometer. *Publ. Astron. Soc. Pacific*, vol. 97, 1985, pp. 1196–1204.

Dunham, E.W.: Optical Instrumentation for Airborne Astronomy. In "Airborne Astronomy Symposium on the Galactic Ecosystem," M.R. Haas, J.A. Davidson, and E.F. Erickson, eds., *ASP Conference Series*, vol. 73, 1995, pp. 517–522.

Guillot, T.; Burrows, A.; Hubbard, W.B.; Lunine, J.I.; and Saumon D.: Giant Planets at Small Orbital Distances. *Astrophys. J.*, vol. 459, 1996, pp. L35–L38.

Jenkins, J.M.; Borucki, W.J.; Dunham, E.W.; and McDonald, J.S.: High Precision Photometry with Back-Illuminated CCDs. In "Planets Beyond our Solar System and Next-Generation Space Missions," D. Soderblom, ed., *ASP Conference Series*, vol. 119, 1997, pp. 277–280.

Robinson, L.B.; Wei, M.Z.; Borucki, W.J.; Dunham, E.W.; Ford, C.H.; and Granados A.F.: Test of CCD Precision Limits for Differential Photometry. *Publ. Astron. Soc. Pacific*, vol. 107, 1995, pp. 1094–1098.

Young, A.T.: In Methods of Experimental Physics, vol. 12, Astrophysics, part A Optical and Infrared, 1974.

# A Performance Comparison for Two Versions of theVulcan Photometer

W. J. Borucki, D. A. Caldwell, and D. G. Koch
*NASA Ames Research Center, Moffett Field, CA 94035-1000*

J. M. Jenkins
*SETI Institute*
*2035 Landings Road, Mountain View, CA 94043*

R. L. Showen
Raytheon Systems Co., Moffett Field, CA 94035-1000

## Abstract

Analysis of the images produced by the first version (V1) of the Vulcan photometer indicated that two major sources of noise were sky brightness and image motion. To reduce the effect of the sky brightness, a second version (V2) with a longer focal length and a larger format detector was developed and tested. The first version consisted of 15-centimeter (cm) focal length, F/1.5 Aerojet Delft reconnaissance lens, and a 2048 x 2048 format front-illuminated charged coupled device (CCD) with 9 μ micropixels (Mpixels). The second version used a 30-cm focal length, F/2.5 Kodak AeroEktar lens, and a 4096 x 4096 format CCD with 9 μpixels. Both have a 49-square-degree field of view (FOV), but the area of the sky subtended by each pixel in the V2 version is one-fourth that of the V1 version. This modification substantially reduces the shot noise due to the sky background and allows fainter stars to be monitored for planetary transits. To remove the data gap and consequent signal-level change caused by flipping the photometer around the declination axis and to reduce image movement on the detector, several other modifications were incorporated. These include modifying the mount and stiffening the photometer and autoguider structures to reduce flexure. This paper compares the performance characteristics of each photometer and discusses tests to identify sources of systematic noise.

## Introduction

A knowledge of other planetary systems, including information on the number, size, mass, and spacing of the planets around a variety of star types, should enable us to deepen our understanding of planetary-system formation and processes that give rise to their final configurations. Recent discoveries (Mayor and Queloz, 1995; Cochran et al., 1997; Butler et al., 1997) show that many planetary systems are quite different from the solar system in that they possess giant planets in short-period orbits. To obtain information on the statistical properties of the giant inner planets and to develop the statistical dependencies of these, it is necessary to observe many of these objects for a variety of stellar spectral types and stellar compositions and at a range of semi-major axes.

The current method of discovering giant planets uses Doppler velocity observations that require a measurement precision near one part per hundred million. Obtaining this level of precision requires a large-aperture telescope to collect enough photons to reduce the shot noise to a level low enough that the extremely small spectral displacements can be discerned. In the future it may be possible to use transit photometry to obtain statistical information on inner planets and to identify targets for Doppler velocity determinations of the mass. The use of small photometric telescopes would be a much less expensive method of finding planets and determining the planet size and orbital period. To test this approach, we have constructed two small telescopes and tested them at the Lick Observatory on Mt. Hamilton. This paper describes the results of the first six months of our tests.

# Needed Precision

Planets the size of Jupiter and Saturn produce a 1% reduction in the brightness of a G2 main sequence dwarf like our sun. For stars as large as spectral class F0, a jovian-sized planet would produce a flux reduction of 0.45%, whereas it would produce a 3% to 14% reduction for stars of spectral class M0 to M5. (See table 1.) For planets like 51Peg B that are at 0.05 astronomical unit (AU) of their star, the signals could be 50% larger (Guillot et al., 1996) than shown in table 1. Signals with amplitudes of 1% or greater can be detected with ground-based photometry when special care is taken to minimize the various errors introduced by the atmosphere and the instrumentation. Three or more transits that demonstrate a consistency in period, depth, and duration provide adequate validation to guard against false alarms.

Table 1. Signal size vs. stellar type for jovian-size planets and main sequence stars

| Stellar type | Signal amplitude | Stellar radius |
|---|---|---|
| A0 | $1.8 \times 10^{-3}$ | 2.4 |
| A5 | $3.5 \times 10^{-3}$ | 1.7 |
| F0 | $4.5 \times 10^{-3}$ | 1.5 |
| F5 | $6.0 \times 10^{-3}$ | 1.3 |
| G0 | $8.3 \times 10^{-3}$ | 1.1 |
| G5 | $11.9 \times 10^{-3}$ | 0.92 |
| K0 | $14.0 \times 10^{-3}$ | 0.85 |
| K5 | $19.5 \times 10^{-3}$ | 0.72 |
| M0 | $28.1 \times 10^{-3}$ | 0.6 |
| M5 | $138.0 \times 10^{-3}$ | 0.27 |

For sufficiently bright stars, the precision of ground-based photometry is generally limited by atmospheric effects such as extinction and scintillation, but is also adversely affected by telescope tracking, detector noise, and variability of the comparison stars. (See discussions in this volume by Henry, Dunham, Howell, and Lockwood.) On photometric nights and when sufficient care is taken, it is possible to obtain measurements with an hour-to-hour relative precision of 1 to 3 millimagnitudes, i.e., a precision of 0.1% to 0.3%. (See papers by Henry and Lockwood, this volume.) By observing several transits and folding the data so that the transits align, planets somewhat smaller than jovian size should be detectable.

## Expected Detection Rate

The expected detection rate can be estimated from Equation (1).

$$P = P_d * P_p * P_a * P_3, \tag{1}$$

where $P_d$ is probability that a field star is a dwarf, $P_p$ is the probability that a dwarf star has a planet with a three- to six-day orbit, $P_a$ is the probability that the planetary orbit is aligned close enough to the line of sight to produce transits, and $P_3$ is the probability that six weeks of data will show three or more transits.

For a given magnitude, only about half the stars near the galactic plane are main sequence dwarfs. Many of the rest are giants that are too large to show a detectable signal. Thus only one-half the field stars can be considered as targets, and $P_d$ must be approximately 0.5.

Observations of solar-like stars by Butler et al., 1997, Mayor and Queloz, 1995, Cochran and Hatzes, 1997, and Noyes et al., 1997 have shown that approximately 5% of stars have giant planets. Approximately 40% of the stars with planets have periods between three and six days. Considering only those planets with such orbital periods, the probability that the orbital plane is near enough to our line of sight to show a transit is about 10%. (The slight increase in this fraction when planets with longer periods are included is ignored because of the low probability of recognizing these events.) Hence $P_p$ is about 0.02 and $P_a$ is near 0.1.

The value of $P_3$ was estimated from a numerical simulation. In the simulation, it was assumed that the observations were made for a constant number of hours each night and then transits were simulated for all possible phases for periods between three and six days. The fraction of events for which three or more transits occurred was recorded as a function of the number of nights of observations. The results are shown in figure 1, which shows that during seasons that observations can be carried out an average of 8 hours/night, and when six weeks of measurements have been accumulated, then $P_3$ is about 0.5. Hence the probability of detecting three transits per star that is monitored is the product of the probabilities P and is equal to $5 \times 10^{-4}$.

The yield, Y, is the product of the probability times the number of stars monitored $= (5 \times 10^{-4})$ x 4000 stars = 2 planets per six-week observation period. In summary, the expected yield is 2 planets per star field.
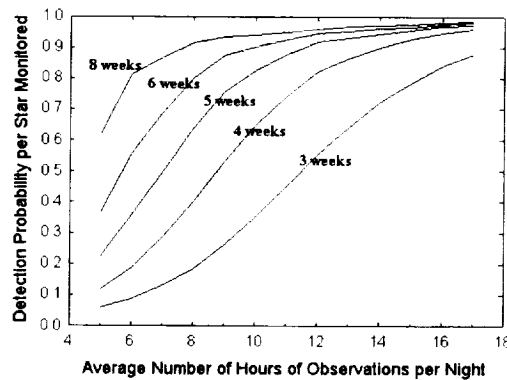


*Figure 1. The probability of detecting three or more transits for various choices of the length of night and the duration of the observations.*

As shown by Dunham (this volume), the number of useful target stars (and thus the expected planetary detection rate) is proportional to the area of the lens divided by the square of the focal length; i.e., proportional to the inverse square of the focal ratio. Hence very fast lenses are appropriate. As will be shown shortly, long focal lengths are needed to reduce the shot noise due to the sky background. To determine the capability of small-aperture, wide-FOV photometers, two photometers based on surplus lenses were constructed and tested.

## Instrument Description

The first version consisted of 15-cm focal length, F/1.5 Aerojet Delft lens, and a Kodak 2048 x 2048 format front-illuminated CCD with 9 μpixels. An autoguider telescope with a 1-meter (m) focal length was used to reduce the guiding jitter by the ratio of its focal length to that of the photometer. (See figure 2.)
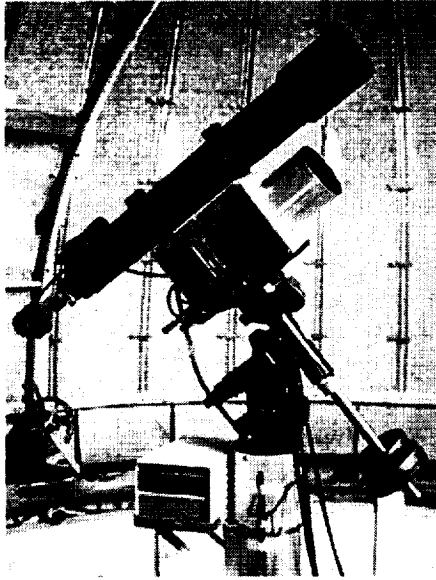
*Figure 2. Version 1 with original autoguider, mount, and counter weight system.*

The second version used a 30-cm fl, F/2.5 Kodak AeroEktar lens and a Kodak 4096 x 4096 format CCD with 9 μpixels. To maintain the same FOV, it was necessary to double the area of the CCD. Although the use of small pixels required large data files, they better sample the PSF. To stiffen the autoguider telescope, its length was shortened to 40 cm and a 2x Barlow lens was inserted to maintain a high ratio of the autoguider focal length to that of the photometer.

Both photometers have the same 49-square degree FOV, but the area of the sky subtended by each pixel in the V2 version is one-fourth that of the V1 version. Thus the noise contributed by the sky background is about a factor of two smaller in V2. As discussed later, the shot noise from the sky background seriously affects the ability of the AeroJet Delft lens to obtain high signal-to-noise-ratio observations of 11th and 12th magnitude stars. Because these stars are so much more common than brighter stars, their loss cannot be tolerated if a high detection rate is desired. Hence V1 was replaced by V2.

To mitigate the errors caused by image motion, several modifications were incorporated to V2. These include modifying the mount so that no axis flip is needed when the star field passes through the meridian and stiffening the photometer and autoguider structures to reduce flexure. The extended collar (which can be seen in figure 3 between the declination axis and the pier) moves the equatorial axis away from the pier so that the photometer can move past without collision. The photometer has also been moved past the equatorial axis and away from the pier. To balance the torque produced by the off-center photometer, the counterweight is supported by a jointed shaft that brings the weight behind the equatorial axis. Elimination of the axis flip substantially reduces the complexity of data-analysis effort because it allows the same stars to stay on the same CCD pixels throughout the night. Further, the substantial gap in the coverage caused by flipping the photometer and reacquiring the guide star is eliminated.

Nevertheless, even though an autoguider is used to keep the central star locked to the same pixels and very careful alignment of the polar axis is used, substantial image motion is still present.
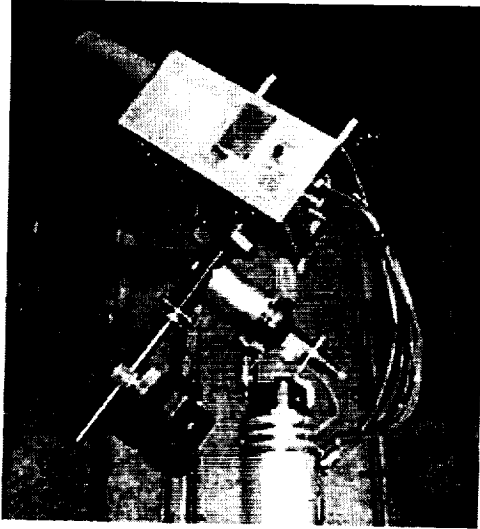
66

*Figure 3. Version 2 with longer-focal-length lens, shortened autoguider, extended mount, and off-center counterweight.*

## Point-Spread Function

To obtain good estimates of the stellar fluxes, it is important to have a point-spread function (PSF) that covers several pixels without having wings that are so broad that they spread the stellar flux over a large area of background sky and stars. Results of the tests that were conducted to determine the PSFs of both the AeroJet Delft and AeroEktar lenses are shown in figure 4. Both have PSFs wide enough so that the full-width-at-half-maximum (FWHM) widths cover three or more pixels and should, therefore, have critically sampled PSFs. Although the focal length of the AeroEktar lens is twice that of the Aerojet Delft lens, the angular sizes of their FWHM are similar and constrained by aberrations rather than diffraction.

A comparison of the enclosed energy versus the PSF radius is shown in figure 5. The wings of the AeroEktar PSF are very wide, the central portion of the PSF is asymmetrical, and the lens has a low transmission. Hence the AeroEktar lens cannot be recommended and will be replaced as soon as practical.

## Star Fields Observed and the Amount of Data Obtained

During the year since the system was set up, four star fields have been observed. Data from a total of 18 nights have been obtained from a field in Perseus; 13 nights with a V filter, and 5 nights with clear and I filters. The field is centered on the star 1Perseus at right ascension (RA) and declination (Dec) of $1^h 52^m$ and $+55°10'$. In April and May 1998, a field in Canes Venatici at $12^h49^m$ and $+42°13'$ was observed for four nights with a V filter. The third field observed was centered on Lamda Auriga at $5^h 19^m$ and $+40°06'$and a total of 10 nights were observed using the R filter. The fourth field was in Cygnus at $19^h46^m$ and $36°56'$. Observations were made with V filter for 22 nights with a minimum of 6 hours/night. These data are sufficient to determine the precision of the measurements and to conduct preliminary studies to examine the effects of using different color filters. Mena-Werth (this volume) showed that the largest spectral passband appears to give the highest precision.
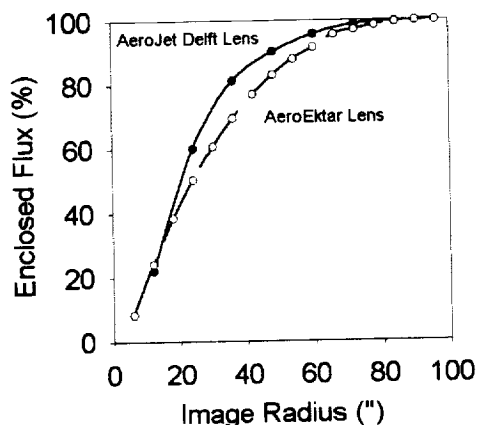
**Figure 4 chart:**

Enclosed Flux (%) vs Image Radius (")

AeroJet Delft Lens

AeroEktar Lens

*Figure 4. Comparison of the enclosed energy for the AeroJet Delft (solid circles) and the AeroEktar (open circles) lenses.*

**Figure 5 chart:**

Enclosed Flux (%) vs Image Radius (")

With Mask

No Mask
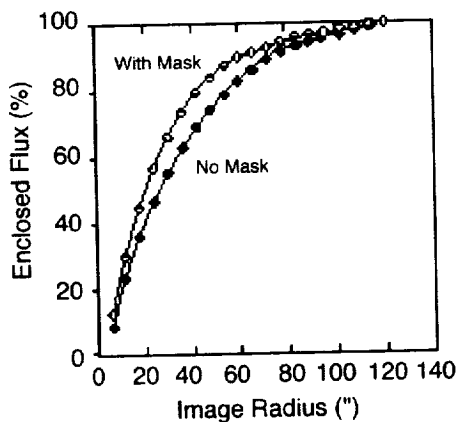
*Figure 5. Comparison of the enclosed energy for the AeroEktar lens with and without the F/3.5 mask.*

## Photometric Precision

For faint stars, the precision is controlled by a combination of shot noise due to the sky background and to the flux of the stars. For bright stars, the precision is expected to be limited only by scintillation noise. Figure 6 shows the measured hour-to-hour precision for V2 as a function of stellar magnitude in V.

The solid line is the measured precision. The long-dash curve represents the predicted total of scintillation and shot noise due to both the star and background. The dash-double dot curve represents the shot noise from the stellar flux, and the short-dash curve shows the predicted shot noise from the sky background. The horizontal dotted curve is the predicted scintillation noise for an airmass of 2.6.

It is clear that the precision is limited for stars fainter than 11th magnitude by the shot noise due to the star and background fluxes. However, for brighter stars, the attained precision is poorer

*Figure 6. Hour-to-hour precision obtained with V2.*

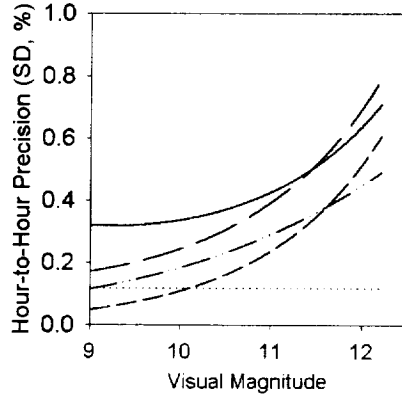than expected when only the shot and scintillation noise are considered. Further, the precision is nearly independent of stellar magnitude and much poorer than expected from scintillation noise, even at high air mass.

One possibility for the reduced precision of the bright stars is the motion of the images over the CCD. Because the polar axis is not perfectly aligned with the refracted pole, and because of the differential refraction over the large FOV, the image of the star field slowly rotates over the CCD surface during the night. For star images near the center of rotation, the rotation is less than 0.1 pixel per hour, but for star images several degrees away from that point, the image motions can reach 2 pixels per hour. In figure 7, the effect of this motion on the hour-to-hour precision is shown. No dependence is found. Further studies to determine the cause of the lower than expected precision shown by the bright stars are needed.

**Summary**

It is clear that to reduce the effect of shot noise from the sky background, it is important to use focal lengths of 30 cm or greater and to use small pixels. The use of small pixels provides better sampling of the PSF but requires large data files. Replacing the currently used lenses with new ones that have small focal ratios, large focal lengths, and high transmission can be expected to decrease the shot noise and thereby increase the expected detection rate of planets orbiting fainter stars. The origin of the noise that limits the hour-to-hour precision of the bright stars has not been identified.
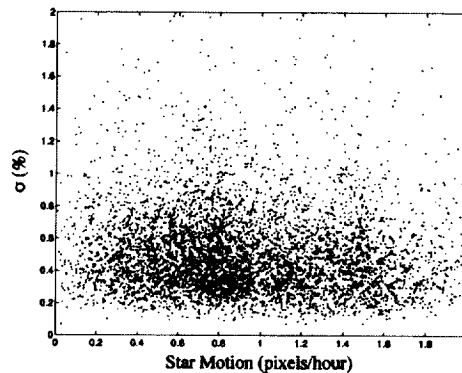


*Figure 7. Standard deviation of the hour-to-hour corrected fluxes versus the amplitude of the motion of the image centroids.*

## References

Butler, P.; Marcy, G.; Williams, E.; Hauser, H.; and Shirts, P.: Three New "51 Peg-Type" Planets. Astrophys. J. Lett., vol. 474, 1997, p. L115.

Cochran, W.; Hatzes, A.; Butler, P.; Marcy, G.: The Discovery of a Planetary Companion to 16 Cyg B. Astropyhs. J., vol. 483, 1997, p. 457.

Guillot, T.; Burrows, A.; Hubbard, W. B.; Lunine, J. I.; and Saumon, D.: Giant Planets at Small Orbital Distances. Astrophys. J. Lett., vol. 459, 1996, pp. L35–L38.

Mayor, M.; and Queloz, D.: Nature, vol. 378, 1995, pp. 355–359.

Noyes, R. W., et al.: Astrophys. J., vol. 487, 1997, pp. L111–L114.

Robinson, L. B.; Wei, M. Z.; Borucki, W. J.; Dunham, E. W.; Ford, C. H.; and Granados, A. F.: Test of CCD Precision Limits for Differential Photometry. Publ. Astron. Soc. Pacific, vol. 107, 1995, pp. 1094–1098.

# The Effects of Focus Settings on S/N and FWHM for Stars in a Crowded Field

Jose Mena-Werth
*University of Nebraska at Kearney*
*Kearney, NE 68849*

## Abstract

Focusing tests of the Vulcan Photometric Planet-Search Camera using standard V, R, I and clear filters are used to determine the effect of focus setting on both signal/noise ration (S/N) and full width at half maximum (FWHM) of star images in fields with different degrees of crowding. These four filters, in addition, were studied to determine which produced both the maximum S/N and minimum FWHM for stars near the center of the charged coupled device (CCD) frame. MIRA software was used for the photometric reductions, and air mass was not accounted for in this study.

## Background

The Vulcan Photometric Planet-Search Project is based at the NASA Ames Research Center under the direction of William Borucki. Its purpose is to record the transits of inner Jupiter-size planets across other stars. Since inner Jupiters are found around approximately 2% of planet-bearing stars, the Vulcan camera stares at crowded star fields with the goal of recording a 1% drop in flux from transited stars. The first year of operations used a 100-millimeter (mm) wide field camera permanently stationed at the Crocker Dome at Lick Observatory.

Four star fields were observed during the past year, one per season. Each field is 7 degrees (7°) on a side, contains thousands of stars, and is identified by its central star or its constellation. The four fields are named 1Per, λ Aur, CnV, and the Cygnus star field. During the initial observing run in October, November, and early December 1997, multiple filters were used on the 1 Per field. Because of the need for consistency in the observations, later star fields were observed with a single filter.

Three sets of focusing tests were performed. The I filter focusing test was on November 28, 1997; the R filter was tested on December 12, 1997; and the V, R and clear filters were tested on March 18 and 30, 1998. The focusing tests consisted of recording an image of a conveniently positioned star field at a given focus setting, and then changing the focus setting slightly and recording another image, and so on.

The multiple filter observations of the 1 Per field also allowed the comparison of the different filters in terms of which one produced the maximum S/N between star brightness and background and which filter produced star images with the minimum FWHM.

## Data

The data set for the focus data is a collection of CCD images taken with different filters where the micrometer focus setting is slowly changed and an image is recorded at each new focus setting. The focus setting changes were performed in one direction in order to eliminate mechanical backlash. These are raw CCD frames with no compensations for dark, flat, or bias images. A complete listing of data for the focus tests can be obtained from the author upon request.

Both the S/N and the FWHM measurements were made with the Mira Pro SL program. S/N is measured with a "bullseye" cursor composed of three concentric circles (see figure 1).
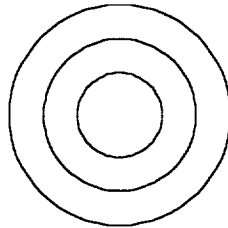


*Figure 1. S/N "bullseye" used for calculating the ratio of star brightness to background.*

The area of the inner circle surrounds the target star and sums the counts in each pixel. The annulus is the area between the two outer circles, and is used to calculate the background. The radii of the three circles can be changed, depending on the size of the target star and how crowded the field is around the target star. The radii changes are accomplished with the "set aperture parameters" command in the aperture photometry mode of the MIRA program.

The FWHM is a good indicator of the optimum inner radius for the aperture photometry target, but a more reliable method is to use the horizontal profile function. The best-fit inner radius is determined by plotting a horizontal slice of the image of the target star. The point at which the intensity histogram of the star first begins to merge with the background determines the inner radius. The annulus radii are determined by how closely surrounding stars crowd the target star.

For each focusing test, one star was selected near the center of the CCD frame, and its S/N and FWHM were measured. This method yielded one value of S/N and one value of FWHM for each focus setting. Care was taken to choose a star as uncrowded by neighbor stars as possible in order to improve the S/N and FWHM measurements. The star of moderate brightness was chosen so that neither saturation nor background noise was a significant factor.

**The Focusing Tests**

**The R filter.** The R filter was tested on three occasions—December 10, 1997, March 18, 1998, and March 30, 1998. The December 10 test is shown in figure 2. The expected inverse relation between S/N and FWHM is at once apparent. The vertical scale for all the focusing tests in this section are identical to enable easier comparisons. A consistent feature of this filter and the V and I filters is a displacement of the maximum S/N toward smaller focus settings than the minimum of the FWHM. It is also important to keep in mind that the December 10 and the March 30 tests were in crowded star fields where the blending of defocused starlight progressively decreases the S/N as one moves away from the maximum value. Without the effect of crowding, there is no distinct maximum and bell-shaped curve of the S/N. In an uncrowded star field, one would expect the S/N to stay constant because the photometric aperture can be sized to fit any size star image while the FWHM retains a minimum value with symmetric higher-value wings. The tests conducted on March 18 were in an uncrowded star field, and these latter effects will be evident there.
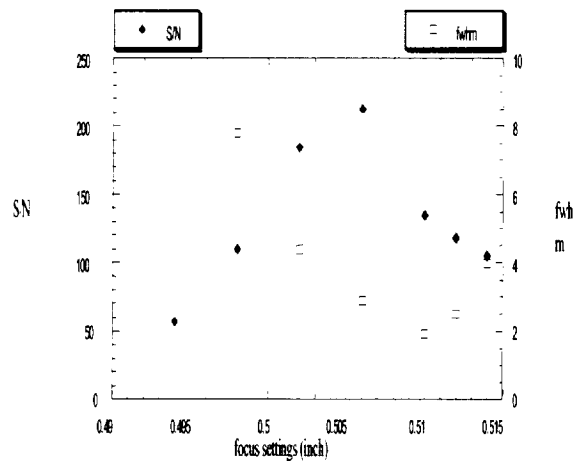
*Figure 2. Focus test for the R filter on December 10, 1997.*

The March 30 R filter focus test is shown in figure 3. This test has the most data points of any test and most clearly shows the maximum S/N ratio displaced to smaller focus settings than the minimum FWHM. The FWHM values for the 0.505- and 0.507- inch focus setting could not be calculated because they were too extended.
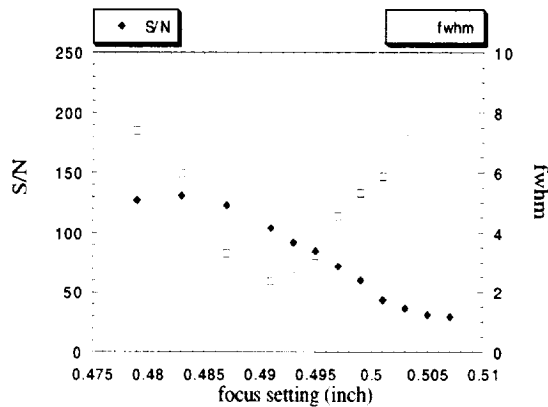


*Figure 3. The March 30, 1998, R filter focus test.*

The R filter focus test conducted on March 18, 1998 is shown in figure 4. As noted in the data section above, this test was on an uncrowded star field. The reason this test is not presented in chronological sequence is because it was never completed because of electronics problems. The March 30 test was the successful R filter test. Nevertheless, the uncrowded star field used on March 18 makes this test significant.

The most salient feature of the March 18 test is the flatness of the S/N curve. This flatness argues in favor of the suspicion that the bell curve of S/N is indeed a consequence of crowding. The sparseness of data points and the small span of focus setting, however, argues for more evidence before a definitive

answer is attained. There also is a slight progressive decrease in S/N with increasing focus setting. If the analysis had included flat, dark, and bias images as well as incorporating airmass, perhaps the decrease would not be there. Certainly, the next step in this study is to include the flat, dark, bias, and airmass corrections in the focus test analysis.
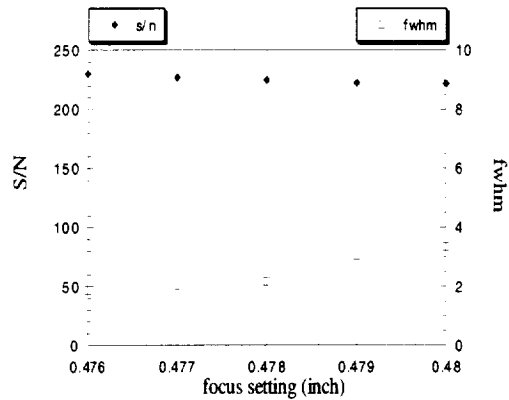


*Figure 4.  The March 18 R filter focus test.*

**The V Filter.** Two V filter focus tests were performed on March 30, 1998. The initial test, figure 5, was interrupted by an axis flip for the telescope (a problem corrected in the current Vulcan camera). This initial test is included because it complements the completed test shown in figure 6. In figure 6, the FWHM reaches a minimum at a focus setting of 0.495 inch while the S/N continues to increase with decreasing focus setting. As seen in the R filter focus test of figures 2 and 3, the S/N maximum continues to be toward smaller focus settings than the FWHM minimum.
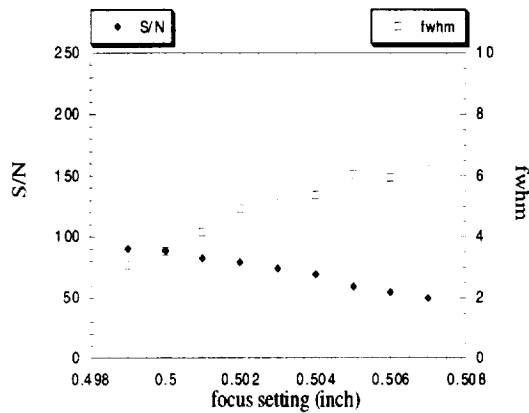


*Figure 5.  The initial march 30 V filter focus test.*
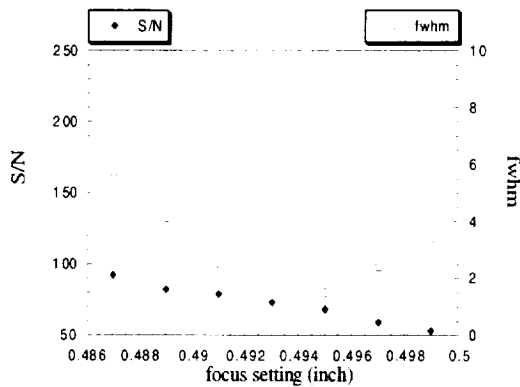
*Figure 6. The completed March 30 V filter focus test.*

**The I Filter.** The I filter focus test took place on November 28, 1997. This test was done with the telescope axis flipped. In figure 7, both the S/N maximum and the FWHM stand out, but they are not as well defined as in figures 2 and 3 for the R filter. Nevertheless, the displacement of the S/N maximum to smaller focus setting values as compared to the minimum of the FWHM remains consistent with the tests for the R and V filters.
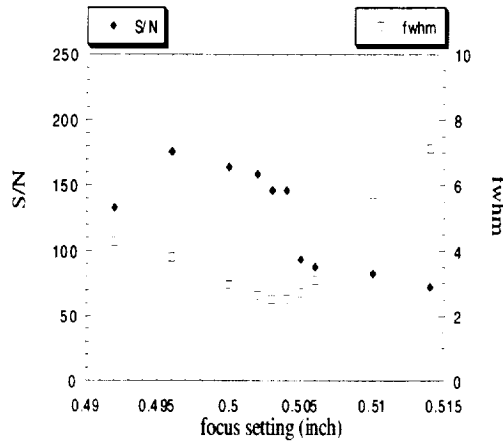


*Figure 7. The I filter focus test on November 28, 1997.*

**The Clear Filter.** The clear filter was tested on March 18, 1998. As with the test of the R filter in figure 4, this test was performed over an uncrowded star field. Figure 8 shows the results of this test.

s/n   fwhm

250 ─────────────────────── 10
                    ♦
         ♦                        ♦
200              ♦      ♦               ♦       8

S/N  150                                 6   fwhm

100                                       4

50                                        2

0 ──────────────────────── 0
0.54  0.545  0.55  0.555  0.56  0.565  0.57
            focus setting (inch)

*Figure 8. The clear filter test on March 18, 1998.*

In a similar way to the uncrowded R filter test of March 18, the clear test suffers from a lack of data points. This uncrowded field also displays the expected flat response of the S/N that is hinted at in figure 4. Unlike the R filter, however, the spread of focus settings is broader, and spans the FWHM minimum at a focus setting of 0.560 inch. Also unlike the R filter test, the clear filter does not show a progressive decrease in S/N with increasing focus settings.

## The Dependence of S/N and FWHM on Filter Choice

The original purpose of this report was to determine which filter produces the maximum S/N between star brightness and background. Only during the observations of th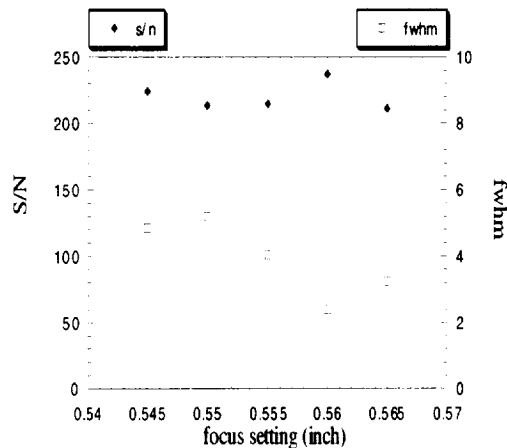e 1 Per field were multiple filters used. All observations for this section consequently are from the 1 Per data. For this part of the report, it was also important to use the same stars viewed through the different filter, so concentrating on a single field had an added benefit of allowing the same stars to be continuously monitored. In order to increase the continuity, all images are taken before the axis flip. The test stars occupy nearly the same pixels in the different images. The numerical data on the test stars are available from the author. The CCD used during the first nine months of the Vulcan Project had dimensions of 2K x 2K pixels. The four stars chosen were near the center of the CCD frame as their coordinates verify. The stars were chosen to represent different brightness with star 4 being the brightest. The S/N ratios of all the star images were measured with the concentric "bullseye" aperture having radii of three, six and ten pixels.

Figure 9 shows the dependence of the four test stars on the S/N ratio when viewed through different filters. The clear filter maximizes the S/N better than the other filters. It is important to note that the clear-filter exposure times were 90 seconds, whereas the V, R, and I filters required exposures of 180, 200, and 200 seconds, respectively. One possibility is that the shorter exposure time for the clear filter reduced the buildup of background more effectively than the longer exposures for the other filters. Another possibility is that scattered and reflected lights from San Jose more severely affect the V, I, and R filters producing more noise. This is one set of observations that would benefit from incorporating airmass in the photometry.
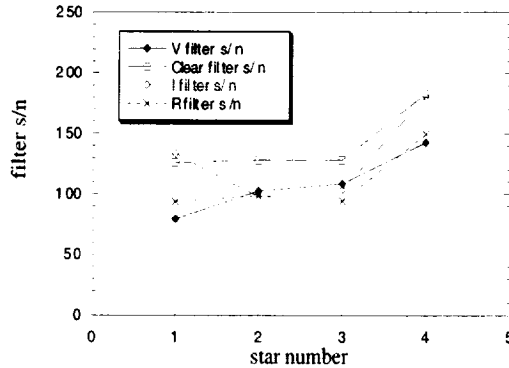
*Figure 9. The dependence of S/N on V, R, I, and clear filters for the same four stars in the 1 Per star field.*

The data points in both figures 9 and 10 were averaged over two consecutive observations in order to produce the ordinate values seen in these two graphs. The pairs of observations used were all taken within a span of ten minutes.

Figure 10 shows the dependence of FWHM on filter for the same four used in figure 9.
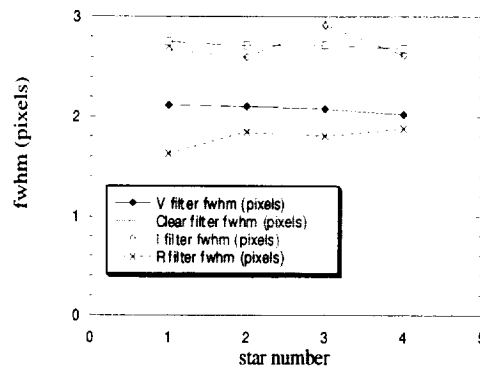


*Figure 10. The dependence of FWHM on R, V, I, and clear filters for the same four stars used in figure 9.*

The FWHM were measured with the MIRA program image profile function that fits a gaussian to the image of the star. The FWHM values were compared to the histogram of a horizontal cut through the image of the same star to ensure accuracy. The clear and I filters rendered larger star images than the R and V filters.

## Discussion

The focus tests show how crowding affects S/N and FWHM. In figures 2, 3, and 7 where the test was over a crowded star field, the S/N value shows a maximum value with decreasing values on either side. In the most complete tests (see figures 2, 3, 6, and 7), the S/N maximum is always displaced to smaller focus settings than the FWHM minimum. The reason for this effect is not understood. When the focus test was over an uncrowded field (see figures 4 and 8), the S/N shows no maximum. An uncrowded field also continues to display a clear FWHM minimum, as figure 8 demonstrates. In addition, figure 8 shows that in an uncrowded field there is no displacement of S/N and FWHM.

The displacement between S/N and FWHM in a crowded field might have the most profound effect on photometric planetary detection where the expected transit signal is a 1% change in flux. In figure 2, the minimum FWHM of 2 pixels and a S/N of 130 occur at a focus setting of 0.510 inch, yet changing the focus setting to 0.506 inch results in a FWHM of 3 pixels and a S/N of 210. In figure 3, the minimum FWHM of 2 pixels with a S/N of 100 occurs at a focus setting of 0.491 inch, yet changing the focus setting to 0.483 inch results in a FWHM of 5 pixels and a S/N of 130. In figure 7, the minimum FWHM of 2 pixels and a S/N of 150 occur at a focus setting of 0.503 inch, yet changing the focus setting to 0.495 inch results in a FWHM of 4 pixels and a S/N of 180. These examples imply that by slightly defocusing the image to smaller focus settings, one achieves at least a 20% increase in S/N.

In Section 4, where filters are compared as to which produced the largest S/N between star brightness and background, the clear filter was superior to the V, R, and I filters in producing star images with S/N 20% higher than the other filters. The sizes of the star images with the clear filter as determined by their FWHM, however, are 50 percent larger than the star images of the R filter.

The MACHO Project is also concerned with crowded star fields. Conversations with Douglas Welch, Christopher Stubbs, and Kem Cook of the MACHO Project revealed that no focusing tests were conducted because conditions at their site never permit better than two arc second seeing. Kem Cook selected the filter for their camera. He had two concerns. The filter had to minimize skylight; and since they split the light into a red and blue band, the filter also had to produce a balanced distribution of radiation in the two observed bands. He chose a broad filter that eliminated the sky bands beyond 780 nanometers (nm). His studies showed no clearly superior filter in enhancing S/N.

The next step in analyzing the focusing tests and filter study should be the incorporation of flats, darks, and biases frames. However, because the Vulcan Camera is at Lick Observatory just above San José, California, airmass might have the strongest influence on the photometry.

78

# A Testbed Search System for Extra-Solar Planet Transits at the University of Wyoming

Mark E. Everett and Steve B. Howell, Department of Physics and Astronomy,
*University of Wyoming, Laramie, WY 82071*

Derrick Ousley, Department of Physics and Astronomy,
*University of Alabama, Tuscaloosa, AL 35487*

## Abstract

We have developed a low-cost testbed system for detecting transits by extra-solar planets. The hardware consists of "off-the-shelf" components that, while presenting numerous of significant problems not encountered with higher-quality equipment, do allow us to develop reduction and data-analysis techniques, discover limitations affecting long-term, high-precision photometric survey projects, and formulate plans for future extra-solar planet searches. Within certain limitations on our usable field of view (FOV), we are able to obtain a set of long-term, high-precision light curves of field stars. This system also serves as a teaching laboratory for undergraduate astronomy majors and could be used as an effective low-budget facility to observe the behavior of bright variable stars.

## Hardware

The search system hardware consists of an 8-inch f/6.3 Meade Schmidt–Cassegrain telescope with a SBIG ST-8 charged coupled devices (CCD) system mounted at the focus (the CCD is Kodak model KAF1600). The telescope is equipped with an onboard LX200 computer and keypad to align the telescope axes and acquire targets. A Pentium class PC running Windows 95 is used with the CCDSoft software package to control the camera. The telescope is permanently mounted on a tripod on the roof of a University of Wyoming building.

The CCD consists of a 1530 x 1020 array of 9 micron pixels, resulting in a 37' x 24' FOV and a plate scale of 1.45 arcsec/pixel. For our SBIG ST-8 CCD, we have measured a gain of 2.7 electrons/ADU, a root-mean-square (rms) read noise of 11 electrons, and a dark current of 0.7 electrons/second at the nominal operating temperature of −15 degrees Celsius (°C).

## Data Acquisition

At the beginning of each clear night, the telescope axis encoders are initialized on a bright star and then the coordinates of the chosen search field are entered into the LX200 computer to acquire it. After making fine adjustments to pointing and focusing the telescope, we obtain a night-long time series of exposures of the search field. Our data have usually consisted of 3-minute exposures with a duty cycle time of 5 minutes. Approximately 45 minutes are required to set up the telescope in the evening, and the system is left to operate unattended through the night until shut down the next morning by the operator. Although the ST-8 camera includes a built-in ST-4 CCD for use as an autoguider, the CCDSoft program requires that time-series exposures be taken in a "focus" mode, precluding the use of the autoguider. As a result, our data are unguided. At the end of the night, all images, which have been stored as Flexible Image Transport System (FITS) files on a hard drive, are written to CDs for archiving and transported from the data-acquisition PC to UNIX workstations for data reduction and analysis.

## Telescope Performance

Typical seeing at our rooftop site coupled with troublesome telescope motions produce a stellar full width at half maximum (FWHM) of ~5 arcseconds, giving good spatial sampling, but resulting in unusual and time-variable point-spread functions (PSFs). In addition, the telescope focal plane suffers significantly from coma, further degrading the image quality toward the edges of the field. We obtain images in white light, which when combined with the red sensitivity of the CCDs results in a bandpass that is approximately a combination of the V- and R-band filters.

The unguided images and poor polar alignment of the telescope mount (due to its inexpensive design) result in a large-scale drift of the observed field during the night (typically the drift is 5 arcminutes over the full night). These motions, combined with variations in the stellar PSFs both in time and position across the field, impose the most significant limitations on using this system to acquire high-precision photometry. We discuss these problems in more detail below.

## Data Reduction

Image Reduction and Analysis Facility (IRAF) scripts have been written to reduce the data in an automated manner with very minimal setup time. First, a mean dark and bias exposure is subtracted from each image, and the result is divided by a flat field composed of twilight sky flats. The spatial shifts between each image are found using cross-correlation techniques, and a combined image of all data taken during the night is constructed so that the position of each star in the field can be found (using DAOfind). The positions are then used by IRAF's APPHOT aperture photometry package to measure stellar fluxes in a range of aperture radii for each star on each image.

The results from IRAF's aperture photometry are written out to a hard drive for archiving and input to custom FORTRAN programs that perform ensemble differential photometry on the entire data set (or optionally a subset of the data). These FORTRAN programs output light curve data files for each star (magnitudes, differential magnitude errors, observation times, etc.) as well as other documentation describing details of the data-reduction procedure. The comparison ensemble consists of ~10 bright stars that appear in each exposure. The light curve data files are read in by other FORTRAN programs to search for variability above a certain threshold. Interesting stars are then flagged for more detailed analysis and possible follow-up observations.

## Results

To examine the photometric precision of this system, we produce light curves for all stars in the field and compare the standard deviation of the observed magnitude measurements in each light curve to the uncertainties predicted by the signal-to-noise equation (see Howell and Everett in this volume). In figure 1 we plot the logarithm of the standard deviation of various light curves vs. their magnitude along with a line representing our predicted best precision for photometry of a single star at each magnitude. The nature of the results as seen in a plot like this depends on what data-reduction methods have been employed. For the data shown in figure 1, for relatively faint stars (magnitude (m)>12), we find an acceptable agreement with the predicted precision. The highest precision reached is ~0.005 magnitudes, or slightly better, per 3-minute exposure.
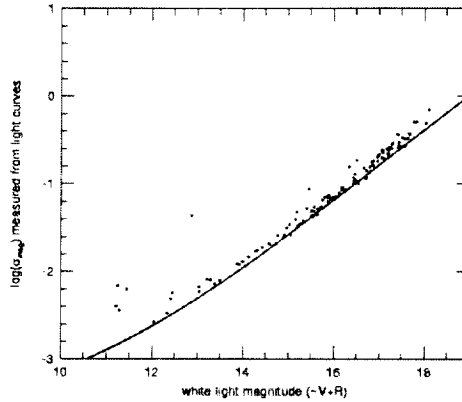
*Figure 1. The photometric precision as a function of magnitude measured from the observed light curves (the dots), and predicted based on the signal-to-noise equation (the line). The measured and predicted precisions agree fairly well for stars fainter than m = 12 (in white light), but the predicted precision is not attained for the brightest stars, as we discuss in the text. A cataclysmic variable, V592 Cas, was observed in this field and can be seen strongly deviating from the line at m = 12.8.*

Of greatest interest are the brightest stars for which we are most sensitive to the low-level variations caused by planetary transits, as well as any other effects present that would limit high-precision photometric photometry. Inspection of the light curves for the brightest stars (m<12) reveals systematic "wiggles" where the magnitude deviates from its mean. Unlike a source of random noise, these wiggles tend to persist over many consecutive exposures. Their artificial nature is revealed by the fact that neighboring bright stars tend to exhibit simultaneous wiggles. In figure 2 we show an example of a light curve with relatively large wiggles. In most cases the size of the wiggles is smaller (e.g., ~1% of the flux); however, this is still a significant problem when attempting to observe stellar variability at the 1% level.
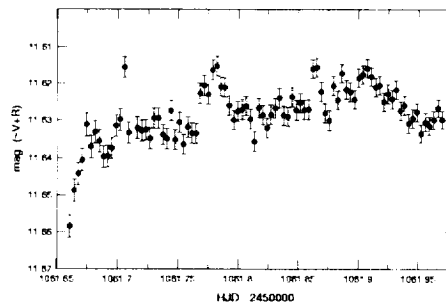


*Figure 2. A light curve showing systematic wiggles. These data were produced with a straightforward ensemble differential photometry reduction method that did not incorporate some of the "fixes" discussed in the text. The wiggle is apparently due to time-variable and pixel location-variable PSFs.*

We believe these wiggles are due to variations in the PSFs across the FOV combined with the telescope drift from poor polar alignment and other effects. This means that apertures used to measure the ensemble of calibration stars do not contain the same fraction of the total stellar fluxes as the apertures

used to measure other individual stars in the field and that this effect changes with each exposure. This explanation is supported by the improvements seen after optimizing the data reduction in three ways that alleviate the problem with the wiggles: a localized ensemble of comparison stars is used to correct for the extinction of each star of interest; the data reduction is confined to a region near the center of the field approximately 8 arcminutes across; and large-diameter extraction apertures (3–4 times the stellar FWHM) are being used in order to include a large percentage of the total stellar fluxes. We find that when using these large apertures, the noise for the brightest stars is still dominated by photons from the star.

Applying these "fixes" results in better precision, down to ~0.005 magnitudes or slightly better, for the brightest stars. The data shown in figure 1 are produced in this way. Even so, the brightest stars are not as precisely measured as would be predicted based on their total counts. The wiggles could play a role, but other noise-like sources of error seem to affect the brightest stars as well. In figure 3 we show the light curves of three stars that have been reduced in this way on two consecutive nights. Night-to-night repeatability is ensured by using the same ensemble stars, initial telescope pointing, and calibration data.
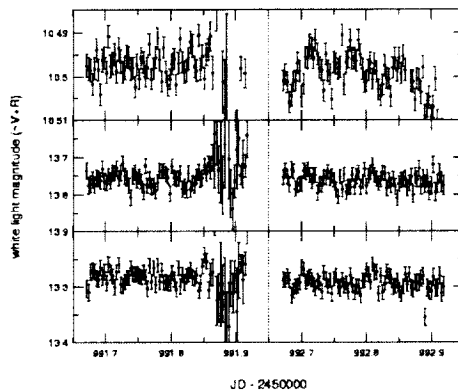


*Figure 3. Light curves of three different stars (ordered in the top to bottom pairs of panels) on two consecutive nights (the left and right panels). These three stars lie near the center of the CCD field, and were reduced using a localized ensemble and relatively large extraction apertures. The increasingly large error bars seen in the light curves at the end of the first night are attributable to cloud interference.*

## Conclusion

One motivation for experimenting with this testbed system is to determine the level of photometric precision attainable for a system that can be easily duplicated with a low budget and minimal effort. It is apparent that precisions better than 1% are attainable, a remarkable finding given the inexpensive hardware. One requirement of an effective extra-solar planet transit search program is that a very large number of stars must be observed at high precision. However, to obtain data at these precisions, we have been restricted to a relatively small FOV that, when combined with the small aperture of the telescope, results in a small sample of stars. Furthermore, we still do not reach the precisions expected for the brightest stars, and low-level systematic wiggles have not been entirely eliminated. The system is easily capable of monitoring or detecting high-amplitude variable stars (>0.1 magnitude) as faint as m = 16 and could be quite useful for teaching observational astronomy while gathering a unique data set for a targeted variable star (e.g., a Cepheid) as well as a few nearby field stars.

The main problems facing users of this equipment is the lack of guiding, difficulty of polar aligning the mount, mount instabilities, the shallow CCD well depths, and a simplistic data-acquisition software package. Although this system is inadequate for a long-term transit search program, it has allowed us to formulate the requirements of a larger, better (proposed) extra-solar planet transit search system.

# VAPHOT - A Package for Precision Differential Aperture Photometry

Hans J. Deeg

*Instituto de Astrofísica de Canarias, E-38200 La Laguna (Tenerife), Spain and
Centro de Astrobiologia, INTA, E-28807 Torrejon (Madrid), Spain*

Laurance R. Doyle

*SETI Institute, 2035 Landings Dr., Mountain View, CA 94043*

## Abstract

The aperture photometry package "vaphot" was developed to perform reliable and precise time-series photometry of uncrowded fields. This package works within the Image Reduction and Analysis Facility (IRAF) environment and is built upon the standard aperture photometry task "phot" from IRAF. The design goal of vaphot was a simple-to-use photometry task with relatively few input parameters that performs precise aperture photometry using optimum-sized apertures. The derivation of optimum-sized apertures is outlined; the calculation of these sizes is performed by a subroutine "apcalc" within the vaphot package. We also outline the derivation of signal-to-noise (S/N) values for differential photometry, when the flux reference is constituted by an ensemble of reference stars. A comparison of vaphot against normal aperture photometry shows that the sizing of apertures with the point-spread function (PSF) of the charged coupled device (CCD) images mitigates the effects of changes in the size of the PSF during an observing run. The use of apertures sized individually to each star on the field does not greatly improve photometry compared to the use of similar-sized apertures. However, the use of photometry with previously determined optimum aperture sizes ensures that this photometry will be of the best quality that can be obtained.

## Introduction

Differential time-series photometry has been used in many fields of astronomy to obtain information about temporal varying phenomena. Young et al. (1991) demonstrates how photo-tube measurements can obtain precisions of a few parts in $10^4$. Many of its aspects regarding the diminution of potential sources of errors can be applied to photometry based on CCD imagery as well. CCDs have meanwhile become more available than phototubes on most telescopes, and their instrumental precision for differential photometry is competitive, with theoretical limits on the order of 1 part in $10^5$ (Robinson et al., 1995). For the Transits of Extrasolar Planets (TEP) project (Deeg et al., 1997, 1998; Doyle et al., 1996, 1999), for which the software described here has been developed, the task was to measure the brightness evolution of *one* star (the program star) with a high precision against a set of reference stars. For precision time-series photometry with CCDs, this measurement task can be divided into two steps: the extraction of flux count values from the stars on the CCD frames, and the creation of a flux standard from the reference star(s), against which the brightness of the program star is measured.

Optimized data-extraction techniques have been addressed for aperture photometry by Howell (1989), and by Kjeldsen and Frandsen (1992) for a package that uses a "mixed" approach between aperture and PSF fitting. We note that photometry programs that depend purely on PSF fitting, such as "daophot" (Stetson, 1987) or "dophot" (Schechter et al., 1993), are *not* optimized for high-precision photometry of bright stars, a situation that is generally associated with time-series photometric projects. On the second step, techniques for the creation of flux standards, as well as evaluations of their stability, have been addressed by Howell et al. (1988), Gilliland and Brown (1988), and Kjeldsen and Frandsen (1992). The general consensus is that CCD photometry does have advantages over single-channel and

multichannel photo-tubes, the major one being that the program star *and* several reference stars can be measured simultaneously.

This communication is aimed at introducing a software package, *vaphot,*[1] for differential time-series photometry, using optimized data extraction, and introducing a way to create and to evaluate reference flux standards. These methods have been developed for the TEP project, whose major goal is the monitoring of the eclipsing binary star CM Draconis for the presence of planetary transits. These transits would express themselves as brightness dips with amplitudes of 0.1% to 1% of the quiescent brightness of the star, and would have a duration of typically one hour (Borucki and Summers, 1984; Schneider and Chevreton, 1990). In the course of this project, a very large number ( > 30000) of CCD frames has been obtained of CM Draconis and of some neighboring stars. These observations were taken at several observatories, and because of manpower restrictions, had to be reduced by the observers at their sites. It has, therefore, been necessary to obtain software packages that can deal efficiently with large numbers of CCD frames, that are relatively easy to use, and that deliver reliable and precise photometry. Preference was given to the IRAF environment because of its availability at the various sites and because of the observers' acquaintance with it. We found the standard tasks supplied in the IRAF-"ccdred" package fully sufficient for the basic image-reduction steps. The situation was more difficult with software to perform the differential photometry. Distributed within IRAF are two photometry packages: the "apphot" package for aperture photometry, which can be adapted to be used for large numbers of frames, but allows the use of only same-sized apertures for all stars within a CCD frame, and the daophot package, which employs PSF fitting, and is intended for crowded-field photometry rather then for differential-precision photometry. It is also relatively complicated to use, especially for consistent reductions of large numbers of frames.

Since the field of CM Dra is uncrowded, aperture photometry techniques should in principle be able to obtain the best precision. We evaluated the stand-alone MOMF package (Kjeldsen and Frandsen, 1992), whose photometry has been optimized for time-series CCD photometry. This package delivers results with excellent precision but is quite complicated to use, and its large number of output files with generic file names is not well adapted to the needs of the TEP project. We used this package, however, for reference evaluations. The program that is the topic of this paper, vaphot, was then developed as a task for IRAF. The vaphot program is built on the reliable aperture-photometry task phot from IRAF, but employs apertures that are sized to obtain optimum signal-to-noise ratios for *each* star in a CCD frame. It also fulfills the requirements of simple use, and creates for each night of observations just one output file that contains all needed data (instrumental magnitudes for all stars, sky brightness, tracings of full width at half maximum (FWHM), airmass, etc.), as well as a record of all relevant parameter settings that have been used. This output file is in straight ASCII text, to facilitate its interpretation by further reduction routines. In addition to the TEP project, vaphot has been used in a project to measure rotation curves of low-mass stars from their brightness variations (Martín and Zapatero-Osorio, 1997) and is used in an ongoing survey of minimum times of eclipsing binaries (Doyle et al., 1997). It is expected that this program will be of use for those investigators who need to perform precision time-series photometry of bright stars in uncrowded fields where aperture photometry is feasible.

---

[1] The programs vaphot, apcalc, and associated routines are available as part of the software distribution for the TEP project, at ftp://ftp.iac.es/pub/hdeeg/tep_dist/.

The points addressed in the following sections include:

- The aperture optimization used in vaphot

- Overview of the vaphot package

- The use of multiple reference stars as the flux basis; considerations about inclusion/exclusion of stars into flux basis

- Photometric performance of vaphot

## Calculation of the Signal-to-Noise Ratio for Aperture Photometry and Derivation of an Optimum-Sized Aperture

For time-series photometry based on CCD aperture photometry, the choice of the correctly sized aperture is of importance in obtaining lightcurves with the lowest possible noise. Clearly, in apertures too small, light from a star is wasted at the fringes of the PSF, whereas in apertures too big, unwanted noise—but no signal—is contributed from the inclusion of unnecessary sky background. The right-sized aperture, therefore, depends mainly on the size and the amplitude of the stellar PSF and on the level of background noise on the CCD. The flexibility in sizing the optimum aperture onto a CCD at the reduction stage can be considered an advantage over photometer-tube photometry, where the aperture has to be fixed before performing the observations. Finding this optimum-sized aperture for stellar CCD photometry in a simple-to-use photometry package is now outlined.

For the sake of clarity, signal and noise are expressed in units of electrons on the CCD; the conversion to CCD counts analog to digital unit (ADU) is trivial. Also, the aperture radius, r, is assumed to be in units of pixel side length. On the CCD, the signal, S, is the number of photons, $N_{ph}$, from the star inside an aperture with radius $r$, which is under the assumption of a Gaussian PSF with width $\sigma_{PSF}$ given by:

$$S = N_{ph}(r) = N_{ph,tot}\left(1-\exp\left(\frac{-r^2}{2\sigma_{psf}^2}\right)\right) \tag{1}$$

where $N_{ph,tot}$ is the total number of photons from the star in the limit of an infinite aperture. The total noise inside the radius r is given by the error-sum:

$$N = \sqrt{\sigma_{N_{ph}}^2(r)+\sigma_{BG}^2(r)+\sigma_{scin}^2} \tag{2}$$

where $\sigma_{Nph}(r) = \sqrt{N_{ph}(r)}$ is the photon noise from the star inside radius r, and $\sigma_{BG}(r)$ is the uncertainty in the contribution of the sky background to the total count within the aperture. If the average noise of one background pixel (from photon noise of the sky background and from CCD read-noise, is $\sigma_{1pix}$, then $\sigma_{BG}(r)$ is given by:

$$\sigma_{BG}(r) = \sigma_{1pix}r\sqrt{\pi} \tag{3}$$

The scintillation noise $\sigma_{scin}$ is a constant, which is independent of the magnitudes of the stars or the aperture used. Except for extremely short exposure times or with very small telescopes, $\sigma_{scin}$ will be much smaller then $\sigma_{Nph}$ or $\sigma_{BG}$, and can, therefore, be neglected in Equation (2). The ratio of Equations (1) and (2) gives then the S/N, and is also known as the "CCD equation" (Howell, 1989). Figure 1 shows the graph of S/N for a test image of CM Dra taken at the Mees Telescope of the University of Rochester. It is, of course, desirable that aperture photometry will be performed with apertures sized so that the S/N reaches a maximum. The programs to do this are the subject of the next section.
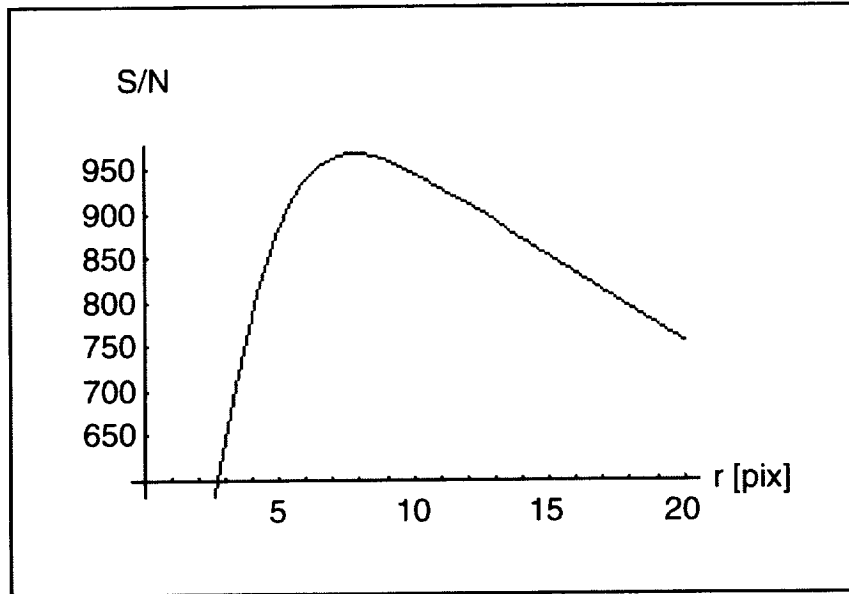
*Figure 1. The signal-to-noise ratio of aperture photometry of a stellar CCD image with dependence on the size of the aperture. The FWHM of the PSF of the star was 7 pixels (radius =3.5 pixels). The photon count from the star $N_{ph}$ was $1.1 \cdot 10^7$ electrons (at a gain of 4.1 $e^-/ADU$), and the noise of the background was 7 ADU. The radius of the optimum aperture is 7.8 pixels, corresponding to an aperture diameter of 2.23 times the FWHM.*

## The Photometry Routines apcalc and vaphot

The major programs ("tasks" in IRAF language) of the vaphot package are apcalc, which calculates optimized apertures, and the main vaphot task, which performs the photometry on a time series of CCD images, using the apertures calculated by apcalc. The package also provides an improved version of the IRAF task "imalign," called "imal2," which is intended for the aligning of large numbers of CCD frames.

Apcalc finds the optimum aperture sizes from a simple iteration that searches for the zero point in the derivative $\partial(S/N)/\partial r$. The only user input required is a CCD image containing the stellar field, a list of x-y coordinates of the stars on this field, and a value for the CCD gain. The program then measures the values $\sigma_{PSF}$, $N_{ph,tot}$, and $\sigma_{1pix}$ on the stars in this field, and finds the optimum aperture size for each star. Lastly, apcalc writes a file that contains the x-y coordinates of the stars and their optimum aperture diameter in units of the FWHM of the PSF (assuming a uniform PSF across a CCD image). This file can be used as an input to the photometry routine vaphot. Apcalc is normally used on only one image per night (or per observing run) for each stellar field observed. This reference image should be typical for the observing run in terms of seeing and sky brightness.

The vaphot program performs aperture photometry on a time series of CCD frames, with apertures sized individually for each star. An example of the vaphot input specifications is shown in figure 2. Items that need to be specified include the CCD images, a file for the results, a file

```
TASK = vaphot
images    =           @imlist   Images to do photometry on
result    =           940519c   Output file
stapcor   =   stapcor940519      File with object star coordinates and
                                  apertures
PSFcoord=   stapcor940519      File with PSF star coordinates
(fwhmini=               5.)    Initial FWHM for PSF fitting
(obstime=              HJD)    Time of observation image header
                                  keyword
(exptime=         EXPOSURE)    Exposure time image header keyword
(keyw1  =          AIRMASS)    1st auxiliary header keyword (i.e.,
airmass)
(keyw2  =          IMSHIFT)    2nd auxiliary header keyword
(verbose=              yes)    Verbose output
```

*Figure 2. Relevant input parameters for the vaphot task.*

with the position of the stars and aperture sizes (normally this is produced by apcalc), initial settings for PSF fitting, and the names of header keywords for exposure time and duration. Also
given is the option to include two more auxiliary image-header keywords in the results file, an inclusion that allows us to keep track of changing parameters (such as airmass) that are being logged in the image header. Also, if the images have previously been aligned with the imal2 task, a header keyword describing the X and Y shifts are created, which can subsequently be logged to the results file.

Although this is not intended as a manual for vaphot (detailed instructions are available at the same location as the software), we give here a short overview on the working of vaphot: On each image, vaphot measures the PSF on one representative star (if not oversaturated, the brightest stars would be suitable). The FWHM of this PSF is used as a basis to scale the apertures for each star by the value that has been calculated by apcalc.

The aperture sizes used on each star$_{s,k}$, where $s$ denotes the number of the star and $k$ the number of the CCD frame, are now given by: $a_{s,k}$ = FWHM$_k$ x aopt$_s$, where aopt$_s$ is the optimized aperture size calculated by apcalc for each star in units of FWHM, and FWHM$_k$ is in units of pixel size. This way, changes in the FWHM throughout at night can be accounted for. If there are drastic variations of the FWHM throughout at night, the *sizes* of the apertures used may deviate from the optimum aperture sizes for a particular image, but the relative brightnesses measured among the stars will not change. The aperture photometry that is then performed (using the aperture sizes $a_{s,k}$) on each *individual* stellar image is similar to the standard IRAF phot (vaphot is actually a "cl script"—or macro—built around the phot task). The only other major difference to the phot task is the format of the results file, which is adapted to the needs of time-series photometry. All measured magnitudes, several parameters that change throughout an observing run (Julian date, exposure time, FWHM, and parameters specified by the auxiliary header keywords), as well as relevant fixed parameters (such as the positions of the stars, aperture sizes, and the zero magnitude) are then written into *one* table in ASCII format, which is suitable to be plotted, or to be analyzed by programs outside the IRAF environment.

As is the case with all photometric methods, consistency of the results will degrade if the observing conditions undergo strong changes. Strong variations in the sky brightness, in the seeing, or in the transparency will cause the use of apertures that are not optimized for a particular image. In general, though, it is preferable to use only one set of optimized apertures for each night (or for each observing

run, if brightness variations on times scales of several nights need to be tracked). The S/N dependency of the aperture radii close to the optimum size (fig. 1) is very small, and sky-brightness changes from rising/setting of the moon, from normal seeing fluctuations, or from small (< 10%) transparency fluctuations do not deviate the apertures far from the optimum S/N. Changes in S/N as a result of a deviation from the optimum apertures are not very relevant relative to the variations to the S/N that are introduced by atmospheric fluctuations under marginal conditions.

## S/N in an Ensemble of Reference Stars

One of the major advantages of CCD photometry is the possibility of measuring simultaneously more than the usual one or two reference stars taken with photomultiplier tubes. This section evaluates the photometric precision that is given if such an ensemble of several stars is providing the brightness reference in differential photometry. The signal of an ensemble of $n$ reference stars is given by:

$$S_{ens} = \sum_{s=1}^{n} N_{ph,s}$$

(4)

where $N_{ph,s}$ is the photon count of each star $s$ within its aperture of radius $r_s$. The ensemble S/N is now:

$$S/N_{ens} = \frac{\sum_s N_{ph,s}}{\sqrt{\sum_s \left(N_{ph,s} + \sigma_{BG,s}^2\right)}}$$

(5)

Although the background noise of each pixel, $\sigma_{1pix}$, can be assumed to be the same everywhere on the CCD, it should be noted that $\sigma_{BG,s}$ is not the same for all stars, if differing sizes of $r_s$ where used (see Eq. 3), as is done by vaphot. The S/N of the *differential* photometric measurement for the program star is now given by:

$$S/N_{diff} = 1/\sqrt{S/N_{pro}^{-2} + S/N_{ens}^{-2}}$$

(6)

where S/N$_{pro}$ is the S/N of the program star, and can be determined from the CCD equation for single stars (the ratio of Equation (1) and Equation (2)).

As an example, table 1 shows the values of the optimized apertures and the S/N ratios from an image of the field of CM Dra, where seven reference stars where used for the ensemble reference. The parameters used are the same ones as given in the caption to figure 1.

One important consideration in the use of ensemble standards is that more reference stars are not necessarily better. The inclusion of faint reference stars with a low S/N can have a deteriorating effect on the ensemble S N! For example, excluding the faint reference star 7 of table 1 would raise the differential S/N to 593.

Since this consideration cannot usually be accounted for at the moment of performing the photometry, for the vaphot package a dual path was chosen: The output file contains a value for the differential photometry (magnitude (mag)$_{Program\_star}$ − mag$_{ensemble}$), but additionally, the magnitudes of all reference stars are recorded individually. This allows later removal of reference stars and a recalculation of the differential magnitudes, if reference stars are found to deteriorate the ensemble S/N because of their faintness, or because of variability. For these calculations, a program was written that allows the evaluation of individual reference stars from vaphot output files, recalculation of the differential photometry, rejection of individual points based on unusual variations among the reference stars, and generation of a final lightcurve. This program, named "vanaliz" and written in Interactive Data Language (IDL), is included in the software distribution. There exists also a prototype version with limited capabilities for Microsoft Excel, which can be requested from H. Deeg.

90

Table 1. Example of optimized apertures and S/N calculation for an ensemble of reference stars in the field of CM Dra.

| Star | $R_{opt}$[1] | $N_{ph}$ | $\sigma_{Nph}$ | $\sigma_{BG}$ | S/N[2] | mag[5] | magerr[6] |
|------|------|------|------|------|------|------|------|
| CM Dra | 2.23 | 1073271 | 1036 | 397 | 967 | 11.057 | 0.0011 |
| Ref *1 | 1.99 | 416501 | 645 | 354 | 566 | 12.085 | 0.0019 |
| Ref *2 | 1.75 | 141543 | 376 | 311 | 290 | 13.257 | 0.0037 |
| Ref *3 | 1.72 | 121210 | 348 | 306 | 261 | 13.425 | 0.0042 |
| Ref *4 | 1.68 | 96246 | 310 | 298 | 224 | 13.675 | 0.0048 |
| Ref *5 | 1.66 | 87339 | 296 | 295 | 209 | 13.781 | 0.0052 |
| Ref *6 | 1.58 | 52842 | 230 | 281 | 146 | 14.326 | 0.0074 |
| Ref *7 | 1.49 | 20345 | 143 | 265 | 68 | 15.363 | 0.0160 |
| Sum of Ref * | | 936027 | 967 | 801 | 745[3] | 11.206 | 0.0015 |
| CM Dra-(Sum of Ref *) | | | | | 590[4] | -0.149 | 0.0018 |

Notes to table 1:

[1]$R_{opt}$ is the optimum-sized aperture in units of FWHM of the PSF.

[2]S/N for individual stars is calculated by the ratio of Equations (1) and (2).

[3]S/N of the ensemble of reference stars is calculated with Equation (5).

[4]S/N of the differential measurement is calculated with Equation (6).

[5] Mag is magnitude, as converted from $N_{ph}$.

[6]The magnitude error is calculated from S/N as follows: magerr = 2.5 log (1+ N/S).

## Photometric Performance of the vaphot Program

Since vaphot is entirely based on standard aperture photometry, its performance on *single* stellar brightness measurements will be identical to the IRAF phot task. Where differences will occur is in the quality of measurements of ensembles of stars, and of sequences of CCD frames. A detailed comparison of vaphot to some other reduction packages is beyond the scope of this paper and is the subject of a forthcoming article. In the following, a comparison between optimized aperture photometry and conventional aperture photometry with similar-sized apertures (for all stars) and/or with constant-sized apertures (independent of the PSF) is outlined.

In table 2, the noise of the differential photometry of a night (June 6, 1999, observed at the Crossley 36-inch telescope at Lick Observatory) of observations of CM Draconis is shown. This night was characterized by a strong change in the size of the PSF, from variations in the seeing and possibly in the focusing of the telescope. The column rms (root mean square) gives the standard deviation of the differential lightcurve against a nightly mean. The "LF rms" indicates the low-frequent noise, giving deviations over a longer time scale of about one-half hour; these deviations were obtained by smoothing the resultant lightcurve with a boxcar with a length of nine data points. The "HF rms" indicates the high-frequent or "point-to-point" noise, which was obtained by subtraction of the smoothed lightcurve from the original curve.

As can be seen, the major difference is in the rms or LF rms between photometry whose apertures scale with the PSF, and photometry whose aperture do not. This was caused by the strong changes in the size of the PSF, which occur on slower time scales and do not much affect the point-to-point noise (HF rms). \

Table 2 Comparison between different aperture photometry methods

| Description | rms (mag) | LF rms (mag) | HF rms (mag) | Apertures optimized for each star | Apertures scale with FWHM |
|---|---|---|---|---|---|
| The vaphot program (optimized apertures, scaling with FWHM of PSF) | 0.0044 | 0.0029 | 0.0031 | Y | Y |
| Apertures of radius 2.5 x FWHM for *all* stars, and scaling with FWHM of PSF | 0.0042 | 0.0026 | 0.0031 | N | Y |
| Optimized apertures for reference image, but apertures kept constant during night | 0.0068 | 0.0057 | 0.0032 | Y | N |
| Apertures of radius 16 pixels[1] for *all* stars, and apertures kept constant during night | 0.0061 | 0.0047 | 0.0035 | N | N |

[1] *16 pixels corresponds to 2.5 times the FWHM of 6.5 pixels of the reference image.*

The difference between apertures of optimum size for *all* stars and the use of a constant aperture of 2.5 x FWHM for all stars is not very profound. It should, however, be noted that the optimized apertures for all stars are relatively close to 2.5 x FWHM (between 2.6 and 1.9 x FWHM) and that the dependence between S/N and size of aperture is not very strong near the optimum (see fig. 1). The major advantage in the use of apcalc and vaphot is, therefore, that the guesswork "what is the best size for my apertures?" is completely taken care of. This is true for any combination of observing conditions (brightness of stars, brightness of background, gain of camera, size of telescope, etc), in a package that is straightforward to use, and will derive precise aperture photometry.

# Bibliography

Borucki, W.J.; and Summers, A.L.: Icarus, vol. 58, 1984, p. 121.

Deeg, H.J.; Martín, E.L.; Doyle, L.; Jenkins, J.; Schneider, J.; Chevreton, M.; and Palaiologou, M.: Astronomical and Astrophysical Transaction, vol. 13, 1997, p. 233.

Deeg, H.J.; Doyle, L.R.; Kozhevnikov, V.P.; Martin, E.L.; Oetiker, B.; et al.: Astronaut. and Aeronaut., vol. 338, 1998, p. 479.

Doyle, L. R.; Deeg, H. J.; Jenkins, J. M.; Schneider, J.; Ninkov, Z.; et al.: in Brown Dwarfs and Extrasolar Planets, R. Rebolo et al., eds., ASP Conference Proc., vol. 143, 1997, p. 224.

Doyle, L. R.; Deeg, H. J.; Kozhevnikov, V.P.; Oetiker, B.; Blue, J.E., et al., submitted, 1999.

Doyle, L. R.; Dunham E.T.; Deeg H. J.; Blue J.E.; and Jenkins J. M.: J. Geophys. Res. – Planets, vol. 1, p. 14823.

Gilliland, R.L., and Brown, T.M.: Publ. Astron. Soc. Pacific, vol. 100, 1998, p. 754.

Howell, S.B.: Publ. Astron. Soc. Pacific, vol. 101, 1989, p. 616.

Howell, S. B.; Mitchell, K.J.; and Warnock III, A.: Astrophys. J., vol. 95, 1998, p. 247.

Kjeldsen, H., and Frandsen, S.: Publ. Astron. Soc. Pacific, vol. 104, 1992, p. 413.

Martín, E. L., and Zapatero-Osorio, M.R.: Monthly Notices of the Royal Society, vol. 286, 1997, p. L17.

Robinson, L.B.; Wei, M.Z.; Borucki, W.J.; Dunham, E.W.; Ford, C.H.; and Granados, A.F.: Publ. Astron. Soc. Publ., vol. 107, 1995, p. 1094.

Schechter, P.L.; Mateo, M.; and Saha, A.: Publ. Astron. Soc. Pacific, vol. 105, 1993, p. 1342.

Schneider, J., and Chevreton, M.: Astronaut. and Aeronaut., vol. 232, 1990, p. 251.

Schneider, J., and Doyle, L.: EM&P, vol. 71, 1995, p. 153.

Stetson, P.B.: Publ. Astron. Soc. Pacific, vol. 99, 1987, p. 191.

Young A.T. et al.: Publ. Astron. Soc. Pacific, vol. 103, 1991, p. 221.

# An Astronomical Test of CCD Photometric Precision

David G. Koch
*NASA Ames Research Center, Moffett Field, CA 94035-1000*

Edward W. Dunham
*Lowell Observatory, 1400 Mars Hill Road, Flagstaff, AZ 86001*

William J. Borucki
*NASA Ames Research Center, Moffett Field, CA 94035-1000*

Jon M. Jenkins
*SETI Institute, 2035 Landings Road, Mountain View, CA 94043*

## Abstract

Ground-based differential photometry is limited to a precision of order $10^{-3}$ because of atmospheric effects. A space-based photometer should be limited only by the inherent instrument precision and shot noise. Laboratory tests (Robinson, et al., 1995; Jenkins, et al., 1997) have shown that a precision of order $10^{-5}$ is achievable with commercially available charged coupled devices (CCDs). We have proposed to take this one step further by performing measurements at a telescope using a Wollaston prism as a beam splitter. First-order atmospheric effects (e.g., extinction) will appear to be identical in the two images of each star formed by the prism and will be removed in the data analysis. This arrangement can determine the precision that is achievable under the influence of second-order atmospheric effects (e.g., variable point-spread function (PSF) from seeing). These telescopic observations will thus provide a lower limit to the precision that can be realized by a space-based differential photometer.

## Objective

This investigation directly addresses the CCD system-level proof of concept at the one-part-in-$10^5$ level by construction and use of a ground-based testbed to demonstrate technological readiness for the Kepler Mission (Borucki, et al., 1997; Koch, et al., 1996). The testbed attempts to reproduce or come as close as practical to as many characteristics of the proposed space mission as are feasible. Specifically, the characteristics to be demonstrated include:

- Use of a real star field, along with associated background stars and diffuse galactic background;
- Use of real stellar spectra rather than a monochromatic LED;
- Use of the same ratio of PSF to pixel size as in the Kepler Mission baseline design.
- Data processing similar to the proposed onboard data handling;
- Flux levels that are the same to show that the precision can be achieved in the same time interval;
- Shutterless operation during CCD readout, as in the space mission;
- A back-illuminated CCD that is thinned, delta doped, annealed, and anti-reflection coated;
- Use of a two-channel readout to identify potential cross-talk effects;
- Dark current at the proposed operating temperature; and
- Charge transfer efficiency (CTE) and full well capacity similar to that for the Kepler Mission.

The ground-based observational test will be adversely affected by several effects that do not apply to the space-based case. This implies that the precision achieved by the ground-based observations will be a lower limit to the achievable precision of a space-based photometer. In particular:
- The pointing jitter will be greater than that expected for the spacecraft.

- The size and shape of the PSF will be variable.
- Nonlinear response in the CCD may result in incomplete removal of common-mode brightness changes due to extinction.
- Each star image can use its oppositely polarized twin only as a comparison object rather than using many stars in the field, as the space-based system will.
- The CCD electronics will not have been optimized for very high-speed read rates.

**Significance of Test**

A photometric space mission has many capabilities that can contribute to a fuller understanding of the frequency of occurrence and character of planets in general and uniquely to that of Earth-size planets. Our proposed mission concept has evolved (Koch, et al., 1996) to that of continuously and simultaneously monitoring 100,000 dwarf stars with no bias as to the spectral type of star to investigate. This will lead to results on characteristics of planets for a wide variety of stars, including binary and other multiple star systems. The same system can also detect giant planets around the G-giant stars that will also be monitored in the same field of view (FOV). Photometry is complementary to the other existing and proposed methods. For example, a nulling interferometer cannot be used to observe planets in binary systems because it creates only a single null and is limited to only the nearest stars, which are mostly M-dwarfs. The radial velocity method is limited to stars later than mid-F dwarfs because of the need for sufficient spectral structure in order to measure the reflex velocity. Photometry is currently the only feasible method for detecting a statistically significant sample of Earth-size planets and characterizing each case.

Although ground-based methods can detect giant planets and determine their properties and microlensing could provide a broad statistical sample of outer-planet frequency for galactic bulge stars, transit photometry is the only currently feasible method for detecting and characterizing Earth-size planets in the continuously habitable zone (CHZ) of a large sample of stars in the extended solar neighborhood of the galaxy. Three characteristics determine if a planet is potentially habitable:

1) The characteristic surface temperature of the planet (assuming a blackbody), a parameter that determines if liquid water can exist. The temperature depends on the stellar luminosity and the distance of the planet from its star. (The albedo and emissivity are needed to be more precise, but enter only to the one-fourth power);
2) The planet mass, which determines if it can have crustal recycling and if it can retain an appropriate atmosphere or will attract a massive atmosphere, making it uninhabitable; and
3) The spectral type of the star, which determines the length of time the climate of the planet is continuously habitable (Kasting, et al., 1993).

Photometry can address all three of these characteristics, namely:

1) From the period and the stellar mass (inferred from the spectral type of the star), the orbital semi-major axis is calculated. From this and the stellar luminosity, the characteristic temperature can be calculated.
2) From the change in apparent brightness during a transit and the stellar size, the planet size (not just a lower limit) is calculated. If a density is assumed, the mass can be estimated.
3) For the brighter stars, measurement of p-mode oscillations with Kepler can be used as a direct measure of the stellar properties, specifically the mass to a few percent and age to about 5% (Brown and Gilliland, 1994). The spectral classification of the other stars will be used to determine their characteristics.

Results from the Kepler Mission will provide a statistically significant sample of extrasolar planets; will determine the basic properties of the systems detected; will have the unique capability to detect and characterize Earth-size planets in the CHZ; and will provide candidate planetary systems that the Space Interferometry Mission can search for giant companion planets. The significance of the

results from this testbed will be to define a lower limit to the achievable precision of the photometric method at the system level using real stars and a CCD system similar to that proposed for the Kepler Mission.

## Previously Achieved Photometric Precision

We have conducted laboratory measurements to investigate the intrinsic precision of both front- (Robinson, et al., 1995) and back-illuminated Reticon 512 x 512 CCDs with 27-micrometer ($\mu$m) pixels (Jenkins, et al., 1997). The back-illuminated CCD was thinned and delta-doped (Nikzad et al. 1994). It has a full well capacity of about 4 x $10^5$ e$^-$ in multipinned phased (MPP) mode and a read noise of 12 e$^-$ at $-109$ degrees Centigrade ($^\circ$C). The CCD was operated using the SNAPSHOT data-acquisition software (Dunham et al. 1985, and Dunham, 1995), providing a constant exposure time. The optical system included a 660 nanometer (nm) LED, diffusers, condensing lenses, several artificial star-field plates, and imaging lenses. Light from the LED passed through the star-field plate, producing resolved images of the holes in the plate. The star images were about seven pixels in diameter full width at half maximum (FWHM) on the CCD. The entire projection system was mounted on a micropositioning stage, which provided reliable subpixel motion in both the column and row directions. No shutter was used, thereby simulating the Kepler Mission operation. The instrument was mounted vertically for mechanical stability and enclosed in a temperature-controlled housing. Data were accumulated as sums of 20 or 40 2.5-second (sec) exposures on 3-sec centers, resulting in approximately 2.4 x $10^8$ e$^-$ or 4.8 x $10^8$ e$^-$ in each summed image.

The system was used to conduct numerous performance tests, including:

- The effects of "star trails" resulting from reading out without the use of a shutter;
- The effects of background stars up to five stellar magnitudes fainter at 10, 20, and 40 pixels from the target star; and
- The effects of subpixel motions on the photometric precision.

All effects were found not to degrade the precision beyond the required level of 1 x $10^{-5}$. In each test, the summed images obtained during the experiment were processed to obtain relative light curves for each of the 13 artificial stars. Overclocked pixels were used to estimate the bias level, which was then subtracted from each pixel. Dark current was negligible at the operating temperature relative to the signal. The flux time series for each star was obtained by summing the counts in a 15- x 15- pixel window. This windowing size was chosen so that it contained at least 80% of the light of each star. No nonlinearity or flat-field corrections were applied to the images. The flux time series of each star was divided by the sum of the fluxes of all the other stars to obtain a relative flux. This was normalized to its mean value. Linear least-squares regressions were performed using the x and y coordinates (measured by the centroid of each star) as the independent variables. Finally, the residual relative fluxes were bin-averaged by successive powers of two to assess their values for longer time scales.

As an example of one run, subpixel scale motions similar to those expected for the Kepler Mission were applied to the apparatus. The motions for this test consisted of moving the star images over a 0.08- x 0.05- pixel grid in nine uniform increments. After correction for motion, almost all the scatter in the residuals can be accounted for by shot noise, yielding a residual instrument precision of better than three parts per million (ppm) at an integrated flux of 5.1 x $10^9$e$^-$. The motions were much larger than the pointing jitter anticipated for the Kepler Mission, so that even better precision may be achieved in practice.

In summary, back-illuminated CCDs are found to be essentially shot noise-limited differential-photometric detectors when the effects of image motion are calibrated. At the demonstrated precision of better than 3 ppm at a flux of 5.1 x $10^9$ e$^-$, these CCDs are capable of detecting 80 ppm in the

brightness change of a star caused by transits of Earth-size planets in orbit about solar-like stars. However, other effects, such as very crowded starfields and realistic point-spread functions, might be troublesome and were not simulated in these tests.

## Description of the Testbed

The overall guideline for the testbed is to replicate the parameters and configuration of the space-based mission as closely as practical with the ground-based testbed equipment and observing procedure using the Crossley telescope at Lick Observatory (Stone, 1979).

Based on our laboratory testing, we have defined the requirements for an optimum CCD for the space mission. We have contacted numerous vendors and found that EEV can currently provide the closest match to these requirements. A comparison of the characteristics of the space-based Kepler Mission configuration with that of the Crossley testbed is shown in table 1. The CCD we are using for this testbed is an engineering-grade EEV CCD42-80. The device has three times as many bad pixels as the limit for a Grade 1 and 22 bad columns (four times the Grade 1 limit).These CCDs have a read noise of about 30 electrons at a one megapixel per sec read rate with the on-chip amplifier operating at low gain, and good CTE at this speed. They are backside illuminated and anti-reflection (AR) coated for a peak quantum efficiency of over 80%. Backside charging is achieved with ion implantation followed by laser annealing. This procedure results in stable quantum efficiency and allows use of aluminum clock lines, resulting in high clock speeds. The format is 2k x 4k with 13.5 micron square pixels. There are two readout amplifiers on the CCD, each servicing a 1k x 4k section of the CCD. With two amplifiers, the readout time would be four seconds. However, by binning 2 x 2 the read time will be one second. A modification of this basic design with 2k x 1k 27 micron pixels with two amplifiers each servicing a 1k x 1k section, is a strong candidate for a flight detector for the proposed Kepler Mission. Thus the CCD42-80 is a very good choice for this testbed. We will operate the CCD at various temperatures to determine the impact of dark current on the differential photometric precision. The image in the testbed will be defocused so that the total well capacity per star will match that for the space mission.

Table 1  Kepler Mission versus Crossley testbed characteristics

| Parameter | Kepler Mission | Crossley testbed |
|---|---|---|
| Aperture | 0.95 meter (m) | 0.90 m |
| System f# | 1.4 | 5.8 |
| Optical design | Schmidt with individual field flatteners at focal plane | Prime focus with beam splitter |
| Tracking | ~0.1 arcsec, 1 $\sigma$ | ~1 arcsec |
| Shutter for readout | None | None |
| Plate scale | 3.6 arcsec/pixel | 0.5 arcsec/pixel |
| Defocus | 7 pixels (25 arcsec) | 14 pixels (7 arcsec) |
| Bandpass | 0.4–1.0µ | 0.4–1.0µ - sky glow filter |
| CCD | 2048 x 2048 (54 x 54 millimeter (mm) | 2048 x 4096 (27 x 54 mm) |
| Preparation | Backside thinned delta doped, AR coated | Backside thinned delta doped, AR coated |
| Pixel size | 27µ x 27µ | 13.5µ x 13.5µ |
| FOV | 12° x 12° | 17' x 34' to overlapping beam |
| Vendor | EEV, SITe, MITLL, or others | EEV |
| Well capacity | 5 x $10^5$ electrons/pix | 1.2 x $10^5$ electrons/pix |
| Light source | Real stars | Real stars |
| Readout rate | 2 megapix/sec/amplifier | 1 megapix/sec/amplifier |

A controller developed by Robert Leach's group at the University of California, San Diego (UCSD) will be used to read out the CCD at nearly one megapixel per second. This second-generation device (Leach, 1996) is the fastest highly programmable controller available. It is currently in use at

more than 20 observatories. The device uses an S-bus interface. Online documentation is available at http://mintaka.sdsu.edu/ccdlab/LabMain.html.

Initially a Sparc Model IPX was used to run the controller. But the Model IPX was found to be too slow for the 1-megapixel/sec readout rate and has been replaced with a Sparc 5 running at 110 megahertz (MHz). Additional application-unique software (LOIS, Lowell Observatory Instrument Software) is being developed both for this camera and other instrument development programs.

## The Testbed Beam Splitter

A key component of the testbed is a beamsplitter that will create two photometrically identical images of the real sky. The beamsplitter does not have to create flawless images. It only needs to maintain a brightness ratio for any pair of rays from the sky constant to $10^{-5}$ or better. A calcite beamsplitter known as a Wollaston prism has been chosen for this purpose, with the optical design shown in figure 1. Calcite has the property that the indices of refraction for each polarization of the light differs by about 0.18 for a wide range of wavelengths. Using a small angle approximation for Snell's Law for a calcite prism with a prism angle of $\theta_p$ and normal incident light, the angle of the ordinary and extraordinary rays, $\theta_o$ and $\theta_e$, are given by:

$$\theta_o = \theta_p n_o, \quad \theta_e = \theta_p n_e \quad and \quad \Delta\theta = \theta_p(n_o - n_e) \quad (1)$$

where $n_o$ and $n_e$ are the ordinary and extraordinary indices of refraction of the calcite. Values of the index of refraction for calcite are listed in *The Infrared Handbook*, Table 7-21. For a prism angle of 3°28', the exit angle is 1°12'. For a distance to the CCD of 145 mm, the image separation is 228 pixels or 3.00 mm. The CCD dimensions and readout direction are illustrated in figure 1. It is important to note that the image is read out orthogonal to the beam splitting direction, because a shutter is not used, just as in the case for the space mission.

Several features of the optical design follow:

1) Prior to being split, every ray passes through the same atmospheric distortion, the same path in the telescope, and the same part of the window material.
2) The beam passes through the calcite while it is still large, reducing the effect of dust and manufacturing imperfections.
3) The only places where cleanliness is critical are the exit side of the calcite and the CCD, which are kept clean by being inside of the dewar.
4) Since most of each beam passes through the same calcite, only the effects of scratches, defects, or specks within 25μ of the edge of each beam can modulate the ratios (see calculation below.)
5) The Wollaston prism is parallel to the focal plane and CCD so that both images are kept in focus. Ghost images will be highly defocused and of low surface brightness.
6) Additionally, a polarizer can be inserted into the beam to select one or the other of the polarizations during instrument checkout.

The only things that could modulate the ratio of the light in the two beams for any given star are defects in the calcite crystal, scratches, or dust on the exit surface in that small portion of the beam that is not common to both as the image jitters. For a one-arcsec jitter of the telescope, the beam moves by 25 micrometers (μm) at the calcite, amounting to a different beam area of 0.875 mm² for which a change in contamination might change the intensity ratio. Dirt and imperfections larger than 100 μm are readily detectable with the unaided eye. A typical human hair is about 75 μm. Both are larger than

Removable polarizer:
For checkout with
one beam only

BK-7 Window
75 mm dia x 14 mm

Dewar wall

Wollaston prism
Calcite birefringent
3° 28' wedge
1° 12' divergence
50 mm square

144 mm

f:5.8 beam

EEV 42-80CCD:
27x54mm
2048x4096 pixels

Plate scale:
    0.5 arcsec/pixel=38 secs/mm
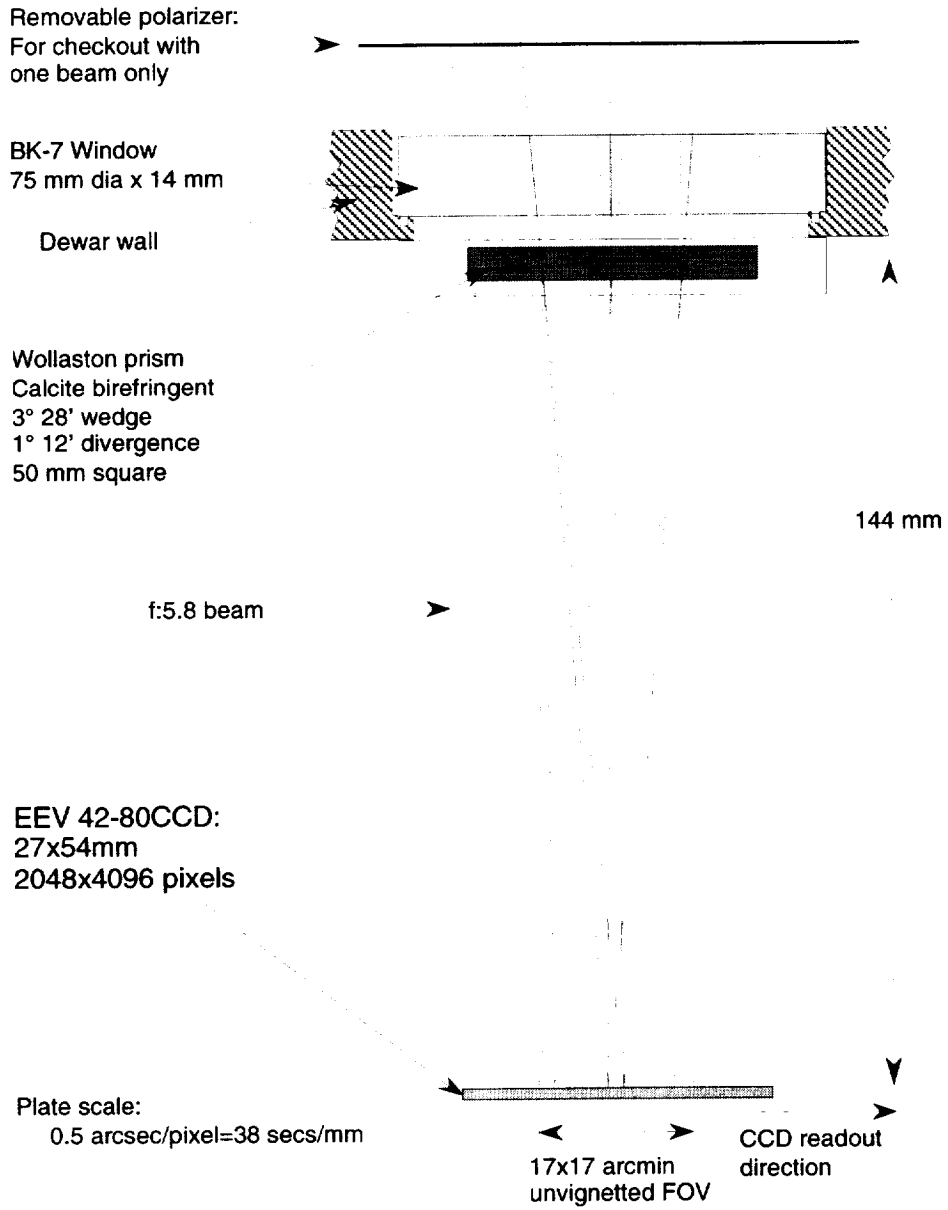
CCD readout
direction

17x17 arcmin
unvignetted FOV

*Figure 1. Testbed beam splitter. A Wollaston prism is used to generate two identical beams from each star to demonstrate the CCD photometric performance. Each double star image is separated by 228 pixels = 3.00 mm.*

100

the beam displacement. Household dust that can be seen with a hand-held magnifier has dimensions on the order of 5 by 200 μm. All dust larger than this can be easily detected and removed. Specifically, the effect of a 5- by -200 μm or 18-μm-diameter piece of dust amounts to $3 \times 10^{-7}$ of the beam. A variation in surface density of 30 particles of this size or of scratches or defects in the calcite crystal would be required to have a $10^{-5}$ change in the brightness ratio. Hence, the imperfection and cleanliness level required, although severe, is not an unreasonable requirement. Assembly of the calcite and dewar will be done on a cleanbench.

## Summary

A system end-to-end test will be performed to demonstrate the upper limit to the differential photometric precision that can be expected for a back-illuminated CCD. A Wollaston prism will be used to generate realistic stellar images for performance of the differential measurements. System parameters will be matched as closely as possible to that of the proposed Kepler Mission.

# References

Borucki, W. J.; Koch, D. G.; Dunham, E. W.; and Jenkins, J. M.: The *Kepler Mission*: A Mission to Determine the Frequency of Inner Planets Near the Habitable Zone for a Wide Range of Stars, *Planets Beyond Our Solar System and Next-Generation Space Missions, ASP Conf. Ser.*, vol. 119, 1997.

Brown, Timothy M., and Gilliland, Ronald L.: Asteroseismology, *ARAA*, vol. 32, 1994, pp. 37–82.

Dunham, E. W.; R. L. Baron; J. L. Elliot J. V.; Vallerga, J. P. Doty; and Ricker, G. R.: Publ. Astron. Soc. Pacific, vol. 97, 1985, p. 1196.

Dunham, E.W.: Optical Instrumentation for Airborne Astronomy, Airborne Astronomy Symposium on the Galactic Ecosystem, ASP Conf. Ser. M. R. Haas, J. A. Davidson, and E. F. Erickson, eds. vol. 73, 1995, pp. 517–522.

Jenkins, Jon M.; Borucki, William J.; Dunham, Edward W.; and McDonald, John S.: High-Precision Photometry with Back-Illuminated CCDs, *Planets Beyond Our Solar System and Next Generation Space Missions, ASP Conf. Ser.* vol. 119, 1997, pp. 227–228.

Kasting, J.F.; Whitmire, D.P.; and Reynolds, R.T.: *Icarus*, vol. 101, 1993, p. 108.

Koch, D.; Borucki, W.; Cullers, K.; Dunham, E.; Webster, L.; Miers, T.; and Reitsema, H.: System Design of a Mission to Detect Earth-Sized Planets in the Inner Orbits of Solar-Like Stars, *JGR-Planets*, vol. 101, 1996, p. 9297.

Leach, Robert: CCD Controller Requirements for Ground-Based Optical Astronomy, *Solid-State Sensor and CCD Cameras*, SPIE, vol. 2654, 1996, pp. 218–225.

Nikzad, S.; Hoenk, M.E.; Grunthaner, P. J.; Terhune, R. W.; Grunthaner, F. J.; Winzenread, R.; Fattahi, M.; and Tseng, H-F: SPIE, vol. 2198, 1994, p. 907.

Robinson, L. B.; Wei, M.Z.; Borucki, W. J.; Dunham, E. W.; Ford, C. H.; and Granados, A. F.: Publ. Astron. Soc. Pacific, vol. 107, 1995, pp. 1094–1098.

Stone, R.: The Crossley Reflector: A Centennial Review, *Sky & Tel*, 1979, pp. 307–311 and 396–400.

# REPORT DOCUMENTATION PAGE

| 1. AGENCY USE ONLY *(Leave blank)* | 2. REPORT DATE<br>February 2001 | 3. REPORT TYPE AND DATES COVERED<br>Conference Publication |
|---|---|---|

**4. TITLE AND SUBTITLE**

Third Workshop on Photometry

**6. AUTHOR(S)**

Edited by William J. Borucki and Lawrence E. Lasher

**5. FUNDING NUMBERS**

624-06-09

**7. PERFORMING ORGANIZATION NAME(S) AND ADDRESS(ES)**

Ames Research Center
Moffett Field, CA 94035-1000

**8. PERFORMING ORGANIZATION REPORT NUMBER**

A-00V0026

**9. SPONSORING/MONITORING AGENCY NAME(S) AND ADDRESS(ES)**

National Aeronautics and Space Administration
Washington, DC 20546-0001

**10. SPONSORING/MONITORING AGENCY REPORT NUMBER**

NASA/TM–2001-209614

**11. SUPPLEMENTARY NOTES**

Proceedings of a Workshop held at the SETI Institute in Palo Alto, California.
Point of Contact: William J. Borucki, Ames Research Center, MS 245-3, Moffett Field, CA 94035-1000
(650) 604-6492

**12a. DISTRIBUTION/AVAILABILITY STATEMENT**

Unclassified — Unlimited
Subject Category 8, 9      Distribution: Standard
Availability: NASA CASI (301) 621-0390

**12b. DISTRIBUTION CODE**

**13. ABSTRACT *(Maximum 200 words)***

The Third Workshop on Photometry was held at the SETI Institute in Palo Alto, California on September 24 and 25, 1998. The workshop emphasizes equipment and software capable of routinely obtaining high precision when monitoring thousands of stars. The papers by Dunham, Borucki, Brown, Everett et al., and Henry discuss the instrumentation and software currently in use. Tests to identify the causes of photometric errors are described by Deeg and Doyle, Howell and Everett, Koch et al., Lockwood, and Mena-Werth.

**14. SUBJECT TERMS**

Photometry, Charged coupled device (CCD), Vulcan

**15. NUMBER OF PAGES**
112

**16. PRICE CODE**
A06

| 17. SECURITY CLASSIFICATION OF REPORT | 18. SECURITY CLASSIFICATION OF THIS PAGE | 19. SECURITY CLASSIFICATION OF ABSTRACT | 20. LIMITATION OF ABSTRACT |
|---|---|---|---|
| Unclassified | Unclassified | | |